Winter 12-15-2017

Reconstruction Algorithms for Novel Joint Imaging Techniques in PET

Homayoon Ranjbar
Washington University in St. Louis

Recommended Citation

Ranjbar, Homayoon, "Reconstruction Algorithms for Novel Joint Imaging Techniques in PET" (2017). *McKelvey School of Engineering Theses & Dissertations*. 292.
https://openscholarship.wustl.edu/eng_etds/292

Washington University in St. Louis

School of Engineering and Applied Science

Electrical and Systems Engineering Department

Dissertation Examination Committee:
Joseph A. O'Sullivan, Chair
Mark A. Anastasio
Ulugbek Kamilov
Richard Laforest
Yuan-Chuan Tai

Reconstruction Algorithms for Novel Joint Imaging Techniques in PET

by

Homayoon Ranjbar

A dissertation presented to
The Graduate School
of Washington University in
partial fulfillment of the
requirements for the degree
of Doctor of Philosophy

Contents

List of Tables

List of Figures

Acknowledgments

I would like to extend my sincerest gratitude to Professor Yuan-Chuan Tai in Mallinckrodt Institute of Radiology at Washington University School of Medicine. Dr. Tai supported my work in every possible way during my PhD years. He's been a great adivsor, a supportive and patient mentor, and a vigilant guidance in my graduate studies.

As a student from the Electrical and Systems Engineering Department, my main advisor was Professor Joseph A. O'Sullivan. Dr. O'Sullivan has always been generous to me with his insighful discussions regarding the theoretical aspect of my work. He has literally been my professor and I learned a great deal of my Emission Tomogrpahy and Statistical Inference mathematical knowledge from him and his lectures.

I owe a great deal of the experiences that I gained during my program, to Mr. Jie Wen, Dr. Aswin J. Mathews, and Dr. Ke Li. Jie was the main designer and assembler of the Beta-Gamma Imager and helped me to understand the system and how to work with it. Aswin has been a patient and supportive mentor during the first 2 years of my time in Tai Lab. He helped me to gain computer progamming and technical writing skills. Ke helped me with GPU programming and has engaged in many productive discussions that benefitted my work.

A major portion of this research was supported by the Office of Science (BER), U.S. Department of Energy (DE-SC0005157). I would like to thank Washington University cyclotron facility and Dr. Dong Zhou for provision of ^{18}F and ^{11}C. Some of the computations were

performed using the facilities of the Washington University Center for High Performance Computing (CHPC), which were partially provided through National Institute of Health (grant NCRR 1S10RR022984-01A1), and I appreciate very helpful advices from Malcolm Tobias regarding the CHPC.

At last my special thanks go to the many graduate students and distinguished faculty members within my department who have reviewed this thesis and/or helped support the related research: Dr. Qiang Wang, Dr. Sergey Komarov, Dr. Jianyong Jiang, Mr. Dimitre Tomov, and Mr. Beichuan Qi.

Homayoon Ranjbar

Washington University in Saint Louis
December 2017

Dedicated to my lovely wife Mahsa, and to my beloved parents.

ABSTRACT OF THE DISSERTATION

Reconstruction Algorithms for Novel Joint Imaging Techniques in PET

by

Homayoon Ranjbar

Doctor of Philosophy in Engineering

Washington University in St. Louis, December 2017

Research Advisors: Joseph A. O'Sullivan and Yuan-Chuan Tai

Positron emission tomography (PET) is an important functional in vivo imaging modality with many clinical applications. Its enormously wide range of applications has made both research and industry combine it with other imaging modalities such as X-ray computed tomography (CT) or magnetic resonance imaging (MRI). The general purpose of this work is to study two cases in PET where the goal is to perform image reconstruction jointly on two data types.

The first case is the Beta-Gamma image reconstruction. Positron emitting isotopes, such as ^{11}C, ^{13}N, and ^{18}F, can be used to label molecules, and tracers, such as $^{11}CO_2$, are delivered to plants to study their biological processes, particularly metabolism and photosynthesis, which may contribute to the development of plants that have higher yield of crops and biomass. Measurements and resulting images from PET scanners are not quantitative in young plant structures or in plant leaves due to low positron annihilation in thin objects. To address this problem we have designed, assembled, modeled, and tested a nuclear imaging system (Simultaneous Beta-Gamma Imager). The imager can simultaneously detect positrons (β^+)

and coincidence-gamma rays (γ). The imaging system employs two planar detectors; one is a regular gamma detector which has a LYSO crystal array, and the other is a phoswich detector which has an additional BC-404 plastic scintillator for beta detection. A forward model for positrons is proposed along with a joint image reconstruction formulation to utilize the beta and coincidence-gamma measurements for estimating radioactivity distribution in plant leaves. The joint reconstruction algorithm first reconstructs the beta and gamma images independently to estimate the thickness component of the beta forward model, and then jointly estimates the radioactivity distribution in the object. We have validated the physics model and the reconstruction framework through a phantom imaging study and imaging a tomato leaf that has absorbed $^{11}CO_2$. The results demonstrate that the simultaneously acquired beta and coincidence-gamma data, combined with our proposed joint reconstruction algorithm, improved the quantitative accuracy of estimating radioactivity distribution in thin objects such as leaves. We used the Structural Similarity (SSIM) index for comparing the leaf images from the Simultaneous Beta-Gamma Imager with the ground truth image. The jointly reconstructed images yield SSIM indices of 0.69 and 0.63, whereas the separately reconstructed beta alone and gamma alone images had indices of 0.33 and 0.52, respectively.

The second case is the virtual-pinhole PET technology, which has shown that higher resolution and contrast recovery can be gained by adding a high resolution PET insert with smaller crystals to a conventional PET scanner. Such enhancements are obtained when the insert is placed in proximity of the region of interest (ROI) and in coincidence with the conventional PET scanner. Intuitively, the insert may be positioned within the scanner's axial field-of-view (FOV) and radially closer to the ROI than the scanner's ring. One of the complicating factors of this design is the insert's blocking the scanner's lines-of-response (LORs). Such data may be compensated through attenuation and scatter correction in image reconstruction. However, a potential solution is to place the insert outside of the scanner's axial FOV and to move the body to be in proximity of the insert. We call this imaging strategy the *surveillance* mode. As the main focus of this work, we have developed an image reconstruction framework for the surveillance mode imaging. The preliminary results show improvement in spatial resolution and contrast recovery. Any improvement in contrast recovery should result in enhancement in tumor detectability, which will be of high clinical significance.

Chapter 1

Background

1.1 Positrons

Proton-rich isotopes such as ^{18}F and ^{11}C decay via positron emission, in which a proton in the nucleus decays to a neutron, a positron, and a neutrino.

$$^{18}_{9}F \rightarrow^{18}_{8} O + \beta^{+} + \nu_{e} \tag{1.1}$$

Equation 1.1 shows the positron-decay products of ^{18}F.

The positron (β^{+}) is the antiparticle counterpart of the electron; it has the same mass as the electron and has the same electric charge as the electron but with positive sign. The positron has some initial kinetic energy right after the nuclear decay. This kinetic energy is not a single value but has a spectrum that is referred to as the beta energy spectrum. See Figure 1.1 for the theoretical energy spectra of some of the useful positron-emitting radionuclides. For positrons with emission energy in the range of $10 - 10000$ keV, they lose their kinetic energy mainly by interacting with the atomic electrons of the surrounding medium. The distance a positron travels before coming to a full stop, is referred to as positron *range*.

When a positron collides with an electron, it will annihilate and will produce two 511-keV back-to-back gamma rays:

$$\beta^{+} + e^{-} \rightarrow \gamma + \gamma$$

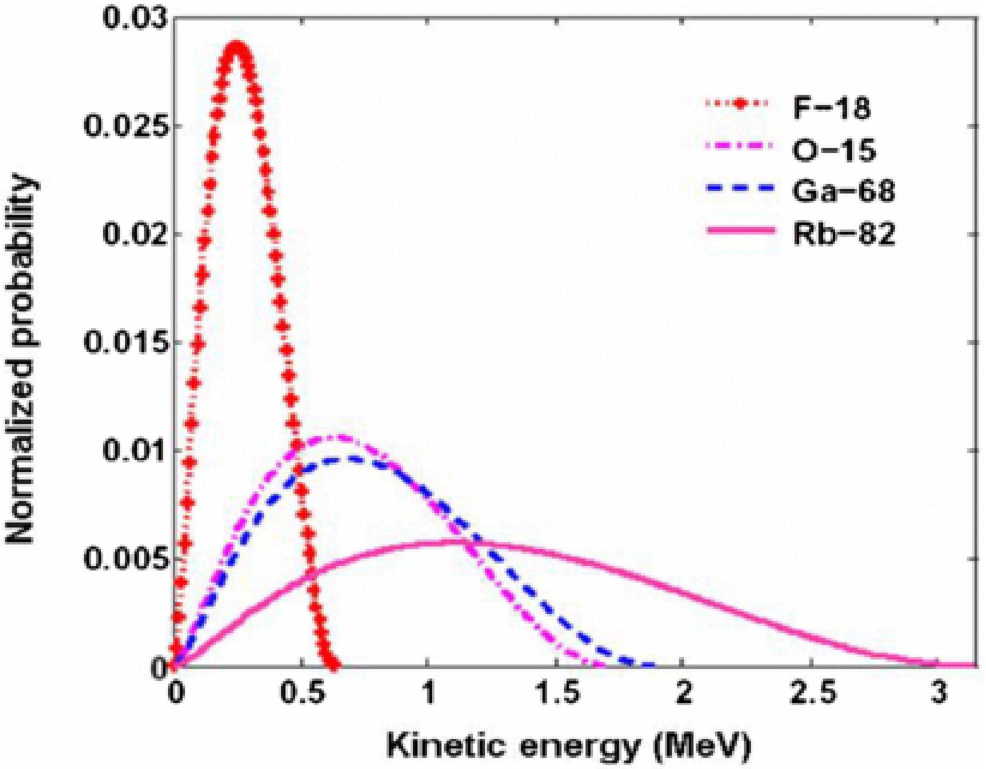

Figure 1.1. Theoretical positron emission energy spectra ([85]). Values are analytically calculated based on the method presented in [118]

If the momentum of the positron, at the time of collision, is not zero then the angle between the two gamma rays will be less than 180°. This discrepancy is referred to as annihilation *non-collinearity.* Positron range and annihilation non-collinearity cause uncertainty for localizing the origin of the radioactive decay.

1.2 Positron Emission Tomography

Positron Emission Tomography (PET) is a nuclear imaging technique. The first PET scanner was developed by a group of scientists at Washington University School of Medicine [103, 86], supposedly to improve the limitations attributed to previously existing nuclear medicine imaging techniques, such as low contrast, low resolution, and non-uniformity of the system response.

Modern PET scanners consist of multiple rings stacked in the axial direction or equivalently of sectors arranged concentrically. Each ring consists of modular detectors, and each module consists of an array of crystals, as depicted schematically in Figure 1.2.

The radiopharmaceutical used for a PET scan, is a chemical compound labeled with a positron-emitting radionuclide such as ^{18}F. The radionuclide decays and the emitted positron annihilates with an electron, which produce two back-to-back gamma rays. If both of the gamma rays hit a pair of opposing detectors of the scanner within a pre-defined time window (typically a few nano seconds) then a coincidence event is registered and recorded as one piece of measurement. After a particular period of data acquisition (e.g. 15 to 20 minutes), the measurements are sorted and fed into the image reconstruction software (computer) to create an image volume which is called a PET scan image (Figure 1.3).

Additional to its applications in a wide range of research (neuropsychiatry, cardiology, pharmacy, etc.), PET's major clinical application is in cancer diagnosis. Prior to a PET scan, a radiopharmaceutical such as fluorodeoxyglucose (^{18}F-FDG) is injected to the patient. ^{18}F-FDG is a glucose analog. Since cancerous cells have defective metabolic pathway, they consume glucose as their primary energy source, and therefore, take up more FDG than the normal cells under fasting condition. This contrast in the uptake value between the normal

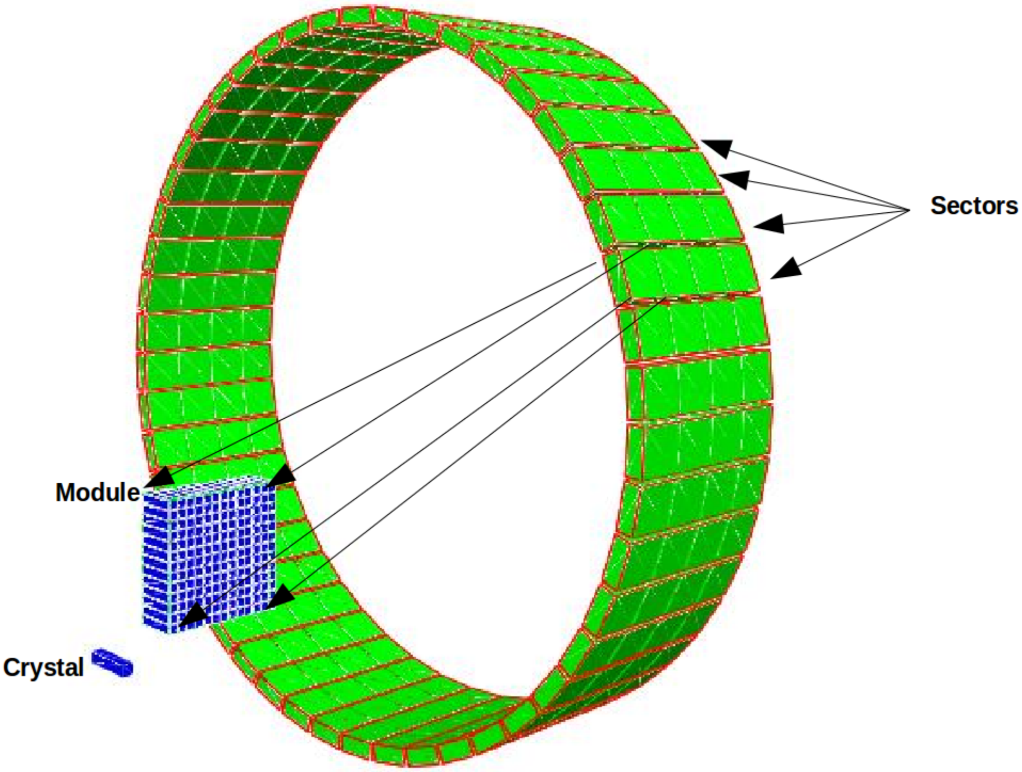

Figure 1.2. Simplified schematic of the elements of a 52-ring PET scanner geometry

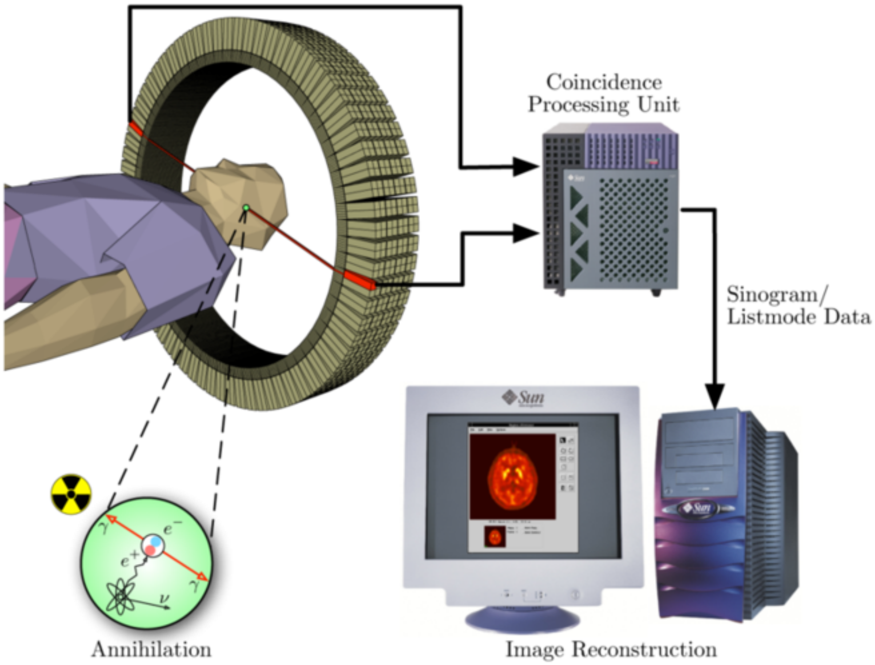

Figure 1.3. Simplified schematic of a PET scan data acquisition and image reconstruction

Table 1.1. Notations

Symbols	Denoting
I	Data space ($i \in I$)
J	Image space ($j \in J$)
$\mathbf{d}$	Data
$\mathbf{v}$	Image intensity
d_i	Data at the i-th data space unit
v_j	Image intensity at the j-th image space unit
H	System matrix

and the canerous cells, is recovered in the PET image, making it possible to detect and localize the tumors.

There is another nuclear medicine imaging modality called Single-Photon Emission Computed Tomography (SPECT) that can provide metabolic and functional information like PET. SPECT scanners are less expensive than PET scanners and require gamma emitting radioisotopes such as ^{123}I, ^{131}I, and ^{99m}Tc. However, the contrast and spatial resolution of SPECT images are inferior to those of PET images.

1.3 Image Reconstruction

1.3.1 Filtered Back-projection

In tomographic data acquisition, measurements are typically made from all angles in a 2π-radian span. A widely-used realization of such acquisition is to define the measurements in terms of line integrals that are indexed by an angle (θ) and a distance variable (s). If the object function is defined as $f(x, y)$ and the projection view is along the s-axis which is rotated θ degrees counter-clock wise with respect to the x-axis.

$$x = r\cos(\theta + \phi) = r\cos\theta\cos\phi - r\sin\theta\sin\phi = s\cos\theta - t\sin\theta$$

$$y = r\sin(\theta + \phi) = r\sin\theta\cos\phi + r\cos\theta\sin\phi = s\sin\theta + t\cos\theta$$

Where:

$$r^2 = x^2 + y^2 = s^2 + t^2$$

Equivalently:

$$(s, t) = (x \cos\theta + y \sin\theta, -x \sin\theta + y \cos\theta) \tag{1.2}$$

The projection of the 2-D function $f(x, y)$ along the projection view, i.e. s-axis, is defined by the projection function $p_\theta(s)$:

$$p_\theta(s) = \int_{-\infty}^{+\infty} \int_{-\infty}^{+\infty} f(x, y)\delta\left(s - (x \cos\theta + y \sin\theta)\right) dxdy$$

which can be written as:

$$p_\theta(s) = \int_{-\infty}^{+\infty} f\left(s \cos\theta - t \sin\theta, s \sin\theta + t \cos\theta\right) dt \tag{1.3}$$

Equation 1.3 is a very useful operator in imaging science and is called *Radon Transform.*

In order to derive the filtered back-projection equation, we need to clearly note a fundamental theorem:

Theorem 1 (Projection Slice Theorem)**.** *The 2-D Fourier transform of a 2-D function, if sampled along a projection view in frequency domain, is equal to the 1-D Fourier transform of the projection of the 2-D function along the projection view in space domain.*

Proof. Now, let us consider the 2-D Fourier transform of the 2-D fucntion $f(x, y)$:

$$F(k_x, k_y) = \int_{-\infty}^{+\infty} \int_{-\infty}^{+\infty} f(x, y) e^{-j2\pi(xk_x + yk_y)} dxdy$$

In order to sample the 2-D Fourier transform along the projection view in frequency domain, we have:

$$k_x = \rho \cos\theta$$

$$k_y = \rho \sin\theta$$

Thus:

$$\begin{aligned} F(\rho\cos\theta, \rho\sin\theta) &= \int_{-\infty}^{+\infty}\int_{-\infty}^{+\infty} f(x,y) e^{-j2\pi(x\rho\cos\theta + y\rho\sin\theta)} dxdy \\ &= \int_{-\infty}^{+\infty}\int_{-\infty}^{+\infty} f(x,y) e^{-j2\pi\rho(x\cos\theta + y\sin\theta)} dxdy \end{aligned}$$

By changing the coordinate system from (x, y) to (s, t), we will have:

$$F(\rho\cos\theta, \rho\sin\theta) = \int_{-\infty}^{+\infty}\int_{-\infty}^{+\infty} f\left(s\cos\theta - t\sin\theta, s\sin\theta + t\cos\theta\right) e^{-j2\pi\rho s} dsdt$$

Change the order of integrals and take out the exponential:

$$F(\rho\cos\theta, \rho\sin\theta) = \int_{-\infty}^{+\infty} e^{-j2\pi\rho s} \left(\int_{-\infty}^{+\infty} f\left(s\cos\theta - t\sin\theta, s\sin\theta + t\cos\theta\right) dt\right) ds$$

Using 1.3:

$$\begin{aligned} F(\rho\cos\theta, \rho\sin\theta) &= \int_{-\infty}^{+\infty} e^{-j2\pi\rho s} p_\theta(s) ds \\ &= \mathcal{F}_{1D}\left\{p_\theta(s)\right\} \end{aligned}$$

□

From the Fourier analysis we have: $f(x, y) = \mathcal{F}_{2D}^{-1}\{\mathcal{F}_{2D}\{f(x, y)\}\}$. Therefore we will have:

$$f(x,y) = \int_{-\infty}^{+\infty}\int_{-\infty}^{+\infty} F(k_x, k_y) e^{+j2\pi(xk_x + yk_y)}\ dk_x\ dk_y$$

Changing the integral variable from Cartesian coordinate system to polar coordinate system, i.e $(k_x, k_y) \to (\rho, \theta)$:

$$f(x,y) = \int_0^{2\pi}\int_0^{+\infty} F(\rho\cos\theta, \rho\sin\theta) e^{+j2\pi\rho(x\cos\theta + y\sin\theta)} \rho\ d\rho\ d\theta$$

Breaking down the above integral into four integrals, i.e. $\int_0^{\frac{\pi}{2}}$, $\int_{\frac{\pi}{2}}^{\pi}$, $\int_{\pi}^{\frac{3\pi}{2}}$, $\int_{\frac{3\pi}{2}}^{2\pi}$, we will then have:

$$f(x,y) = \int_0^{\pi} \int_{-\infty}^{+\infty} F(\rho\cos\theta, \rho\sin\theta) e^{+j2\pi\rho(x\cos\theta + y\sin\theta)} |\rho| \; d\rho \; d\theta$$

From Equation 1.2:

$$f(x,y) = \int_0^{\pi} \int_{-\infty}^{+\infty} F(\rho\cos\theta, \rho\sin\theta) e^{+j2\pi\rho s} |\rho| \; d\rho \; d\theta \tag{1.4}$$

Equation 1.4 is *the* filtered back-projection equation. Modern PET scanners acquire data in 3-D mode which does not have interslice septa[1]. However, instead of using any 3-D filtered backprojection image reconstruction algorithms [88, 63], PET scanner manufacturers, in order to save computation time, opt to sort the 3-D data into 2-D first by means of rebinning methods [37] and then apply the 2-D FBP image reconstruction to each slice.

1.3.2 Statistical image reconstruction

1.3.2.1 Expectation-Maximization Algorithm

Expectation maximization (EM) algorithm is an iterative method to calculate the maximum likelihood estimate of a parameter. This parameter may underline a statistical model of a random variable.

Let Y be a discrete random variable (We will consider, for the scope of this manuscript, discrete random variables only) with probability mass function $g(Y, \theta)$, θ being the underlying parameter. Realization of the latent random variable Y may be observed; however, Y is a function of a broader random variable X, namely the complete data, with distribution

---

[1] Interslice septa are PET collimators that prevent the detection of cross-plane coincidence events.

$f(X, \theta)$. The two distributions are related through:

$$g(Y, \theta) = \sum_{x \in \mathcal{X}} f(X, \theta) \qquad \{\mathcal{X} : Y = h(X)\}$$

The EM algorithm consists of two steps: Expectation (E-step) and Maximization (M-step).

- In the E-step, the conditional expectation $E\left[\log f(X, \theta) | Y, \theta^{(n)}\right]$, where $\theta^{(n)}$ is the parameter at the n-th iteration, is computed.
- In the M-step, $E\left[\log f(X, \theta) | Y, \theta^{(n)}\right]$ is maximized.

To show that the EM algorithm increases the likelihood function $\log g(Y, \theta)$ at each iteration, let us consider the function:

$$\theta \to H(\theta | \theta^{(n)}) = E\left[\log f(X, \theta) | Y, \theta^{(n)}\right] - \log g(Y, \theta)$$

$H(\theta | \theta^{(n)})$ attains its maximum at $\theta = \theta^{(n)}$, i.e. for any θ such as $\theta^{(n+1)}$:

$$H(\theta^{(n+1)} | \theta^{(n)}) \leq H(\theta^{(n)} | \theta^{(n)})$$

Which is a well-known consequence of Jensen's inequality. See Lemma 1 in [39]. Thus, we will have:

$$E\left[\log f(X, \theta^{(n+1)}) | Y, \theta^{(n)}\right] - \log g(Y, \theta^{(n+1)}) \leq E\left[\log f(X, \theta^{(n)}) | Y, \theta^{(n)}\right] - \log g(Y, \theta^{(n)})$$

$$E\left[\log f(X, \theta^{(n+1)}) | Y, \theta^{(n)}\right] - E\left[\log f(X, \theta^{(n)}) | Y, \theta^{(n)}\right] \leq \log g(Y, \theta^{(n+1)}) - \log g(Y, \theta^{(n)})$$

The EM algorithm maximizes the conditional expectation $E\left[\log f(X, \theta) | Y, \theta^{(n)}\right]$, at each iteration in the M-step :

$$E\left[\log f(X, \theta^{(n+1)}) | Y, \theta^{(n)}\right] \geq E\left[\log f(X, \theta^{(n)}) | Y, \theta^{(n)}\right]$$

$$E\left[\log f(X, \theta^{(n+1)}) | Y, \theta^{(n)}\right] - E\left[\log f(X, \theta^{(n)}) | Y, \theta^{(n)}\right] \geq 0$$

Therefore:

$$\log g(Y, \theta^{(n+1)}) - \log g(Y, \theta^{(n)}) \geq 0$$

$$\log g(Y, \theta^{(n+1)}) \geq \log g(Y, \theta^{(n)}) \tag{1.5}$$

Equation 1.5 concludes that the EM algorithm monotonically increases the likelihood function of the random variable whose underlying parameter is to be estimated.

1.3.2.2 EM in Emission Computed Tomography

Let X_{ij} (complete data) be the number of emissions originating from the j-th image space unit and being detected by the detector pair corresponding to the i-th data space unit. X_{ij} is a Poisson random variable with mean $h_{ij}v_j$, i.e. $X_{ij} \sim \text{Poiss}(h_{ij}v_j)$. v_j is the number of emissions originating from the j-th image space unit and h_{ij} is the probability that an emission from the j-th image space unit, will be detected by the detector pair corresponding to the i-th data space unit. The detected number of photons d_i (incomplete data) at the i-th data space unit is a function of the complete data:

$$d_i = \sum_{j \in J_i} X_{ij}$$

Since d_i is the sum of independent Poisson random variables (X_{ij}), then d_i itself is a Poisson random variable ($d_i \sim \text{Poiss}(\bar{d}_i)$) with mean equal to the sum of the individual means:

$$\bar{d}_i = \sum_{j \in J_i} h_{ij} v_j \tag{1.6}$$

The EM algorithm computes the conditional expectation of the likelihood of the complete data:

$$\begin{align} E\left[\log f(X, \mathbf{v}) | \mathbf{d}, \mathbf{v}^{(n)}\right] &= E\left[\sum_i \sum_{j \in J_i} X_{ij} \log\left(h_{ij} v_j\right) - h_{ij} v_j | \mathbf{d}, \mathbf{v}^{(n)}\right] \tag{1.7} \\ &= \sum_i \sum_{j \in J_i} E\left[X_{ij} | d_i, \mathbf{v}^{(n)}\right] \log\left(h_{ij} v_j\right) - h_{ij} v_j \tag{1.8} \end{align}$$

In the above equations, we ignored the term $X_{ij}!$ becuase it is independent of $\mathbf{v}$.

The conditional distribution of X_{ij} given $\left(d_i, \mathbf{v}^{(n)}\right)$ is multinomial with cell probability $p_i = \frac{h_{ij}v_j^{(n)}}{\sum_{j'\in J_i} h_{ij'}v_{j'}^{(n)}}$, therefore, its mean, namely N_{ij}, is equal to $p_i d_i$.

$$E\left[\log f(X,\mathbf{v})|\mathbf{d},\mathbf{v}^{(n)}\right] = \sum_i \sum_{j\in J_i} \frac{h_{ij}v_j^{(n)}d_i}{\sum_{j'\in J_i} h_{ij'}v_{j'}^{(n)}} \log\left(h_{ij}v_j\right) - h_{ij}v_j \tag{1.9}$$

Now the M-step maximizes $E\left[\log f(X,\mathbf{v})|\mathbf{d},\mathbf{v}^{(n)}\right]$. Take the the second partial derivatives:

$$\frac{\partial^2 E}{\partial v_p \partial v_q} = \begin{cases} \sum_i \frac{h_{ip}v_p^{(n)}d_i}{\sum_{j'\in J_i} h_{ij'}v_{j'}^{(n)}} \frac{-1}{v_p^2} & p = q \\ 0 & p \neq q \end{cases}$$

The second partial derivative is strictly negative given $v_j^{(n)}$ is positive for all $j \in J$, therefore, $E\left[\log f(X,\mathbf{v})|\mathbf{d},\mathbf{v}^{(n)}\right]$ is concave and maximizing it, is trivial. Simply take the first partial derivative:

$$\frac{\partial E}{\partial v_j} = \sum_{i\in I_j} \frac{h_{ij}v_j^{(n)}d_i}{\sum_{j'\in J_i} h_{ij'}v_{j'}^{(n)}} \frac{1}{v_j} - h_{ij} \tag{1.10}$$

And set it equal to zero and solve. The result will be as follows:

$$v_j^{(n+1)} = \frac{v_j^{(n)}}{\sum_{i\in I_j} h_{ij}} \sum_{i\in I_j} h_{ij} \frac{d_i}{\sum_{j'\in J_i} h_{ij'}v_{j'}^{(n)}} \tag{1.11}$$

1.3.2.3 Notes

Equation 1.11 is *the* Maximum Likelihood Expectation Maximization (ML-EM) algorithm in PET and there are several interpretations to it. We will discuss two of them here.

By rewriting Equation 1.11 as

$$\sum_{i \in I_j} h_{ij} v_j^{(n+1)} = \sum_{i \in I_j} \frac{h_{ij} v_j^{(n)} d_i}{\sum_{k \in J_i} h_{ik} v_k^{(n)}}$$

one can easily see

$$\sum_{i \in I_j} h_{ij} v_j^{(n+1)} = \sum_{i \in I_j} N_{ij}$$

The sum of N_{ij} over all projections associated with the j-th image space unit ($i \in I_j$) is the best current estimate of the number of photons that originated from the j-th image space unit. The ML-EM algorithm tends to equate the expected number of photons, orginating from the j-th image space unit ($\sum_{i \in I_j} h_{ij} v_j^{(n+1)}$), to this best current estimate.

Another interpretation can be made by considering Equation 1.11 as an iterative multiplicative process, in which at every iteration, v_j is calculated by multiplying the previous value of v_j by a scaling factor, which is:

$$\frac{\sum_{i \in I_j} h_{ij} \frac{d_i}{\sum_{k \in J_i} h_{ik} v_k^{(n)}}}{\sum_{i \in I_j} h_{ij}} \tag{1.12}$$

The scaling factor consists of two operators, forward projection operator ($\sum_{j \in J_i} h_{ij}$) and backprojection operator ($\sum_{i \in I_j} h_{ij}$). Each iteration of the ML-EM algorithm consists of one forward projection of all the image voxels and one backprojection of all the LORs. Please note that the backprojection of ones (called the sensitivity image) is calculated once and prior to the EM iterations. Convergence is reached when this scaling factor asymptotically approaches one. This means that, at each iteration, $\mathbf{v}$ is calculated such that the ratio $\frac{d_i}{\sum_{j \in J_i} h_{ij} v_j}$ approaches unity. This is consistent with the first interpretation.

1.3.3 Maximum a posteriori algorithm

The PET data inherently have limited counts, which is due to the low radio-tracer dosage and short acquisition time in PET. In statistical image reconstruction, the underlying assumption is that the measurements have Poisson distribution. In Poisson noise model, lower count equals lower signal-to-noise ratio (SNR). Moreover, the variance of the reconstructed images using ML-EM algorithm (Equation 1.11) increases rapidly with iteration number at first, and then will plateau out when reaching convergence [16].

A convex-optimization-friendly interpretation is that using Equation 1.11, to maximize the term in Equation 1.9 by no means of any regularizer, will result in over-fitting because the data are noisy.

In order to solve the above-mentioned problem, one can add smoothing steps [94], sieves [96], stopping rules [111], and separable priors [66, 70], or can use penalized least sqaures [47].

Maximum a posteriori (MAP) or equivalently penalized ML-EM based methods are more popular because of their flexibility in terms of implementation such as parallel implementation [22]. The MAP method introduces a penalty term to the maximization of the likelihood function:

$$\begin{aligned}\hat{\mathbf{v}} &= \arg\ \max_{\mathbf{v}}\ L(\mathbf{d}|\mathbf{v}) - \beta\Phi(\mathbf{v}) && (1.13)\\ &= \arg\ \max_{\mathbf{v}}\ \sum_i \left(d_i \log\big(\sum_{j\in J_i} h_{ij}v_j\big) - h_{ij}v_j \right) - \beta \sum_j \sum_{\substack{k\in\mathcal{N}_j\\ k\neq j}} \eta_{jk}\phi\left(\frac{v_j - v_k}{\delta}\right) && (1.14)\end{aligned}$$

$\Phi(\mathbf{v})$ is the prior on the image being reconstructed iteratively and $\beta, \eta_{jk}, \delta > 0$

- β controls the relative weight of the penalty term with respect to the likelihood function (data-fitting term).
- η_{jk} defines how adjacent voxels in the image are related.
- $\phi(v_j)$ is an even function called the potential function and $\phi(v_j) \geq 0$.
- δ controls the variance imposed on the reconstructed image $\hat{\mathbf{v}}$.

One class of priors popular in emission tomography image reconstruction is the function $f(x) = \log(\cosh(x))$, i.e. $\phi(v_j) = \log(\cosh(v_j))$, $\forall j \in J$. We will explain two ways of implementing the penalized ML-EM algorithm.

1.3.3.1 One Step Late

This method doesn't have a convergence proof, however, it has been shown by empirical evidence [51], that by proper choice of $\Phi(\mathbf{v})$ and the value of its parameters, and that if β is not too large, the algorithm will converge. In this case the ML-EM update equation will be:

$$v_j^{(n+1)} = \frac{v_j^{(n)}}{\sum_{i \in I_j} h_{ij} + \beta \frac{\partial}{\partial v_j} \Phi(\mathbf{v})|_{v_j^{(n)}}} \sum_{i \in I_j} h_{ij} \frac{d_i}{\sum_{k \in J_i} h_{ik} v_k^{(n)}} \tag{1.15}$$

Equation 1.15 is derived following the same steps as to drive Equation 1.11. It's called one step late because in Equation 1.15, the penalty is applied (see the second term in the denominator) to the image of the previous iteration (n) as opposed to the current iteration $(n + 1)$.

1.3.3.2 De-coupling the potential function

This method takes advantage of the convexity of the potential function $\phi(v_j)$:

$$\phi(\alpha v_j + (1 - \alpha) v_k) \leq \alpha \phi(v_j) + (1 - \alpha) \phi(v_k) \tag{1.16}$$

$$0 \leq \alpha \leq 1$$

Using Equation 1.16:

$$
\begin{aligned}
\phi(v_j - v_k) &= \phi\left(\alpha\left[\frac{1}{\alpha}(v_j - \hat{v}_j) + (\hat{v}_j - \hat{v}_k)\right] + (1-\alpha)\left[\frac{-1}{1-\alpha}(v_k - \hat{v}_k) + (\hat{v}_j - \hat{v}_k)\right]\right) \\
&\leq \alpha\phi\left(\frac{1}{\alpha}(v_j - \hat{v}_j) + (\hat{v}_j - \hat{v}_k)\right) + (1-\alpha)\phi\left(\frac{-1}{1-\alpha}(v_k - \hat{v}_k) + (\hat{v}_j - \hat{v}_k)\right)
\end{aligned}
$$

Setting $\alpha = \frac{1}{2}$:

$$
\begin{aligned}
\phi(v_j - v_k) &\leq \frac{1}{2}\phi\left(2(v_j - \hat{v}_j) + (\hat{v}_j - \hat{v}_k)\right) + \frac{1}{2}\phi\left(-2(v_k - \hat{v}_k) + (\hat{v}_j - \hat{v}_k)\right) && (1.17) \\
&\leq \frac{1}{2}\phi(2v_j - \hat{v}_j - \hat{v}_k) + \frac{1}{2}\phi(\hat{v}_j + \hat{v}_k - 2v_k) && (1.18)
\end{aligned}
$$

Since one is minimizing the penalty term (maximizing its negative), then they may use the surrogate in Equation 1.18 instead of $\phi(\frac{v_j - v_k}{\delta})$ in Equation 1.14. Revisiting Section 1.3.2.2, the E-step (Equation 1.9) of the EM algorithm will be modified to:

$$
\begin{aligned}
E_{\text{penalized}}\left[\log f(X, \mathbf{v}) | \mathbf{d}, \mathbf{v}^{(n)}\right] = &\sum_i \sum_{j \in J_i} \frac{h_{ij} v_j^{(n)} d_i}{\sum_{k \in J_i} h_{ik} v_k^{(n)}} \log\left(h_{ij} v_j\right) - h_{ij} v_j \\
&- \frac{\beta}{2} \sum_j \sum_{k \in \mathcal{N}_j} \eta_{jk}\left[\phi(2v_j - v_j^{(n)} - v_k^{(n)}) + \phi(v_j^{(n)} + v_k^{(n)} - 2v_k)\right]
\end{aligned}
$$

Accordingly, the M-step (Equation 1.10) will be modified to:

$$
\begin{aligned}
\frac{\partial E_p}{\partial v_j} &= \sum_{i \in I_j} \frac{h_{ij} v_j^{(n)} d_i}{\sum_{k \in J_i} h_{ik} v_k^{(n)}} \frac{1}{v_j} - h_{ij} - \beta \sum_j \sum_{k \in \mathcal{N}_j} \eta_{jk}\left[\frac{\partial}{\partial v_j}\phi(2v_j - \hat{v}_j - \hat{v}_k)\right] \\
&= 0
\end{aligned}
$$

One may use the Newton-Raphson method or other gradient ascent methods to solve for $\mathbf{v}$ [79]. In Section 3.6.1, we have used Trust Region Newton's method to solve for $\mathbf{v}$.

1.3.4 List-mode ML-EM

After the developement of ML-EM algorithm for PET image reconstruction, it did not take long to develope the list-mode image reconstruction algorithm for PET [98, 15]. The list-mode reconstruction adequately fits the nature of PET, because in PET the data are acquired sequentially. The list-mode reconstruction algorithm is similar to Equation 1.11 except that the back-projection operator in the numerator of Equation 1.11 sums over the conicidence events as opposed to summing over the LORs. The ML-EM update step for list-mode image reconstruction for PET is given by Equation 1.19.

$$v_j^{(n+1)} = \frac{v_j^{(n)}}{\sum_{i \in I_j} h_{ij}} \sum_m h_{i_m j} \frac{1}{\sum_{j' \in J_i} h_{i_m j'} v_{j'}^{(n)}} \tag{1.19}$$

i_m indexes the LOR to which the m-th coincidence event belongs.

Similar to sinogram mode ML-EM, the penalized version of the list-mode ML-EM has been proposed [23] where as in Section 1.3.3 the penalty term is added in the E-step (see Equation 3.1).

1.4 Corrections in PET

Obtaining quantitative PET images in which voxel values represent the true distribution of radioactivity in the object, requires accurate corrections of various physical processes that affect the accuracy of our model for the imaging system.

1.4.1 Normalization

Some elements in the system matrix (forward model) are neglected in the calculation of the system matrix. They eventually cause artifacts in the reconstructed image. This imperfection in the calculation stems either from the incomplete physical model, such as failing to take into account the angle at which a line-of-response (LOR) enters the surface of a crystal, or from the gradual variation in the real system, such as crystal/detector degradation and failing. By scanning an exactly known emission phantom, called normalization phantom, one may estimate the neglected elements in the system matrix by comparing the acquired data from the phantom with the data from the digital phantom[2] being forward projected using the system matrix. This process is called normalization and the neglected elements are compensated for through the multiplicative factors called the normalization factors (η_k in Equation 1.20).

The normalization procedure described here, and also which most image reconstruction implementations follow, is the model based normalization presented in [12, 74]. A successful normalization in PET has two main requirements:

- The activity distribution of the normalization source must be known: the amount of radioactivity and the map of the normalization source must be known exactly with respect to some standard precision, e.g. $\frac{\text{nCi}}{\text{cc}}$.
- The activity distribution of the normalization source must provide sufficient number of coincidence events to estimate the normalization factors: the normalization source must cover the imaging field-of-view (FOV) so that the resulting coincidence events span all of the LORs.

Typical PET scanners have detectors with identical crystals, however, if the imaging system consists of more than one type of detector, either crystals of different sizes, as in [73], or crystals of different materials, as in [84] where solid-state silicon detectors have been integrated into a conventional BGO PET detector, then there are more than one type of LORs in terms of detection efficiency.

The LORs connecting detectors of the same type, as opposed to LORs connecting detectors of different types, must be properly modeled. If such property is not modeled in the forward model, then it has to be estimated by means of normalization. For example, in the virtual-pinhole PET technology (Chapter 3), scanner-scanner LORs, scanner-insert LORs, and insert-insert LORs have different detection efficiencies because the PET insert's crystals

---

[2] Also known as the emission decay map, which is the known true 3-D radioactivity distribution of the phantom.

have different detection efficiency as opposed to the scanner's crystals. It will be elaborated in Section 3.6.2.

Normalization components, namely $n_i : \forall i \in I$, are the product of all the normalization factors associated with the i-th LOR.

$$n_i = \prod_{k \in K_i} \eta_k \tag{1.20}$$

We define K_i as the set of indices of the normalization factors associated with the i-th LOR.

To estimate the normalization factors, Poisson log-likelihood function will be maximized:

$$\begin{aligned} \hat{\eta} &= \arg\max_{\eta} L(\eta) && (1.21) \\ &= \arg\max_{\eta} \sum_i d_i \log\left(\prod_{k \in K_i} \eta_k \sum_j h_{ij} v_j\right) - \prod_{k \in K_i} \eta_k \sum_j h_{ij} v_j && (1.22) \end{aligned}$$

$$\text{Subject to} \quad -\eta_k \le 0 \qquad , \forall k \in K_i, \forall i \in I$$

$\mathbf{v}$ is the known normalization emission distribution and $\mathbf{d}$ is the normalization data. We enforce non-negativity constraints on the normalization factors that appear in 1.22.

The Newton method could be used to solve the problem in Equation 1.22 under non-negativity constraints. For instance one may use a limited memory quasi-Newton method described in [72] and use the publicly availabe L-BFGS optimization library. The L-BFGC library requires only the gradient of the log-likelihood function in Equation 1.22.

Therfore, the unconstrained objective function is:

$$L(\eta) = \sum_i d_i \log\left(\prod_{k \in K_i} \eta_k \sum_j h_{ij} v_j\right) - \prod_{k \in K_i} \eta_k \sum_j h_{ij} v_j - \sum_{k \in K_i} \mu_k \eta_k \tag{1.23}$$

Since the second derivative of Equation 1.23 is strictly negative, then in order to find the maximum it suffices to take the derivative and satisfy the complimentary slackness condition:

$$\frac{\partial L}{\partial \eta_k} = \sum_{i:k \in K_i} \frac{d_i}{\eta_k} - \prod_{\substack{k' \in K_i \\ k' \neq k}} \eta_{k'} \sum_j h_{ij} v_j - \mu_k \tag{1.24}$$

And the complimentary slackness condition for inequality constraint requires that:

$$\eta_k \left(\sum_{i:k \in K_i} \frac{d_i}{\eta_k} - \prod_{\substack{k' \in K_i \\ k' \neq k}} \eta_{k'} \sum_j h_{ij} v_j \right) = 0 \tag{1.25}$$

By pre-defining line-search parameters, maximum number of iterations and proper stopping criterion, the algorithm may converge and the normalization factors are estimated.

One the normalization factors are computed, then we use Equation 1.20 to find the normalization components. Including the normalization components in the computation of the sensitivity image (denominator in Equation 1.12), will correct for normalization and Equation 1.11 will upgrade to:

$$v_j^{(n+1)} = \frac{v_j^{(n)}}{\sum_{i \in I_j} h_{ij} n_i} \sum_{i \in I_j} h_{ij} \frac{d_i}{\sum_{j' \in J_i} h_{ij'} v_{j'}^{(n)}} \tag{1.26}$$

1.4.2 Randoms Correction

Accidental coincidences (randoms) are coincidence events that have been falsely registered by the coincidence processing unit. A random event occurs when two single events from two different annihilation events, are registered as a coincidence event, simply just because they fall in a coincidence time window.

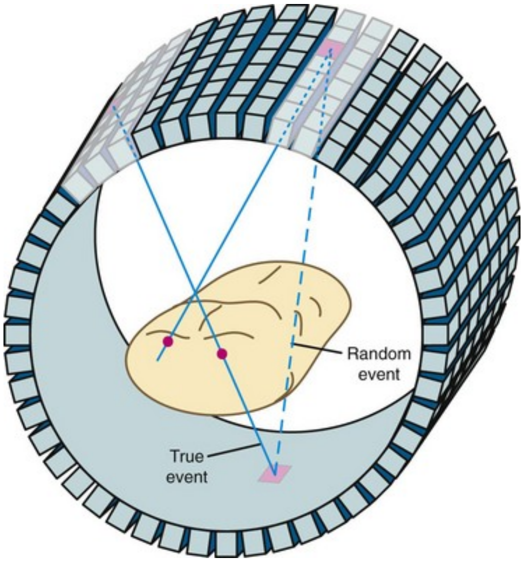

Figure 1.4. Schematic of a random event in a PET scanner [112].

If randoms are not corrected before image reconstruction, they will affect the quality of images by adding to the uncorrelated background counts in the data space. The mean of the random events can be estimated by means of particular techniques during data collection. We define such mean as $\bar{r}_i$.

1.4.2.1 Singles rate

The rate of random coincidences on a given LOR, $i \in I$, is given by Equation 1.27:

$$\bar{r}_i = 2\tau \bar{r}_{i_1} \bar{r}_{i_2} \tag{1.27}$$

where $\bar{r}_{i_1}$ and $\bar{r}_{i_2}$ are the singles rates on the two channels constituting the i-th LOR, and τ is the time coincidence window [31]. Since the count rate of singles events is generally much higer than that of the coincidence events, the above method of estimating the randoms rate, which is proportional to the product of singles rate, is statistically closer to the true mean; it is so because, in fact, the sample mean is computed as a representative of the true mean.

1.4.2.2 Delayed time window

Another method for estimating the randoms rate in PET is delayed coincidence time window. In this method, the timing signal of a particular detector is delayed by an amount significanlty greater than the system's coincidence time window. The coincidence rate of such detector, found in this mode, is an estimate of its randoms rate. This estimate can be subtracted from the prompt coincidence rate on the fly or could be stored as a separate sinogram to be used in image reconstruction as summarized in Equation 1.28. The advantage of the delayed time window method is that the dead time (explained in Section 1.4.5) properties of the delayed time window and prompt time window are identical. The disadvantage is that the estimate is statistically poor due to the relatively low count rate compared to the singles rate method. Discussing the methods to improve the statistical property of this method is beyond the scope of this chapter and interested reader may refere to [25, 11].

Therefore, a more accurate formulation for the mean of the Poisson model in PET must include the randoms:

$$d_i \sim \text{Poiss}\left(\bar{d}_i + \bar{r}_i\right) \tag{1.28}$$

d_i is the detected number of photons at the i-th data space unit (i-th LOR).

1.4.3 Attenuation Correction

The 511 keV gamma rays, generated by the annihilation process get attenuated by the anatomical structures encompassing or surrounding the decay source. It causes loss of coincidence counts detected by the system and will subsequently result in degradation of image quality. Such loss of counts can be restored and the quality of the images reconstructed from PET data, can be significantly improved if attenuation is taken into account and corrected for. An attenuation map, also known as μ-map, $\mu_j : \forall j \in J$, may be acquired by means of a X-ray CT or MRI scan prior to or at the time of the PET scan. If an X-ray CT scan is obtained, one way to estimate the μ-map is to multiply the CT image by the ratio of attenuation coefficients of water at CT and PET energies. Subsequently, the the attenuation correction factor (ACF), $\mu_i : \forall i \in I$, is calculated as:

$$\mu_i = e^{-\sum_{j \in J_i} h_{ij}\mu_j}$$

Including the ACF in the computation of the sensitivity image will correct for attenuation in PET. Thus Equation 1.26 will upgrade to:

$$v_j^{(n+1)} = \frac{v_j^{(n)}}{\sum_{i \in I_j} h_{ij} n_i \mu_i} \sum_{i \in I_j} h_{ij} \frac{d_i}{\sum_{j' \in J_i} h_{ij'} v_{j'}^{(n)}} \tag{1.29}$$

Moreover, from the attenuation map one may obtain an attenuation matrix, A, whose elements, a_{ij}, are defined as the survival probability for an annihilation at j-th image space unit being detected at i-th data space unit ([87]). Therefore, an even more precise formulation for 1.6 must include attenuation, too:

$$\bar{d}_i = \sum_j a_{ij} h_{ij} v_j \tag{1.30}$$

Pollite and Snyder derive, in [87], the EM sequence which includes randoms and attenuation correction to be:

$$v_j^{(n+1)} = \frac{v_j^{(n)}}{\sum_{i \in I} a_{ij} h_{ij}} \sum_{i \in I} a_{ij} h_{ij} \frac{d_i}{\sum_{j' \in J} a_{ij'} h_{ij'} v_{j'}^{(n)} + \bar{r}_i} \tag{1.31}$$

1.4.4 Scatter Correction

The scattering considered in PET is Compton Scattering. The phenomenon of Compton scattering in PET is very simple: the 511-keV photon is deflected by an electron and loses some of its energy which can be calculated by Equation 1.32. For example a 511-keV photon loses approximately 200 keV for a 70° deflection. This is illustrated in Figure 1.5.

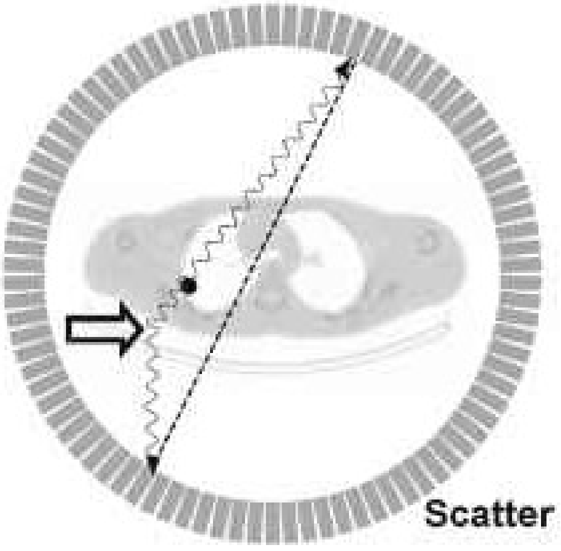

Figure 1.5. Schematic of a scattered event: The black solid circle shows the origin of annihilation, the arrow shows the point of interaction that caused the scattering, and the dashed line is the erroneously ascribed line of response.

$$E_d = \frac{511}{2 - \cos\theta} \tag{1.32}$$

E_d is the energy of the deflected photon in keV and θ is the deflection angle.

Scatter fraction (ratio of scattered events to the scattered plus unscattered events as calculated by Equation 1.33) in a PET tomograph depends on the collimator size and shape [104]. Performance characteristics of a whole-body PET scanner (Advance, General Electric Medical Systems®, Milwaukee, WI) are reported by DeGrado [38] to have, for 2-D data acquisition, a scatter fraction (SF) of 9.4% and 10.2% for direct and cross slices, respectively, and an average SF of 34% for 3-D data acquisition. As far as scattering is considered the prompt events follow a purely additive model:

$$\mathbf{d}_0 = \mathbf{d} + \mathbf{s}$$

$$\mathrm{SF} = \frac{\sum_i s_i}{\sum_{i'} d_{0i'}} \tag{1.33}$$

Where $\mathbf{d}$ is the photo-peak (unscattered) events and $\mathbf{s}$ is the scattered events. Several methods have been proposed to correct for scattering in 3D PET; Here we briefly describe them.

1.4.4.1 Convolution Subtraction

Similar to the scatter correction methods in Single-Photon Emission Computed Tomography (SPECT), [10, 49], de-convolving a scatter function with the prompt data, has been proposed for PET data as a method to correct for Compton scattering [13, 19].

In this method the underlying assumption is that there is a spatial relationship between the scattered events, $\mathbf{s}$, and the photo peak events, $\mathbf{d}$, meaning that the scattered events are the convolution of the measured events and a spatially variant and radially symmetric scatter function $\kappa(\mathbf{r}) = e^{-\alpha\mathbf{r}}$:

$$\mathbf{s} = \mathbf{d} * \kappa$$

Once the scatter function κ and the scatter fraction k have been estimated, then $\mathbf{d}$ is computed iteratively as in Equation 1.34.

$$\mathbf{d}^{(n+1)} = \mathbf{d}_0 - k\left(\mathbf{d}^{(n)} * \kappa\right) \tag{1.34}$$

n indexes the iteration.

1.4.4.2 Direct measurement

This method requires PET scanners with retractable interslice septa [28] or in other words, PET scanner capable of acquiring data both in 2-D and 3-D modes.

A short 2-D acquisition is done prior to the 3-D acquisition and the scatter distribution is esitmated by comparing the LORs common between the two datasets. The phantom used in this experiment, must have activity concentration and density varying both axially and radially.

Another similar method is to fit a Gaussian function to the scatter distribution outside of the activity-containing regions as a means of estimating the scatter distribution inside the object [99, 27].

1.4.4.3 Monte-Carlo simulation model

In this method, the reconstructed image (without scatter correction) volume is used as an input to the Monte Carlo simulation software. The intensity of each voxel in the image volume is assumed to represent the radioactivity concentration, therefore proper normalization and attenuation correction are necessary. Then the annihilation photon's interaction with the scattering medium is simulated. If both photons are detected by a pair of detector then it is saved as a coincidence event. If any of the photon has been scattered it will be saved in the scattered events sinogram, otherwise will be saved in the unscattered event sinogram. After proper scaling, the scattered events rate will be subtracted from the original data for image reconstruction. Successful results have been reported for 3-D PET brain imaging [68].

1.4.4.4 Multiple energy windows

With the improvement in BGO detectors with better energy discrimination and the advent of NaI(Tl) detectors, an energy-based scatter correction technique was proposed [90, 53].

In this method the coincidence events are grouped into two energy windows: lower energy window in which one or both photons deposit energy between 200 keV and 380 keV, and upper energy window in which both photons deposit energy between 380 keV and 850 keV. A weighted sum of the two energy windows are subtracted from the upper energy windows to compensate for scattered events. These weights are computed based on the ratio of counts of scattered events and unscattered events in the line source phantom data.

1.4.4.5 Model-based

In this method, the mean number of scattered events, $\mathbf{s}$, is estimated by means of finding the probability of a photon to undergo a single Compton scattering event. A transmission scan, an emission scan, and the scanner's forward model are used to calculate this quantity [81, 115]. Subsequently, multiple scattering will be a linear transformation of the single-scatter distribution.

In all of the above methods the goal was to estimate the mean number of scattered events. Once this value is found, then the Poisson mean in Equation 1.28 must include the mean of the scattered events $\bar{s_i}$:

$$d_i \sim \text{Poiss}\left(\bar{d_i} + \bar{r_i} + \bar{s_i}\right) \tag{1.35}$$

1.4.5 Deadtime

Deadtime can cause up to 32% resolution loss with a PET system that has 2-D data acquisition [50].

In 3-D PET, however, in order to obtain quantitative images, one has to correct for the losses associated with detector and system dead-time. The deadtime issue is due to either singles loss or coincidence loss.

- Singles loss occurs when the block detector is performing energy discrimination and does not find sufficient time to return to the quiescent state. In other words, two or more photons strike the scintillation crystal within the electronic integration time. This is also called pile-up effect. Moreover mis-positioning can occure when the incident photon in one crystal, penetrates another crystal or is scattered prior to light integration.
- Coincidence loss occurs when the coincidence processing circuitry discards the coincidence event to avoid registering *triple coincidences*.

Both of the above-mentioned losses can be properly modeled and compensated for as described in [33].

1.5 Image Quality

Image quality refers to the faithfulness with which an image represents the imaged object [29]. PET images must be accurate and this “accuracy” is interpreted as conformity both to the radioactivity uptake in the tissue and to the specific medical application or clinical utility of interest. In order to most reliably define image quality, one must take into account the purpose or the goal the medical image is intended to serve. This is referred to as the task-based assessment of image quality. Here in Section 1.5, we will introduce some of the popular figures-of-merit (FOMs) that quantify characterization of an imaging system, however, the choice of the FOM depends on the selected ensemble of patients if, for example, the taks is diagnosis or treatement planning.

1.5.1 Resolution

The spatial resolution of a PET scanner may be defined as how well the scanner can reproduce the radioactivity distribution in the object so that variations in the image are well percepted. Empirically speaking, spatial resolution of a PET scanner is the minimum distance between two points in the image that can be resolved.

Spatial resolution of a PET scanner is affected by its crystal size, positron range, annihilation non-collinearity, the reconstruction method, and localization in the detectors.

One way to quantify the spatial resolution, is to compute the full-width at half-maximum (FWHM) of the line profile of the reconstructed image of a point source. Another way is to assess the ability of the reconstructed image to resolve spherical or cylindrical sources with varying diameters and find the minimum size at which the system can resolve.

1.5.2 Contrast

The contrast of an image stems from the relative value of the regions in the image that contain tumors radioactivity distribution (signal) to the regions that contain the background radioactivity distribution (background). Contrast can be expressed as in Equation 1.36.

$$C = \frac{S - B}{B} \tag{1.36}$$

$S =$ image intensity in the lesion tissue (signal)
$B =$ image intensity in the normal tissue (background)

Therefore, a contrast of 7:1 (reads seven to one) means that the radioactivity uptake in the abnormal region is 8 times the radioactivity uptake in the surrounding background region.

1.5.3 Noise

Image noise is of random nature, and is defined as the variation in the image voxels across the image. Signal-to-noise ratio (SNR) can be improved by means of acquiring more counts, however, obtaining more counts is limited by radiation dose or acquisition time in a PET scan.

1.6 Statement of Contributions

In this work, I will study two joint reconstruction algorithms in PET: one is the joint image reconstruction of beta and coincidence-gamma data, and the other one is the joint reconstruction of scanner-scanner and scanner-insert data from two spatial positions.

1.6.1 Beta-Gamma Imager

The Beta-Gamma Imager has been designed, built, and integrated to achieve higher quantitation accuracy of radioactivity concentration uptake in thin tissues such as plant leaves. I have:

- proposed, tested, and validated the physics model for positrons' movement in media.
- introduced the joint data model and image reconstruction framework.
- developed the image reconstruction software.
- undertook validation experiments on plant leaves, and applied a proper image quality metrics to make an informed comparison between the resulted images and the ground-truth image.

All of the above are comprehensively discussed in Chapter 2.

1.6.2 Virtual pinhole PET technology

Building upon the valuable contributions of the former PhD students of our group, I have contributed to the VP-PET technology [102] by:

- developing an image reconstruction framework under the proposed imaging protocol and system geometry
- implementing the reconstruction software and applying proper normalization
- testing the image reconstruction by means of Monte-Carlo simulation
- showing the effect of scanner-insert data and the location of the insert on spatial resolution, contrast recovery, and SNR of the system

Which are extensively discussed in details in Chapter 3.

Chapter 2

The Beta-Gamma Imager

2.1 Introduction

2.1.1 Background

Now faster growing population and global climate change have made many people reconsider sustainability of their food supply. This means that the challenge of higher crop yield is more important today than it was a few decades ago. Understanding the fundamentals of plant metabolism, such as the biological mechanism by which leaves capture, convert, and store carbon is important for agricultural productivity. Plants harvest the energy of light to convert water and carbon dioxide into sugar and oxygen. This process is called photosynthesis and is carried out by the green pigments in the leaf called chlorophyll.

Carbon is abundant in the atmosphere in the form of CO_2. Increasing levels of atmospheric CO_2 [56] may improve crop productivity if carbon assimilation is increased [46, 45]. Some research groups have adopted carbon isotopes (^{11}C,^{13}C, and ^{14}C) labeling to study the metabolism of plant leaves [78, 82, 41, 42]. Moreover to carbon assimilation, other advances in plant sciences have take place to produce crops that can cope better with biotic stresses such as insects, viruses, and micro-organisms and abiotic stresses such as drought, abrupt temperature changes, and nutrient limitations. One of such advances is phenotyping. Visible light-based imaging techniques have been mostly used in phenomics, however, imaging modalities such as X-ray computed tomography (X-ray CT) and magnetic resonance imagaging (MRI) have been used to non-invasively image the inner structures of the plants and study their roots under soil [77, 20].

Researchers employed Positron Emission Tomography (PET) to provide *in vivo* and non-invasive measurements of radioactivity distribution in plants [80, 65, 58, 36, 2, 113]. Plant leaves are typically very thin (less than 0.2 mm for many species of seedlings) and thus have insufficient material for the emitted positrons to undergo an annihilation event within the tissue. Additionally, positrons have a relatively large range in the air because positron range is inversely proportional to the density of the absorber [29, p.314]. Therefore, radioactivity distribution estimation in plant leaves, using coincidence-gamma measurements, is challenging. Weisenberger has proposed a possible solution by developing a compact beta-positive, beta-minus particle imager (PhytoBeta Imager) for $^{11}CO_2$ [117]. In a feasibility study, Stolin [100] has shown that the ratio of positron detection rate to that of coincidence-gamma detection may vary from 650 to 1600. This ratio depends on many factors such as type and geometry of the detectors and thickness and geometry of the sources. However, it is generally true that beta imaging offers higher detection efficiency than PET when the emitted positrons can escape a thin object with high probability.

The use of measurements from other imaging modalities to improve the PET physics model and image reconstruction may be compared to using X-ray CT measurements to correct for attenuation in PET data [64] or to using MRI measurements for the same purpose [61]. One of the advantages of simultaneous beta-gamma imaging is to acquire more counts from the thin parts of the object. This can be useful when using short-lived isotopes such as ^{11}C [76, 18].

Tornai [108] demonstrated the initial performance of a beta imaging probe, but later modified the beta imaging intra-operative probe and created a combined γ-ray probe/$\beta^{\pm}$ imaging detector for medical purposes and compared different phoswich detector configurations [107]. A challenge in positron measurement is the non-uniformity in the thickness of leaf tissue. Alexoff [4] showed that positron escape fractions were lower in thicker leaf areas like the midrib. This causes an underestimation of radioactivity distribution from either the beta or the coincidence-gamma measurements alone. For imaging thin objects, Wu [119] has developed a detector that simultaneously measures the positrons that did not annihilate

Table 2.1. Notations

Symbols	Denoting
B	Beta data space ($i \in \mathrm{B}$)
Γ	Coincidence-gamma data space ($i \in \Gamma$)
J	Image space ($j \in J$)
w_i	i-th data space unit
s_j	j-th image space unit
u_k	k-th intermediate space unit
R_{jk}	Distance between s_j and u_k
θ_{jk}	Angle between s_j and u_k
$\mathbf{d}_\beta$	Beta data
$\mathbf{d}_\gamma$	Coincidence-gamma data
H_β	Beta system matrix
H_γ	Coincidence-gamma system matrix
(x, y, z)	Cartesian Coordinate system
$\lvert . \rvert$	Cardinality of a space
$L(\mathbf{d} \lvert \mathbf{v})$	Poisson log likelihood function
α	Joint reconstruction hyperparameter

inside the leaf (beta data) and the positrons that did annihilate inside the leaf (gamma data).

We introduce the Simultaneous Beta-Gamma Imager in Section 2.2. Therein we explain the detector design, system geometry, data acquisition, and how positron and coincidence-gamma measurements are classified. The spatial response linearity, spatial resolution, and count rate dependency of the detectors are evaluated in Section 2.2.2. The proposed model for positrons is in Section 2.3. The corresponding image reconstruction framework is described in Section 2.4, and further mathematical derivation is left for 2.4.2. In order to validate the proposed framework, we have conducted a phantom study and a plant leaf experiment; the results are presented in Sections 2.5 and 2.6. Potential improvements and investigations are discussed in Section 2.7. We make a conclusion based on the results from the imaging studies in Section 2.8.

2.1.2 Direct measurement of Positrons

As introduced in Section 1.1, while positrons travel through an attenuating medium their kinetic energy dissipates and once *thermalized* they become more likely to annihilate with an electron to produce two back-to-back 511 keV gamma rays.

If the attenuating medium was a scintillator then it would absorb the energy of the positron and would emit the absorbed energy in the form of light. Plastic scintillators are luminescent materials that can absorb the kinetic energy of positrons and emit light. Such light emission, if properly quantified, can be considered as a direct detection of positrons. This detection occurs prior to positron annihilation and is not a coincidence detection. We refer to this detection as *beta detection*.

2.1.2.1 Photomultiplier tube (PMT)

Interaction of positrons with the plastic scintillator cause scintillation which will generate electric current by means of a photo multiplier tube (PMT).

A PMT is a photoemissive device that generates electric charge by multiplying the electrons, produced by incident light, as much as 100 million times. It mainly has an evacuated glass containing a cathode, several dynodes, and an anode. Incident photons strike the cathode that will cause electrons being ejected through photoelectric effect[3]. The electrons are directed towards the electron multiplier by the focusing electrode. Then the dynodes, arranged in multiple stages, will multiply the electrons by means of secondary emission[4] process. Figure 2.1 shows a simplified schematic of a PMT.

The output of the PMT may be encoded to find the point of interaction.

---

[3] Phtotoelectric effect is the ejection of electrons when photons strike a material.

[4] Secondary emission is a phenomenon where charged particles like electrons or ions strike a material and induce the emission of a secondary electron.

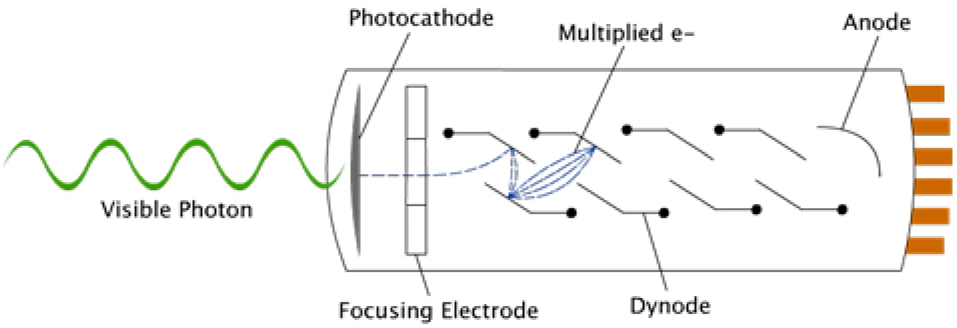

Figure 2.1. Schematic of a photomultiplier tube. Courtesy of Nathan R. Finney.

2.2 System

2.2.1 System Geometry and Detectors

The Simultaneous Beta-Gamma Imager employs two planar detectors: a phoswich detector (hybrid detector) and a gamma detector. The two detectors are positioned 9.4 cm apart facing each other vertically, as shown schematically in Figure 2.2. The three-dimensional imaging field of view (FOV) includes the 4.8 cm × 4.8 cm area in the x-y plane (detector's surface plane).

The detector set-up is secured and aligned by a custom made holder (Figure 2.3).

The phoswich detector uses a BC-404 (Saint-Gobain Crystals, Hiram, OH) plastic scintillator sheet and a lutetium-yttrium oxyorthosilicate (LYSO) crystal array [32], as presented schematically in Figure 2.4a. The phoswich detector is designed to be in direct contact with the object to be imaged. The top layer is the 4.8 cm × 4.8 cm × 0.1 cm plastic scintillator for detecting positrons. To couple the plastic scintillator to the front surface LYSO crystal array, we used room temperature vulcanization (RTV) optical glue, RTV615A (Momentive, Newark, OH) and RTV615B (GE Silicones, Huntersville, NC). The LYSO crystal array consists of 48 × 48 crystals of size 0.1 cm × 0.1 cm × 1 cm for detecting gamma rays. The light detecting unit is a Hamamatsu H8500 position sensitive photo multiplier tube (PS-PMT). The gamma detector is identical to the phoswich detector, except that it does not have the plastic scintillator (Figure 2.4b).

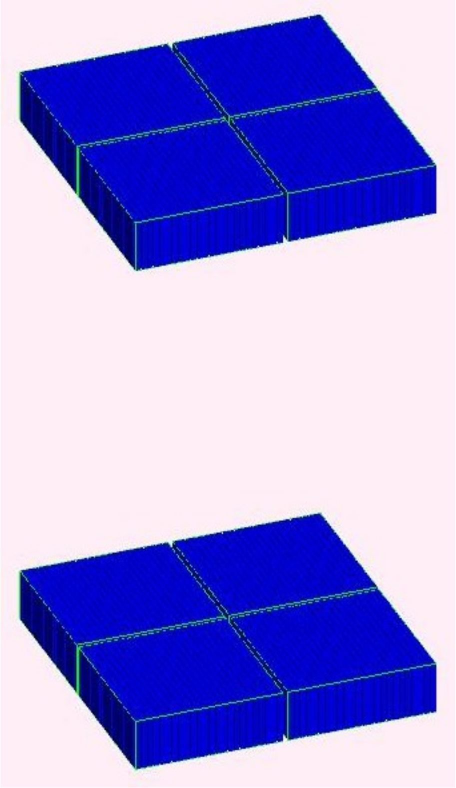

Figure 2.2. Schematic of the detector pair set-up of the Beta-Gamma Imager. The two detector heads are 9.4 cm apart in z-axis. Each head has 2 × 2 modules. Each module has 24 × 24 crystals. The crystal size is 0.1 cm × 0.1 cm × 1 cm.

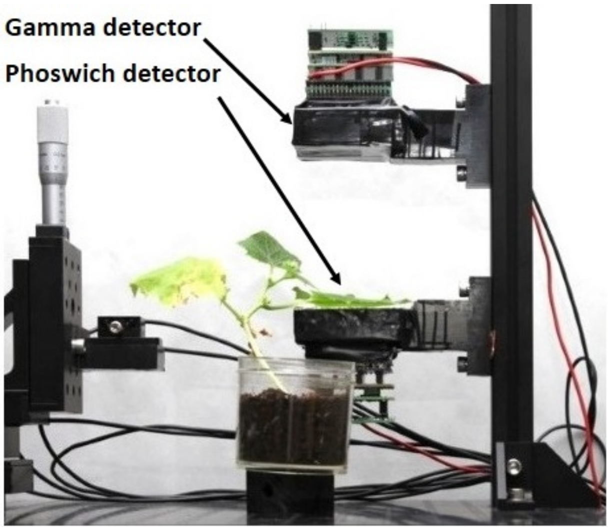

Figure 2.3. The Simultaneous Beta-Gamma Imager used for plant leaf imaging.

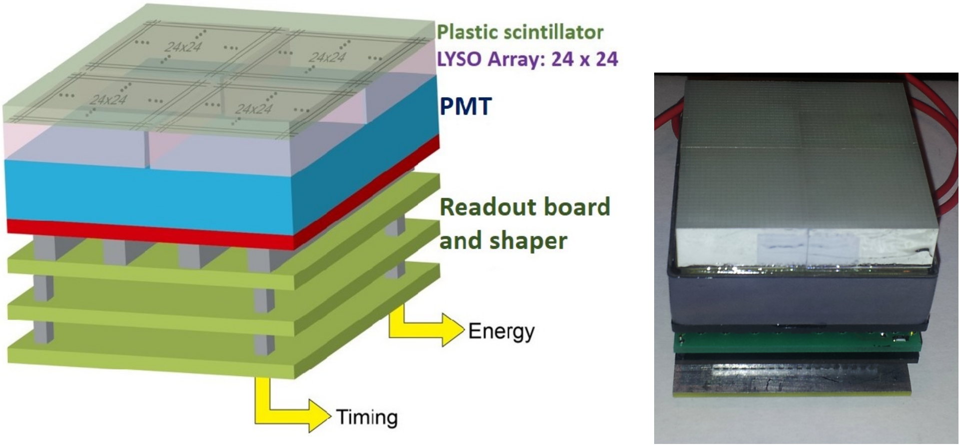

(a) A schematic of the phoswich detector

(b) A photograph of the gamma detector

Figure 2.4. The detectors developed for the beta and coincidence-gamma imaging. For the phoswich detector, the top layer is a BC-404 plastic scintillator. The gamma detector is identical to the phoswich detector but without the plastic scintillator. Each has four 24 × 24 LYSO crystal arrays arranged in a 2 × 2 grid. Crystal size is 0.1 cm × 0.1 cm × 1 cm. The scintillation light is detected by a H8500 PS-PMT. The electric signal is then conditioned by a custom designed filter circuit.

In vivo plant study typically requires bright environment, therefore the detector modules should be lightproof. Since high-energy gamma rays rarely interact with low-density materials, a 0.1 mm thick aluminum foil with black coating (Thorlabs Inc, Newton, NJ) is used to make the gamma detector lightproof.

For the phoswich detector, the light-blocking material needs to be thin because beta particles interacting with such material, before they interact with the plastic scintillator, should be minimized. Therefore, a 0.025 mm thick aluminized Mylar covers the upper surface of the plastic scintillator and side surfaces of both the plastic scintillator and the LYSO crystal array in the phoswich detector. The thin Mylar provides sufficient light blockage is not too thick to cause significant beta energy loss.

2.2.1.1 Data acquisition

The signal from the 64 anodes of the PMT is fed into a resistive multiplexer circuit which reduces the total analog outputs of the detector to 4 channels. Figure 2.5 shows the signal

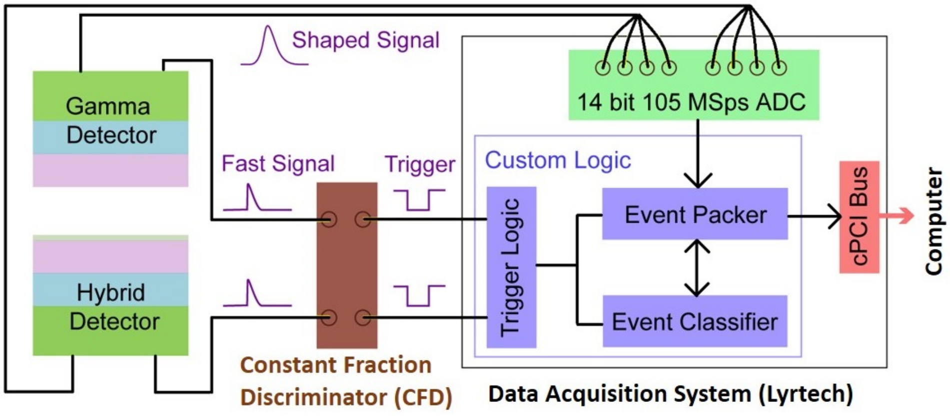

Figure 2.5. Signal flow diagram of the system. Custom designed readout circuit sends out fast signals for triggering purposes, and filters slow signals for the event classifier. The fast signals are fed into an Ortec 935 CFD module. The trigger signals are sent into the custom logic to initiate data acquisition and event classification.

flow diagram. The multiplexed signal goes into a charge-sensitive amplifier, and then into a two-stage Sallen-Key filtering circuit [89] so that the pulse signal matches the input bandwidth and sampling frequency of the analog-to-digital converter (ADC). The height of the conditioned pulse is proportional to the input charge, and the width of the pulse correlates to the width of the input signal. A timing constant of 250 ns for the filtering circuit is optimal regarding the input parameters of the ADC. The filtered pulse keeps the information of the input pulse height and the pulse shape; however, the time of interaction is lost.

In order to provide an accurate timing reference, one path of the signal is reserved to be fed into a constant fraction discriminator (CFD, ORTEC 935), which is a nuclear instrumentation module (NIM), to generate a trigger that drives the custom logic in the data acquisition (DAQ) system. Coincidence-gamma detection is also formed by applying coincidence logic between the triggering signals from both of the detectors.

The DAQ system, Lyrtech System, is a 16-channel ADC array (NUTAQ Inc. VHS-ADC) with a custom configurable field-programmable gate array (FPGA) on board. The ADC features a sample rate of 105 MHz and a resolution of 14 bits over ±1.25 V input range. The two detectors are connected to the DAQ system, and each occupies four ADC channels by their filtered outputs. The trigger signal generated by the NIM module is connected to the digital port of the DAQ system and then passed into the internal logic to initiate data

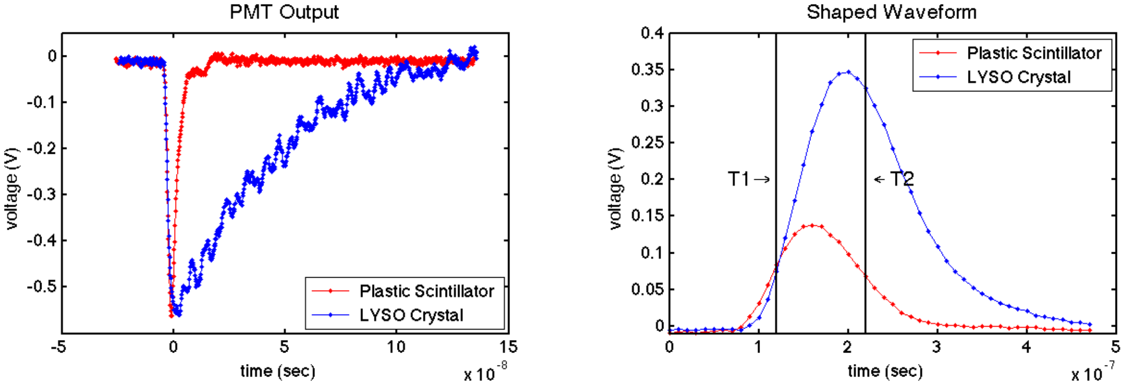

(a) Typical PMT output signals of events from plastic scintillator and LYSO crystal

(b) Typical output waveforms shaped by the filtering circuit.

Figure 2.6. Signals and waveforms from the phoswich detector. The filtering circuit conditions the signals to match the ADC sampling frequency of 105 MHz. T1 and T2 are time points used in characterizing the different time constants of pulses from plastic scintillator and LYSO crystal.

acquisition. The internal logic determines the event type by applying the event classifier, which is discussed in Section 2.2.1.2. Based on the result of the event classifier, the events are packed and streamed out to the host computer via a Compact Peripheral Component Interconnect (CompactPCI or cPCI) bus.

2.2.1.2 Event classifier

The rising edge of the light pulses both from the plastic scintillator and the LYSO crystal is 0.7 to 0.8 ns. The falling edge of a light pulse from the plastic scintillator is 2.1 ns, while it is 40 ns for the LYSO crystal. The output signals of the PMT for the two different pulses are shown in Figure 2.6a. It can be clearly seen that the rising edges of the pulses from the two types of scintillators are similar while their falling tails are significantly different.

The event classifier is implemented on custom configurable FPGA within the data acquisition system. Pulse shape discrimination is applied to the output waveforms from the phoswich detector, and the event type is determined by evaluating the timing characteristics. As shown in Figure 2.6b, events from the plastic scintillator generate a faster signal compared to the events from LYSO crystal. By selecting two appropriate time points T1 and T2 with an interval close to the rise time of LYSO crystal event, a test can be formed that involves the waveform values only at the two time points.

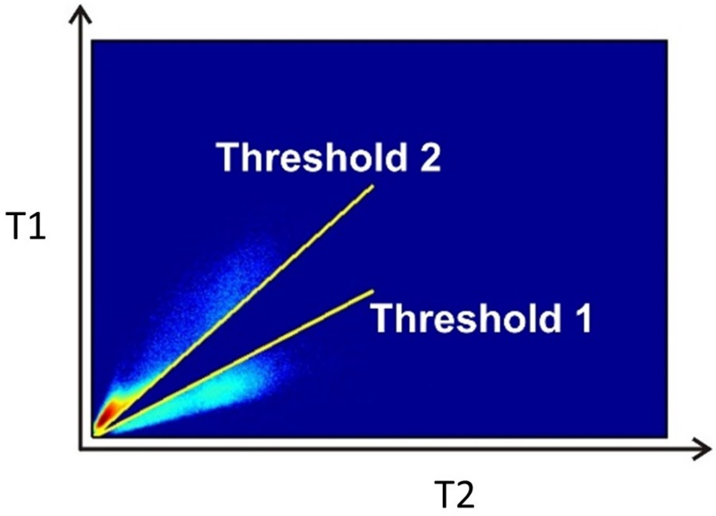

Figure 2.7. A scatter plot with the waveform values at the first time point T1 on the Y-axis and the second time point T2 on the X-axis. The two clusters are shown, and the thresholds used in the event classifier are chosen based on this scatter plot.

By generating a scatter plot with these two values, we observe a clear separation regarding the source of the events. The points fall into two groups: one corresponds to the plastic scintillator events and the other to the LYSO crystal events. The quality of the selected T1-T2 pair can be evaluated by checking the distance from the two highlighted clusters. Then, based on the scatter plot of the optimal T1-T2 pair, two threshold lines are used to define the regions in which the events, from either the plastic scintillator or the LYSO crystal, fall (see Figure 2.7). Any event with a $\frac{T1}{T2}$ ratio above Threshold 2 will be classified as a plastic scintillator event, and any event with a $\frac{T1}{T2}$ ratio below Threshold 1 will be classified as a LYSO event.

Any other event is likely to have gone through a more complicated interactions with matter and is inconclusive for this study, and thus, is discarded. We call these events *contaminated* events. An example of these events is when the light produced by the plastic scintillator is overlaid by the light produced by the scintillation crystals, because the positron detected by the plastic scintillator has annihilated with an electron and (at least one of) the gamma rays have been detected by the scintillation crystals.

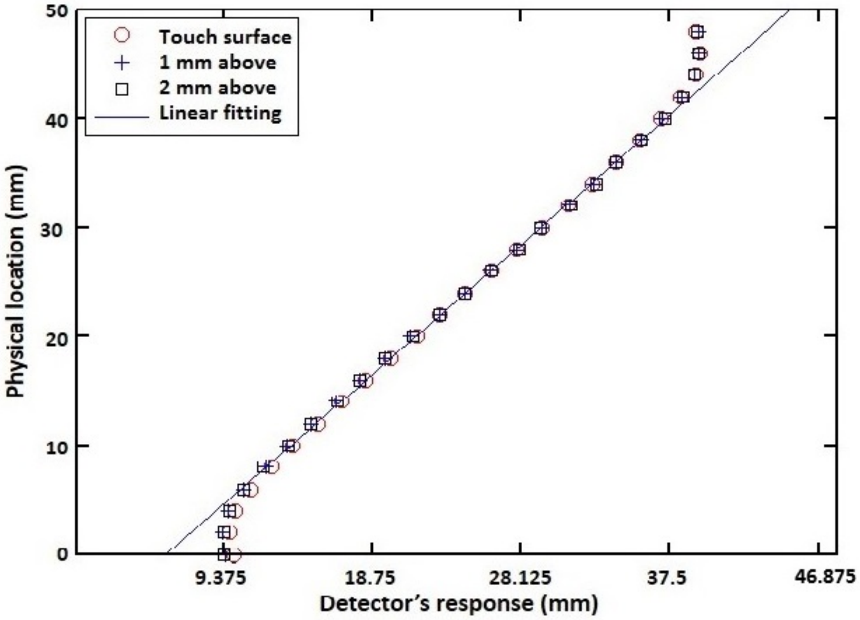

Figure 2.8. The actual physical position of the tube phantom versus the detector's measured physical position of the phantom. The solid line shows the linear fitting of the measurements.

2.2.2 System Evaluation

2.2.2.1 Beta detector spatial response linearity

A plastic tube with 0.2 mm inner diameter and 0.35 mm outer diameter was used as a line phantom. It was filled with ^{64}Cu solution[5] and moved over the detector surface by a linear translation stage in 0.2 cm long steps. The detector response to the phantom at different physical positions is evaluated using the beta data. We repeat the same measurement at different heights over the plastic scintillator surface. Figure 2.8 shows a linear relationship between the actual and the measured physical location of the phantom in the central region of the detector. Additionally, the response is almost independent of the height above the detector surface within short ranges.

However, the edge events are mixed together in the detector's response, which prevents a precise recovery of the event's actual position in the edges of the beta data. This is

---

[5] ^{64}Cu is a positron emitting isotope of Copper, its half-life is 12.7 hours and decays by 17.60% by positron emission to ^{64}Ni (see National Nuclear Data Center at www.nndc.bnl.gov).

potentially due to the complicated light path near the edge of the plastic scintillator and the light coupling with the LYSO crystals.

We measured the responses along the X-axis. Since the system is symmetric in the plastic scintillator and the electronic readout circuit, it is reasonable to assume that the response along the two axes X and Y are the same. As a result, the center 3.6 cm × 3.6 cm of the detector surface is useful for imaging purposes.

2.2.2.2 Intrinsic beta and gamma resolution

Data from a ^{18}F point source is used to characterize the system intrinsic resolution. This phantom is made by depositing ^{18}F solution onto a piece of 0.08 mm thick plastic film in a grid pattern and covered by a layer of 0.02 mm thick transparent adhesive tape (Figure 2.9a). The size of the points in the grid pattern is approximately 0.5 mm.

Points in the beta data are evaluated to obtain system intrinsic resolution for beta. Points in coincidence-gamma image (reconstructed as described in Section 2.4.1) are evaluated to obtain system intrinsic resolution for gamma.

For the beta data shown in Figure 2.9b, a line profile is drawn through the center of the two points in the first row as shown in Figure 2.9c. The resolution is calculated by measuring the full width at half maximum (FWHM) of the line profile and is found to be 2.45 mm FWHM.

For coincidence-gamma image (Figure 2.9d), a profile across the same two points is drawn and the resolution, similarly calculated, is 1.45 mm FWHM (Figure 2.9e)

2.2.2.3 System count rate dependency measurement

High beta detection efficiency combined with high event rate, may cause dead time issues in the detector. Since our goal is to develop an accurate imaging system, any count rate dependency needs to be experimentally verified.

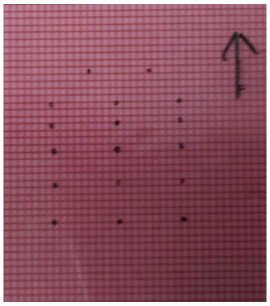

(a) Photograph of the point grid phantom used in the experiment

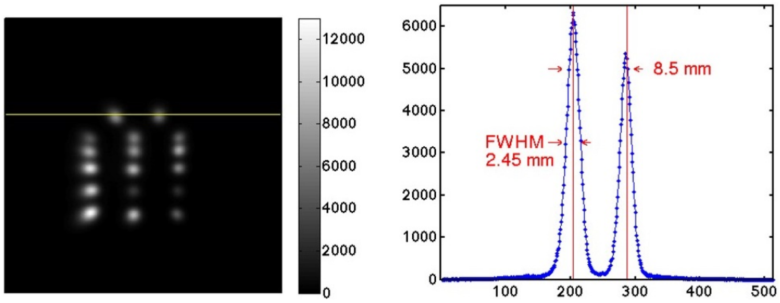

(b) Beta data

(c) Line profile and resolution calculation of the beta data

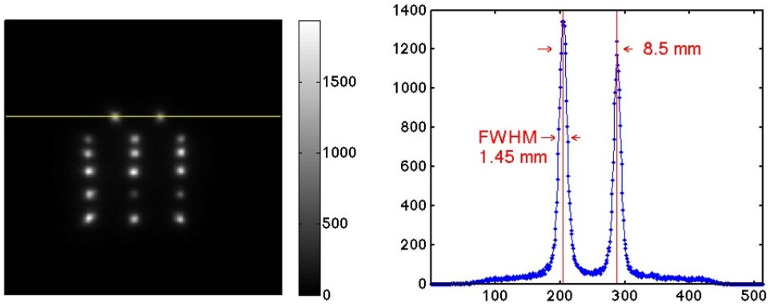

(d) Coincidence-gamma image

(e) Line profile and resolution calculation of the coincidence gamma image

Figure 2.9. System resolution measurements

A point source phantom was made with ^{18}F. The initial activity was 30.38 μCi. I acquired data for 12 hours to investigate the behavior of the detector over a relatively wide range of radioactivity levels.

Figure 2.10 shows the event count rate (measured and calculated) versus activity. Each dot represents the number of events measured over one second. The background event rate from LYSO is measured separately and is subtracted from the measured count rate. The calculated count rate is based on the final activity (0.30 μCi) measured by a dose calibrator at the end of the experiment and computing the activity for all the time points during the experiment according to the decay constant. Figure 2.10a shows the PMT trigger rate for the phoswich detector. There is a discrepancy between the measured data and the calculated activity of ^{18}F when the activity level is relatively high, i.e. above 20 μCi. However, at low activity levels the measured data and the calculated activity match. Figures 2.10b and 2.10c show the classified event trigger rate after the pulse shape discrimination is applied. A more accurate fit to the ^{18}F decay can be observed when the activity level is below 12 μCi.

In order to investigate the dependency of the classified events on the total radioactivity, I measured the percentage of each kind of event out of the event classifier as a function of activity level (Figure 2.11). The part of the curve that belongs to the higher activity levels is bent due to detector dead time issues under high count rate.

The count rate of beta events, as shown in Figure 2.10, has a smaller upper-bound threshold (12 μCi) than that of gamma events (20 μCi), because, at higher activity levels, a portion of beta events are misclassified as contaminated events and a portion of contaminated events are misclassified as gamma events. This can be better observed in Figure 2.11a where the curves for both beta and gamma events start to diverge from the black line at approximately the same activity level. Moreover, the phantom that we used, had a relatively smaller attenuation of positrons than the typical imaging objects, in order to find the worst-case count-rate-dependency threshold for beta detection.

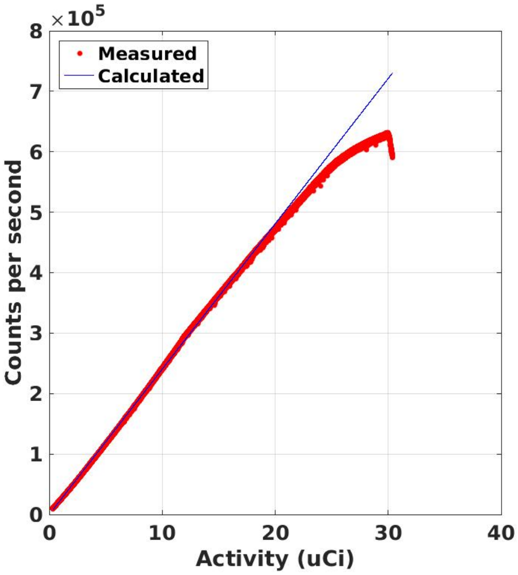

(a) Phoswich detector count rate

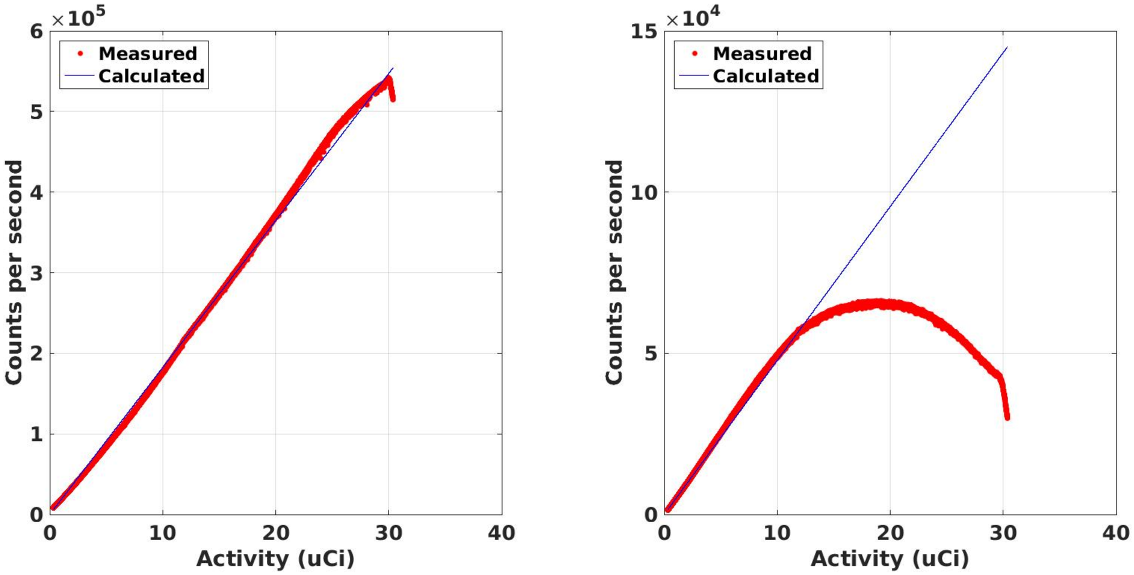

(b) Gamma detection count rate

(c) Beta detection count rate

Figure 2.10. System count rate dependency measurements

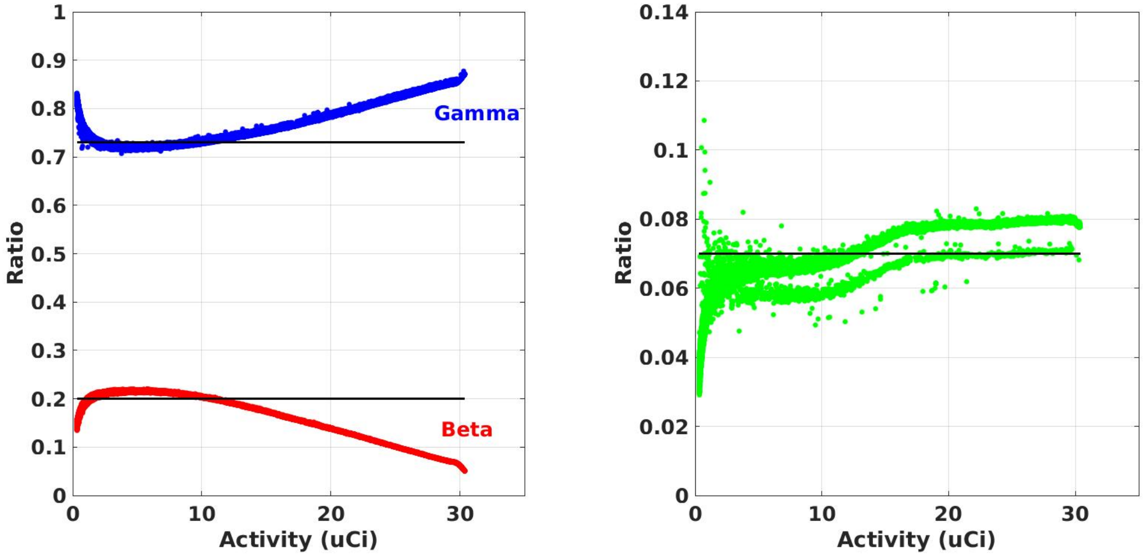

(a) Gamma and Beta events ratio

(b) Contaminated events ratio

Figure 2.11. Event statistics measurement. The ratio is the rate of each kind of events divided by the total rate of the phoswich detector. Black line is the average value from classification of signal waveforms in debugging mode: 0.73, 0.2, and 0.07 for gamma, beta, and contaminated events, respectively.

2.3 Physics model

The energy-weighted positioning technique [93] is directly used to map the point of interaction of all the events, meaning that the Anger Circuit [8] outputs of PMT are multiplexed to obtain the horizontal and vertical Cartesian location of the interaction. Beta and coincidence-gamma data are separately sorted into data arrays. We obtain the beta data ($\mathbf{d}_\beta$), from the plastic scintillator events using Anger-logic. Similarly, the coincidence-gamma data ($\mathbf{d}_\gamma$) is obtained from coincidence-gamma pair events. For gamma image reconstruction, the standard system matrix is used as described in Section 2.4.1. We propose a separate system matrix for beta, i.e., H_β. In our imaging set-up, since positrons move within two media: leaf (object) and the plastic scintillator, the beta system matrix consists of a medium-dependent component, namely, H_2 and the plastic scintillator point spread function (PSF), namely, H_1. Therefore, the overall beta system matrix is modeled using a factored matrix approach: $H_\beta = H_1 \cdot H_2$.

2.3.1 Medium-dependent Component ($\mathbf{H}_2$)

Based on the existing models on positron trajectories in water-equivalent media, Levin [69] has calculated, by means of Monte Carlo calculations, the end point distribution of positron in water for some of the most popular isotopes in PET, such as ^{18}F and ^{13}N. Furthermore, Derenzo modeled [40] the ratio of the number of positrons that survive passing through a particular distance from the origin of decay to the total number of positrons as a sum of two exponential functions of that distance. This work assumes the same model.

I assume H_2 to have a distance-dependent element and a thickness-dependent element as shown in Equation 2.1, and model the distance-dependent element by the inverse square law and obliquity. Define $[H_2]_{kj}$ as the probability of a positron from the j-th object voxel to be incident on the k-th unit, namely u_k, on the top of the plastic scintillator as an intermediate plane, namely K ($k \in K$).

$$[H_2]_{kj} \propto (h_j) \cdot \left(\frac{1}{R_{kj}^2} \cdot \cos\theta_{kj} \right) \tag{2.1}$$

where:

$$\begin{aligned} R_{kj}^2 &= (x(s_j) - x(u_k))^2 + (y(s_j) - y(u_k))^2 + (z(s_j) - z(u_k))^2 \\ \cos\theta_{kj} &= \frac{z(s_j) - z(u_k)}{R_{kj}} \\ [H_2]_{jj} &= h_j \end{aligned}$$

See Table 2.1 for the definition of the variables. Please note that $x(s_j)$ is the x coordinate of s_j, $y(s_j)$ is the y coordinate of s_j, and $z(s_j)$ is the z coordinate of s_j.

2.3.1.1 Validation

As part of our method to compute the thickness-dependent element of H_2, i.e. h_j, a ^{18}F point source was embedded between two layers of 0.05 mm thick transparent adhesive tape (as a water-equivalent medium) of equal thickness. Additional layers of tape were added in

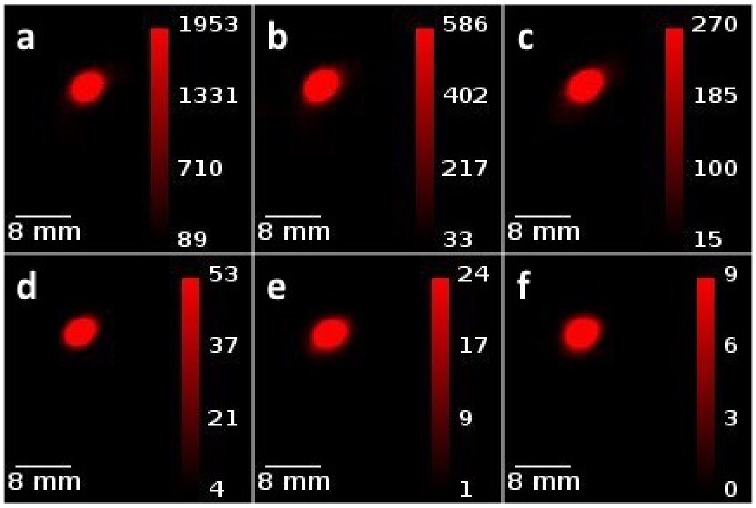

Figure 2.12. Beta image, point source of ^{18}F embedded in a water-equivalent medium for increasing variations of medium thickness: a) 0.05 mm, b) 0.15 mm, c) 0.25 mm, d) 0.45 mm, e) 0.65 mm, f) 0.85 mm. Color bars have unit of dps per image pixel.

increments of 0.05 mm to mimic medium thickness. We acquired data for each configuration of medium thickness.

Beta alone images, reconstructed using the beta data only and using the beta system matrix with $h_j = 1$, $\forall j \in J$ (as explained in Section 2.4.1), are shown in Figure 2.12 for 6 medium thickness variations. The line profile of each image was drawn and fitted to a Gaussian kernel of the form $a \cdot e^{\frac{-(x-b)^2}{2c^2}}$. a is the height of the curve's peak, b is the position of the center of the peak, and c controls the width of the "bell" [6]. The fitting parameters are listed in Table 2.2. From the value of a it can be seen that the intensity of the beta images consistently decreases as medium thickness increases. However, the value of c almost does not change for the first four configurations, and slightly changes for the last two ones (10%, and 15%). Since c is proportional to the FWHM of the Gaussian curve [7], this validates the assumption that the medium thickness mainly causes a reduction in the number of escaping positrons, and the blurring effect of medium thickness can be deconvolved by the distance-dependent element of H_2.

---

[6] The graph of a Gaussian kernel resembles a bell shaped curve

[7] $\text{FWHM} = 2c\sqrt{2\ln 2} \approx 2.3548c$

Table 2.2. Medium thickness values and fitting parameters in $y = a \cdot e^{\frac{-(x-b)^2}{2c^2}}$ for line profiles of beta images in Figure 2.12

Label	a	b	c	d	e	f
Medium Thickness (mm)	0.05	0.15	0.25	0.45	0.65	0.85
a	18148	7054	3439	504	194	63
c (mm)	0.93	0.94	0.92	0.92	1.04	1.09

2.3.1.2 Procedure

From the beta data, using only H_1, and the distance-dependent part of H_2, and ignoring the thickness-dependent part of H_2, I reconstructed the beta images. From the coincidence-gamma data, I reconstructed the gamma images (both explained in Section 2.4.1). Ideally, a known medium thickness map for all image voxels is needed in order to compute h_j. Since all of the voxels of both images have the same medium thickness (phantom design), they all have the same h_j for all image voxels. Thus, one can use the total activity ($\sum_j v_j$), instead of activity of a voxel (v_j), in order to find h_j. Define $\frac{\beta}{\beta_0}$ as the ratio of total activity of the beta image to that of the smallest medium thickness configuration, and $\frac{\beta}{\gamma}$ as the ratio of total activity of the beta image to that of the gamma image. The values of $\frac{\beta}{\beta_0}$ versus medium thickness (Figure 2.13a) can be fitted to a sum of two exponential functions similar to the results of Levin's Monte Carlo simulations for the histogram of x coordinate from positron annihilation point distribution [8] (Equation 16 in [69]). Also, I fit medium thickness versus the values of $\frac{\beta}{\gamma}$ to a sum of two exponential functions (Figure 2.13b).

h_j is a function of only medium thickness. In an imaging experiment of an object of unknown thickness distribution, one can compute h_j using the two plots in Figure 2.13. Initially, the two types of separate reconstruction tasks are executed, as they will be discussed in Section 2.4.1. Having two images (one beta $\mathbf{v}_\beta$ and one gamma $\mathbf{v}_\gamma$), for each image voxel ($j \in J$),

- first compute the thickness from ratio of beta image value to gamma image value ($\left(\frac{\mathbf{v}_\beta}{\mathbf{v}_\gamma}\right)_j$) by looking up the curve in Figure 2.13b
- Secondly, compute the normalized ratio of beta image value by looking up the fitted curve in Figure 2.13a. This ratio is the computed value for h_j.

---

[8] $P(x) = Ce^{-k_1 x} + (1-C)e^{-k_2 x} \qquad x \geq 0$

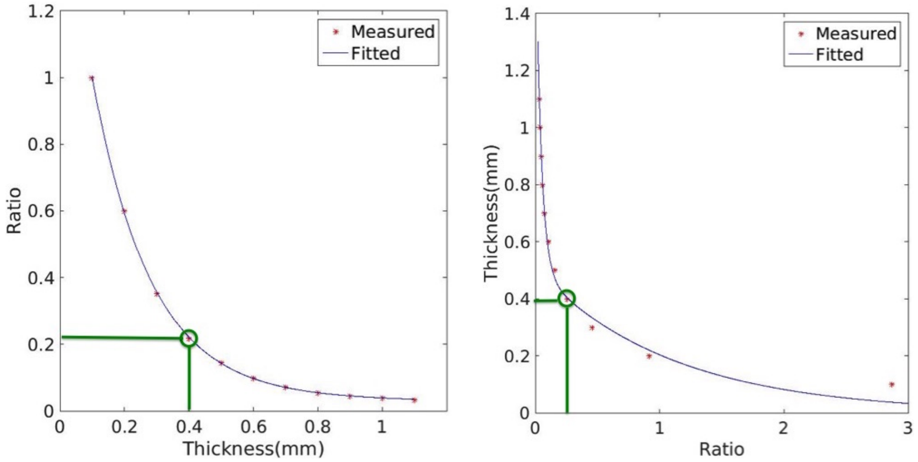

(a) The normalized ratio of beta image value versus medium thickness.

(b) The medium thickness versus the ratio of beta image value over gamma image value.

Figure 2.13. Calibration experiment. The experimental measurements are fitted to a sum of two exponential functions, i.e. $y = ae^{bx} + ce^{dx}$.

For example, if $\left(\frac{\mathbf{v}_\beta}{\mathbf{v}_\gamma}\right)_j$ is equal to 0.26 then the plot of Figure 2.13b gives a thickness of 0.4 mm, and the plot of Figure 2.13a gives $h_j = 0.22$.

2.3.2 Plastic Scintillator Component ($\mathbf{H}_1$)

We use the Point Spread Function of the plastic scintillator to compute H_1. As part of my method to find the PSF of the plastic scintillator, the beta data from a ^{18}F point source was used. The point source was less than 0.1 cm in diameter, had almost zero medium thickness, and was placed right on top of the plastic scintillator. In this set up the primary factor of blurring is the plastic scintillator's response. A weighted sum of two Gaussian kernels, defined in 2D, best fits my experimental beta data. Define:

$$\begin{aligned}[H_1]_{ik} = {} & \frac{p_3}{\sqrt{2\pi}p_1} \exp\left(-\frac{(x(u_k) - x(w_i))^2 + (y(u_k) - y(w_i))^2}{2p_1^2}\right) \\ & + \frac{1-p_3}{\sqrt{2\pi}p_2} \exp\left(-\frac{(x(u_k) - x(w_i))^2 + (y(u_k) - y(w_i))^2}{2p_2^2}\right)\end{aligned}$$

See Table 2.1 for the definition of the variables. Please note that $x(s_j)$ is the x coordinate of s_j, $y(s_j)$ is the y coordinate of s_j, and $z(s_j)$ is the z coordinate of s_j.

Then $[H_1]_{ik} \cdot \Delta x \Delta y$ is the probability of an incident positron on the plastic scintillator at the intermediate space unit u_k to be detected at data space unit w_i. Subsequently, one has to find the parameters p_1, p_2, and p_3 by data fitting and taking into account the emission map of the source.

2.4 Image Reconstruction

For all types of reconstruction, Maximum-Likelihood Expectation Maximization (ML-EM) algorithm is used for 10 iterations. Image voxel size is $0.25 \times 0.25 \times 0.1$ mm^3.

2.4.1 Separate Reconstruction

Beta alone

The beta data ($i \in \{\mathrm{B}\}$) and an incomplete beta system matrix, i.e., $H_\beta = H_1 \cdot H_2$ where $h_j = 1$ for $\forall j \in J$, are used in ML-EM algorithm to reconstruct the beta image.

Gamma alone

The coincidence-gamma data ($i \in \{\Gamma\}$) and the typical coincidence-gamma system matrix [92] are used in ML-EM algorithm to reconstruct the gamma image.

2.4.2 Joint Reconstruction

Two ways of combining the two sets of beta and coincidence-gamma data are proposed.

Complete beta reconstruction.

The beta data ($i \in \{\mathrm{B}\}$) and a complete beta system matrix, i.e., $H_\beta = H_1 \cdot H_2$, are used in ML-EM algorithm to reconstruct the complete beta image.

Therefore, images from the two separate reconstruction methods (Section 2.4.1) are used to calculate H_2, as explained in Section 2.3.1.

Joint beta and gamma reconstruction.

We use both beta and coincidence-gamma data, a complete beta system matrix, and the coincidence-gamma system matrix in ML-EM algorithm to reconstruct the joint image.

Upon the common emission tomography statistical image reconstruction framework [91, 67], We derive the joint beta and gamma image reconstruction in which a weighted sum of two likelihood functions is maximized under non-negativity constraints.

$$\begin{aligned}
\hat{\mathbf{v}} &= \arg\ \max_{\mathbf{v}}\ L(\mathbf{d}_\gamma|\mathbf{v}) + \alpha L(\mathbf{d}_\beta|\mathbf{v}) \\
&= \arg\ \max_{\mathbf{v}}\ \sum_{i\in\Gamma} d_i \log\left[H\mathbf{v}\right]_i - \left[H\mathbf{v}\right]_i + \alpha\left(\sum_{i\in\mathrm{B}} d_i \log\left[H\mathbf{v}\right]_i - \left[H\mathbf{v}\right]_i\right) \\
&= \arg\ \max_{\mathbf{v}}\ \sum_{i\in\Gamma} d_i \log\left(\sum_j h_{ij}v_j\right) - \left(\sum_j h_{ij}v_j\right) \\
&+ \alpha\left(\sum_{i\in\mathrm{B}} d_i \log\left(\sum_j h_{ij}v_j\right) - \left(\sum_j h_{ij}v_j\right)\right)
\end{aligned}$$

$$\text{Subject to}\quad -v_j \leq 0$$

Where $H = \begin{bmatrix} H_\gamma \\ H_\beta \end{bmatrix}$ and the above formulation is an immediate result of assuming $\begin{bmatrix} \mathbf{d}_\gamma \\ \mathbf{d}_\beta \end{bmatrix} \sim$ Poisson$\left(\begin{bmatrix} H_\gamma \\ H_\beta \end{bmatrix} \mathbf{v}\right)$. Following the same procedure as O'Sullivan [83] in the derivation of the alternating minimization algorithm for transmission tomography, which in general is similar to the work of De Pierro [34, 35] for emission tomography, we lift the primary problem to a double optimization problem using the following lemma.

Lemma 1 (Convex Decomposition Lemma)**.**

$$\log\left(\sum_i q_i\right) = \underset{p\in\mathcal{P}}{max} \;\; \sum_i p_i \log\left(\frac{q_i}{p_i}\right) \qquad ; \qquad \mathcal{P} = \left\{p|p_i \geq 0, \sum_i p_i = 1\right\}$$

Using lemma 1 write $\log\left(\sum_j h_{ij}v_j\right) = \max_{\pi_\mathbf{i}} \;\; \sum_j \pi_{ij} \log \frac{h_{ij}v_j}{\pi_{ij}}$ such that $\sum_j \pi_{ij} = 1 \quad \forall i$. So the optimization problem will be lifted to a double maximization problem over $\mathbf{v}$ and the auxiliary variable π:

$$\max_{\mathbf{v}} \;\; \sum_{i\in\Gamma} d_i \;\; \max_{\pi} \sum_j \pi_{ij} \log\frac{h_{ij}v_j}{\pi_{ij}} - h_{ij}v_j + \alpha\left(\sum_{i\in\mathrm{B}} d_i \;\; \max_{\pi} \sum_j \pi_{ij}\log\frac{h_{ij}v_j}{\pi_{ij}} - h_{ij}v_j\right)$$

Equivalently:

$$\max_{\mathbf{v}} \;\; \max_{\pi} \;\; \sum_{i\in\Gamma}\sum_j d_i\pi_{ij}\log\frac{h_{ij}v_j}{\pi_{ij}} - h_{ij}v_j + \alpha\left(\sum_{i\in\mathrm{B}}\sum_j d_i\pi_{ij}\log\frac{h_{ij}v_j}{\pi_{ij}} - h_{ij}v_j\right)$$

$$-v_j \leq 0 \qquad \forall j$$

$$\sum_j \pi_{ij} = 1 \qquad \forall i$$

Construct the Lagrangian for the auxiliary parameter π:

$$\begin{aligned}\mathcal{L} = &\sum_{i\in\Gamma}\sum_j d_i\pi_{ij}\log\frac{h_{ij}v_j}{\pi_{ij}} - h_{ij}v_j + \alpha\left(\sum_{i\in\mathrm{B}}\sum_j d_i\pi_{ij}\log\frac{h_{ij}v_j}{\pi_{ij}} - h_{ij}v_j\right)\\ &+\sum_i \lambda_i\left(\sum_j \pi_{ij} - 1\right)\end{aligned}$$

Take the gradient with respect to π_{ij} and equate to zero:

$$\frac{\partial}{\partial \pi_{ij}}\mathcal{L}=0 \quad \Rightarrow \begin{cases} d_i\left(\log\frac{h_{ij}v_j}{\pi_{ij}}-1\right)=\lambda_i & i\in\Gamma \\ d_i\left(\log\frac{h_{ij}v_j}{\pi_{ij}}-1\right)=\frac{\lambda_i}{\alpha} & i\in \mathrm{B} \end{cases} \quad \Rightarrow \begin{cases} \pi_{ij}=\frac{h_{ij}v_j}{e^{1+\frac{\lambda_i}{d_i}}} & i\in\Gamma \\ \pi_{ij}=\frac{h_{ij}v_j}{e^{1+\frac{\lambda_i}{\alpha d_i}}} & i\in \mathrm{B} \end{cases}$$

Enforce the equality constraint on π:

$$\sum_j \pi_{ij}=1 \Rightarrow \pi_{ij}=\frac{h_{ij}v_j}{\sum_{j'}h_{ij'}v_{j'}}$$

Similarly for $\mathbf{v}$:

$$\mathcal{L}=\sum_{i\in\Gamma}\sum_j d_i\pi_{ij}\log\frac{h_{ij}v_j}{\pi_{ij}}-h_{ij}v_j+\alpha\left(\sum_{i\in \mathrm{B}}\sum_j d_i\pi_{ij}\log\frac{h_{ij}v_j}{\pi_{ij}}-h_{ij}v_j\right)-\sum_j \mu_j v_j$$

$$\frac{\partial}{\partial v_j}\mathcal{L}=0 \quad \Rightarrow \sum_{i\in\Gamma}\frac{d_i\pi_{ij}}{v_j}-h_{ij}+\alpha\left(\sum_{i\in \mathrm{B}}\frac{d_i\pi_{ij}}{v_j}-h_{ij}\right)=\mu_j$$

Complementary slackness condition for the inequality constraint requires that:

$$\mu_j v_j=0 \qquad \forall j\in J$$

$$\Rightarrow \left(\sum_{i\in\Gamma}\frac{d_i\pi_{ij}}{v_j}-h_{ij}+\alpha\left(\sum_{i\in \mathrm{B}}\frac{d_i\pi_{ij}}{v_j}-h_{ij}\right)\right)v_j=0$$

Meaning that if $v_j\neq 0$, then:

$$v_j=\frac{1}{\sum_{i\in\Gamma}h_{ij}+\alpha\sum_{i\in \mathrm{B}}h_{ij}}\left(\sum_{i\in\Gamma}d_i\pi_{ij}+\alpha\sum_{i\in \mathrm{B}}d_i\pi_{ij}\right)$$

This is an alternating algorithm which starts with an initial value for $\mathbf{v}$ and will alternate between π and $\mathbf{v}$ in the following manner:

$$\pi_{ij}^{(k)} = \frac{h_{ij} v_j^{(k)}}{\sum_{j'} h_{ij'} v_{j'}^{(k)}} \qquad v_j^{(k+1)} = \frac{1}{\sum_{i\in\Gamma} h_{ij} + \alpha \sum_{i\in\mathrm{B}} h_{ij}} \left(\sum_{i\in\Gamma} d_i \pi_{ij}^{(k)} + \alpha \sum_{i\in\mathrm{B}} d_i \pi_{ij}^{(k)} \right)$$

The above two steps can be summarized into one single step.

$$v_j^{(k+1)} = \frac{1}{\sum_{i\in\Gamma} h_{ij} + \alpha \sum_{i\in\mathrm{B}} h_{ij}} \left(\sum_{i\in\Gamma} d_i \frac{h_{ij} v_j^{(k)}}{\sum_{j'} h_{ij'} v_{j'}^{(k)}} + \alpha \sum_{i\in\mathrm{B}} d_i \frac{h_{ij} v_j^{(k)}}{\sum_{j'} h_{ij'} v_{j'}^{(k)}} \right)$$

The final ML-EM step is :

$$v_j^{(k+1)} = \frac{v_j^{(k)}}{\sum_{i\in\Gamma} h_{ij} + \alpha \sum_{i\in\mathrm{B}} h_{ij}} \left(\sum_{i\in\Gamma} h_{ij} \frac{d_i}{\sum_{j'} h_{ij'} v_{j'}^{(k)}} + \alpha \sum_{i\in\mathrm{B}} h_{ij} \frac{d_i}{\sum_{j'} h_{ij'} v_{j'}^{(k)}} \right) \tag{2.2}$$

First-order [9] KKT [10] conditions for $L(\mathbf{d}|\mathbf{v})$ require that:

$$0 = -v_j \cdot \frac{\partial L(\mathbf{d}|\mathbf{v})}{\partial v_j} = v_j \cdot \left(\sum_{i\in\Gamma} h_{ij} - \sum_{i\in\Gamma} \frac{d_i h_{ij}}{\sum_{j'} h_{ij'} v_{j'}} + \alpha \left(\sum_{i\in\mathrm{B}} h_{ij} - \sum_{i\in\mathrm{B}} \frac{d_i h_{ij}}{\sum_{j'} h_{ij'} v_{j'}} \right) \right)$$

$$\Rightarrow \begin{cases} \sum_{i\in\Gamma} h_{ij} - \sum_{i\in\Gamma} \frac{d_i h_{ij}}{\sum_{j'} h_{ij'} v_{j'}} + \alpha \left(\sum_{i\in\mathrm{B}} h_{ij} - \sum_{i\in\mathrm{B}} \frac{d_i h_{ij}}{\sum_{j'} h_{ij'} v_{j'}} \right) = 0 & if \;\; v_j > 0 \\ \sum_{i\in\Gamma} h_{ij} - \sum_{i\in\Gamma} \frac{d_i h_{ij}}{\sum_{j'} h_{ij'} v_{j'}} + \alpha \left(\sum_{i\in\mathrm{B}} h_{ij} - \sum_{i\in\mathrm{B}} \frac{d_i h_{ij}}{\sum_{j'} h_{ij'} v_{j'}} \right) \geq 0 & if \;\; v_j = 0 \end{cases} \tag{2.3}$$

Now if $v_j^{(k)}$ is a fixed point of equation 2.2, then $v_j^{(k)} = v_j^{(k+1)}$, that yields:

$$\Rightarrow \begin{cases} \sum_{i\in\Gamma} \frac{d_i h_{ij}}{\sum_{j'} h_{ij'} v_{j'}^{(k)}} + \alpha \sum_{i\in\mathrm{B}} \frac{d_i h_{ij}}{\sum_{j'} h_{ij'} v_{j'}^{(k)}} = \sum_{i\in\Gamma} h_{ij} + \alpha \sum_{i\in\mathrm{B}} h_{ij} & if \;\; v_j^{(k)} > 0 \\ \sum_{i\in\Gamma} \frac{d_i h_{ij}}{\sum_{j'} h_{ij'} v_{j'}^{(k)}} + \alpha \sum_{i\in\mathrm{B}} \frac{d_i h_{ij}}{\sum_{j'} h_{ij'} v_{j'}^{(k)}} \geq \sum_{i\in\Gamma} h_{ij} + \alpha \sum_{i\in\mathrm{B}} h_{ij} & if \;\; v_j^{(k)} = 0 \end{cases}$$

---

[9] Necessary conditions

[10] Karush-Kuhn-Tucker

Which are equal to 2.3 if v_j is replaced with $v_j^{(k)}$

See Tables 1.1 and 2.1 for the definition of the variables.

2.4.3 Structural Similarity (SSIM)

An objective assessment of the image quantification of the jointly reconstructed image can be achieved by using the structural similarity (SSIM) approach [114]. The SSIM index employs a full reference method for assessing perceptual difference between two images. It compares the local patterns of pixel intensities. The SSIM index is composed of a luminance comparison index, a contrast comparison index, and a structural comparison index. In this study, all three terms are weighted equally. The SSIM index between image 1 ($\mathbf{v_1}$) and image 2 ($\mathbf{v_2}$) is formulated in Equation 2.4, where $\sigma_{1,2}$ is the correlation between the two images and is defined as $\frac{1}{|J|-1}\sum_j (v_{1j}-\mu_1)(v_{2j}-\mu_2)$.

$$\mathrm{SSIM}(\mathbf{v_1},\mathbf{v_2}) = \left[\frac{2\mu_1\mu_2}{{\mu_1}^2+{\mu_2}^2}\right]\cdot\left[\frac{2\sigma_1\sigma_2}{{\sigma_1}^2+{\sigma_2}^2}\right]\cdot\left[\frac{\sigma_{1,2}}{\sigma_1\sigma_2}\right] = \left[\frac{2\mu_1\mu_2}{{\mu_1}^2+{\mu_2}^2}\right]\cdot\left[\frac{2\sigma_{1,2}}{{\sigma_1}^2+{\sigma_2}^2}\right] \tag{2.4}$$

Where:

$$\mu = \frac{1}{|J|}\sum_j v_j$$

$$\sigma = \sqrt{\left(\frac{1}{|J|-1}\sum_j (v_j-\mu)^2\right)}$$

Are, in order, the mean and standard deviation of an image. See Tables 1.1 and 2.1 for the definition of the variables.

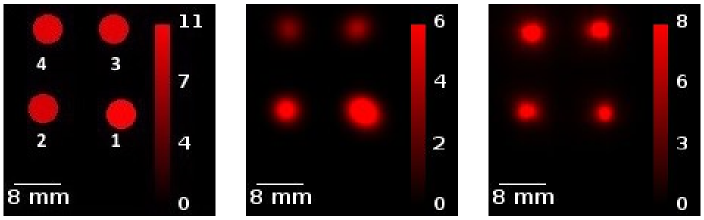

(a) True map **(b)** Beta alone reconstruction **(c)** Gamma alone reconstruction

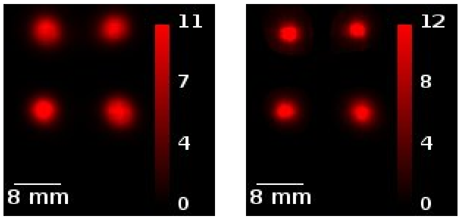

(d) Complete beta reconstruction **(e)** Joint beta and gamma reconstruction

Figure 2.14. Point source images are reconstructed from simultaneous beta and coincidence-gamma data, using ML-EM algorithm. Color bars have unit of nCi per image pixel.

2.5 Physics Model Validation

As it is claimed, the two pieces of data, the beta and coincidence-gamma data, collectively should yield more quantitative images than either of the two considered alone. To show that, we have done a phantom imaging study as well as a plant imaging study to investigate the validity of the physics model and the joint image reconstruction framework.

To cross-check the potential quantification improvement achievable by our model, a simple phantom is made of four point sources of ^{18}F embedded inside a water equivalent medium (transparent adhesive tape) of four thickness variations. The true emission map and the images, reconstructed from the beta and coincidence-gamma data according to the reconstruction schemes described in Section 2.4, are shown in Figure 2.14.

The true and the estimated activity values are shown in Table 2.3. The true activity of each point source is measured using a gamma counter. For each reconstruction method, the estimated activity values are normalized by the maximum value (out of four) and scaled to the true activity of the maximum point source. This is why for each reconstruction method,

Table 2.3. Quantification results for estimated radioactivity of each point source shown in Figure 2.14

	Phantom		Beta		Gamma		Complet beta		Joint(α=1.9)	
#	True activity (μCi)	Medium thickness (mm)	Estimated activity (μCi)	Error %	Estimated activity (μCi)	Error %	Estimated activity (μCi)	Error %	Estimated activity (μCi)	Error %
1	3.398	0.10	3.398	0	1.987	42	3.398	0	3.025	11
2	2.858	0.25	1.745	39	2.179	24	3.114	9	2.734	4.4
3	3.016	0.40	1.118	63	2.792	7	2.913	3.4	2.638	12
4	3.026	0.55	0.958	70	3.206	0	3.188	0.6	3.206	0

the maximum estimated activity is equal to the true activity. Quantification of each image in Figure 2.14 can be evaluated by the difference between the estimated activity and the true activity. Percent error values for the estimated activity is equal to the absolute value of difference between true activity and the estimated activity divided by the true activity. The beta alone image becomes less accurate when medium thickness increases as opposed to the gamma alone image, which becomes less accurate when medium thickness decreases. Both separate reconstruction methods are inaccurate. The complete beta and the joint beta and gamma reconstruction methods (as explained in Section 2.4.2) yield relatively accurate estimations of activity.

2.6 Plant Leaf Study

The plant leaf experiment consists of three steps: 1) Have a tomato plant absorb $^{11}CO_2$. 2) Cut the desired leaf, submerge it in water [11] and image it by the PlantPET Imager [113]. 3) Image the leaf by the Simultaneous Beta-Gamma Imager.

A tomato plant was exposed to 6.5 mCi of $^{11}CO_2$ injected into a sealed labeling chamber of $\sim$ 1 L in volume. The tomato plant absorbed the gas for 10 minutes and then the gas was flushed out with fresh air for 10 minutes. For the following PET imaging, the leaf was sandwiched between two 3 mm thick layers of plastic and submerged into water, to effectively eliminate positron escape, and was scanned for 5.5 minutes. The image from the PlantPET Imager serves as our ground truth image for quantitative performance evaluation of the Simultaneous Beta-Gamma Imager and therefore the PET image must be quantitative.

---

[11] The leaf is submerged in water to enforce higher positron annihilation

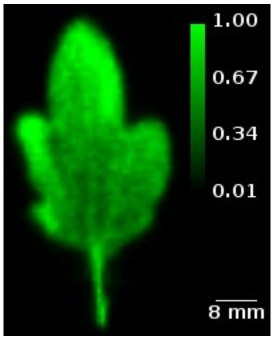

Figure 2.15. PET image of the tomato leaf obtained from the PlantPET Imager, using ML-EM algorithm. The image voxel size is 0.8 mm × 0.8 mm × 0.8 mm. Color bar has unit of normalized value (normalized to the maximum value).

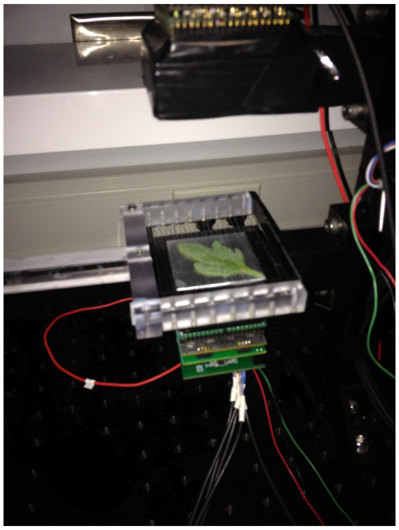

Figure 2.16. The tomato leaf is placed on the Simultaneous Beta-Gamma Imager and data is collected for approximately 2 hours.

Figure 2.15 shows the ground truth image as reconstructed using the ML-EM algorithm with image voxel size of 0.8 mm × 0.8 mm × 0.8 mm [74]. Due to the use of large LSO crystals in the PlantPET scanner and larger voxel size, this image has lower resolution compared to the images from the Simultaneous Beta-Gamma Imager but it has better quantification because of positron escape elimination.

For Beta-Gamma imaging, we placed the leaf on the surface of the phoswich detector (as shown in Figure 2.16) and acquired data for 2 hours. The images are shown in Figure 2.17.

It can be seen from the images shown in Figure 2.17, the joint beta and gamma reconstruction image (Figure 2.17e) and complete beta reconstruction image (Figure 2.17d) resemble the ground truth image in Figure 2.15 better than either of the two separate reconstruction images, i.e., beta alone and gamma alone (Figures 2.17b and 2.17c, respectively). The beta image captures the dominant $^{11}CO_2$ uptake in the leaf but has relatively lower resolution.

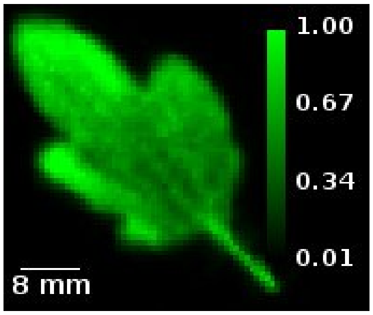

(a) The ground truth image.

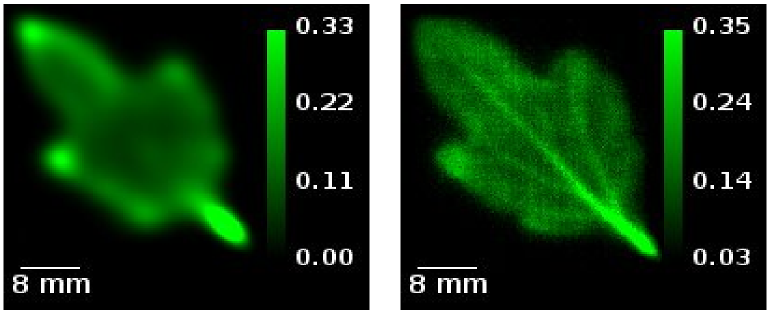

(b) Beta alone reconstruction. SSIM index = 0.33

(c) Gamma alone reconstruction. SSIM index = 0.52

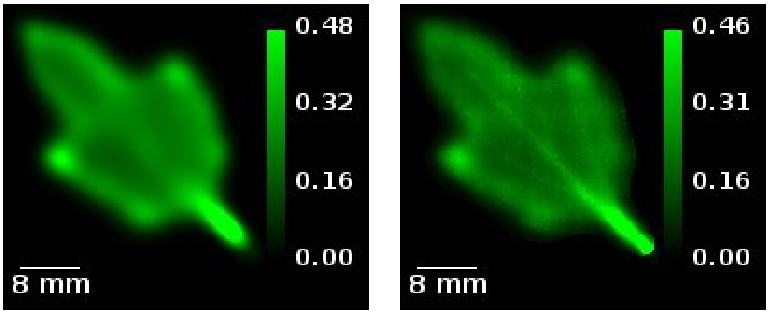

(d) Complete beta reconstruction. SSIM index = 0.69

(e) Joint beta and gamma reconstruction (α=0.45). SSIM index = 0.63

Figure 2.17. Tomato leaf images are reconstructed from the beta and coincidence-gamma data collected by the Simultaneous Beta-Gamma Imager, using ML-EM algorithm. Color bars have unit of normalized value (normalized to the maximum value).

Also it fails to capture the structural features on the midrib and the $^{11}CO_2$ uptake in the veins as opposed to the gamma image in which the veins are visible. The gamma image gives a misleading indication of how the true radioactivity is distributed in the relatively thin regions of the leaf such as the top right edge and the side lobes. The joint beta and gamma image captures both the structural features and $^{11}CO_2$ uptake distribution in the leaf.

The ground truth image in Figure 2.15, co-registered (rotated and resized) with the beta-gamma images (Figure 2.17), was used as the reference image. The SSIM index for each of the images reconstructed from the data acquired by the Simultaneous Beta-Gamma Imager is found to be 0.33, 0.52, 0.69, and 0.63 for *beta*, *gamma*, *complete beta*, and *joint*, respectively. This indicates that the complete beta image and the joint image are more similar to the ground truth image than the beta alone and gamma alone images in terms of structural features.

The complete beta image has a higher SSIM index than the joint image. However, the joint image has a higher resolution than the complete beta image.

2.7 Discussion and Future Work

2.7.1 Increasing the imaging FOV of the beta detector

The non-linearity between the detector response and the physical location for the edge crystals discussed in Section 2.2.2.1 may be corrected by using a look-up table for beta detection. Similar to a flood image experiment and making a look-up table for crystal peak locations for gamma, a collimated beta source can be used to scan the plastic scintillator's entire surface at small increments (e.g. 0.25 mm) in 2D to acquire a histogram and subsequently to find the mapping from the plastic scintillator response to the physical location of the beta source. Using this look-up table for beta, one can increase the imaging FOV of the beta detector, however utilizing the 4.8 cm × 4.8 cm imaging FOV of the beta detector requires optimization of light path from the plastic scintillator to the PMT. Additionally, one may combine multiple phoswich detectors of the same kind to create a large-area simultaneous beta-gamma imager. The system should employ modular design and read out phoswich detectors independently in order to limit (or reduce) dead time and preserve (or even improve) the system count rate capability.

2.7.2 Event classification

Our pulse shape discrimination procedure is not capable of classifying the mixed events from both the plastic scintillator and the LYSO crystal at the same time. The system marks the events falling in between the two thresholds described in Section 2.2.1.2 as *contaminated* events and discards them without any further processing. Classifying contaminated events requires a more complicated algorithm in order to maximize the efficiency of the Simultaneous Beta-Gamma Imager. In this sense, beta events are the ones induced by positrons which escaped from the leaf and interacted with the plastic scintillator. Also, this interaction should not be followed by an annihilation gamma ray being detected by the LYSO crystal or it may result in a contaminated event. In the current implementation, the contaminated events account for 7% of the CFD triggered events. A more sophisticated classifier may improve counting statistics and efficiency of the Simultaneous Beta-Gamma Imager.

2.7.3 $\mathbf{H}_1$ characterization

Modeling and characterization of the plastic scintillator's PSF is worth investigating. Generally H_1 should be such that for a known emission map $\mathbf{v}$ and its corresponding measurement $\mathbf{d}$, the Poisson log likelihood function between the source emission map and the measurement be maximized. If H_1 is modeled as a sum of two 2D Gaussian kernels with parameter $\mathbf{p} = (p_1, p_2, p_3)$, then:

$$\hat{\mathbf{p}} = \arg\max_{\mathbf{p}} \sum_i d_i \log\left(\sum_j h_{ij} v_j\right) - \sum_j h_{ij} v_j$$

In the above optimization problem, h_{ij} must be equal to $\sum_k [H_1]_{ik} [H_2]_{kj}$; however, since the PSF of the plastic scintillator is needed in order to compute the thickness-dependent element of H_2, the source emission map should be designed so that such element be unity.

2.7.4 Joint reconstruction hyperparameter α

The choice of the hyperparameter α that originally appears in the formulation of the optimization problem developed in 2.4.2 may be the topic of a separate study. This value controls the contribution of beta data to the joint beta and gamma reconstruction.

2.8 Conclusion

In this work, we introduce a new imaging modality, Simultaneous Beta-Gamma Imaging. We have designed, assembled, modeled, and tested a prototype. While the application presented for our Simultaneous Beta-Gamma Imager was a quantitative imaging of leaves, the same system can be used to image other thin objects that are challenging for PET systems.

The phantom study results shown in Section 2.5 demonstrate that the physics model proposed in Section 2.3 along with joint image reconstruction framework proposed in Section 2.4 provide more quantification in estimating radioactivity concentration.

Moreover, in a plant leaf study (Section 2.6), we showed that the physics model and the joint image reconstruction are capable of producing images that are both subjectively (visually) and objectively (Structural Similarity Index) more quantitative than gamma alone and beta alone images.

Chapter 3

Virtual-pinhole PET Technology: Surveillance Mode

3.1 Introduction

Since PET spatial resolution can be limited by the detector intrinsic resolution, one way to enhance it, is to reduce the size of the crystals. However, clinical PET scanner manufacturers refrain from using too small scintillation crystals, because the improvement in spatial resolution is limited due to positron annihilation non-collinearity. For a scanner that has a ring diameter of $\geq$ 80 cm, the annihilation non-collinearity effect will limit the resolution to be no better than 0.2 cm FWHM. As a result, using very small scintillation crystals to improve the resolution is not cost-effective. For instance, Siemens uses 0.4 cm × 0.4 cm × 2 cm LSO crystals in Biograph TruePoint®PET-CT scanners.

The clinical desire for higher resolution PET imaging in specific applications, has caused development of PET systems with modified or adjusted geometries such as Positron Emission Mammography (PEM). Thompson *et al* [106, 105] built a dedicated BGO-based PAM device and demonstrated that spatial resolution of about 2 mm and efficiency of about ten times that of a conventional brain scanner were acheivable. Doshi *et al* [43] built a LSO-based modular PET detector for breast imaging and later developed a high-performance PET camera (maxPET) for imaging breast and axilla [44].

Adjusting the PET geometry for particular applications, such as breast and brain imaging, is not the only way to achieve higer resolution and sensitivity. Tai *et al* proposed the Virtual-pinhole (VP) PET [102] in order to investigate an enhancement in spatial resolution and sensitivity. In VP-PET technology, one or more high-resolution PET detector units are integrated into and operate in coincidence with a conventional PET scanner that has lower-resolution detectors. Our group designed, built, and tested 4 VP-PET detectors (*inserts*) and reported $2.40 - 3.24$ mm FWHM spatial resolution [102]. VP-PET effect improves the spatial resolution in the region of interest (ROI) near where the higher-resolution insert has been placed. Mathews *et al* built a half-ring PET insert and demonstrated improvement in image resolution and contrast recovery for breast imaging applications [73].

3.2 Virtual-pinhole PET: Active Mode

In the *active* mode, the PET insert is located inside the scanner's FOV, as shown in Figure 3.1. One of the downsides of the active mode is that the insert, being inside the scanner's FOV, will block some of the scanner's LORs and therefore is considered an attenuating medium that imposes attenuation and scattering on the scanner's LORs. However, high-resolution scanner-insert LORs, obtained from the region of interest, will complement the scanner's loss of LOR.

Since the insert attenuates some of the scanner's LORs, then it must be considered in the attenuation correction of the image reconstruction algorithm. Therefore, the insert's geometry must be included in the attenuation map[12], as shown in Figure 3.2. Overall, the attenuation map is composed of the attenuation map of the patient's body derived from a X-ray CT image and the calculated attenuation map of the VP-PET insert device, as illustrated in Sections 4.2 and 4.3 of [62].

---

[12] The attenuation coefficient map of image voxels at 511 keV.

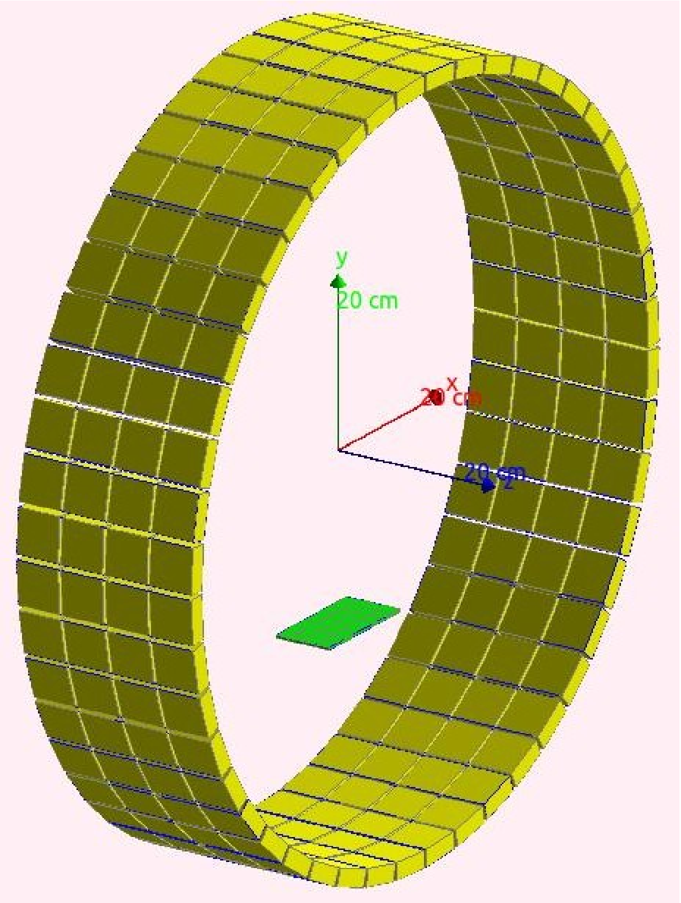

Figure 3.1. Schematic of the PET scanner and the insert in the active mode. The insert is placed inside the scanner's bore.

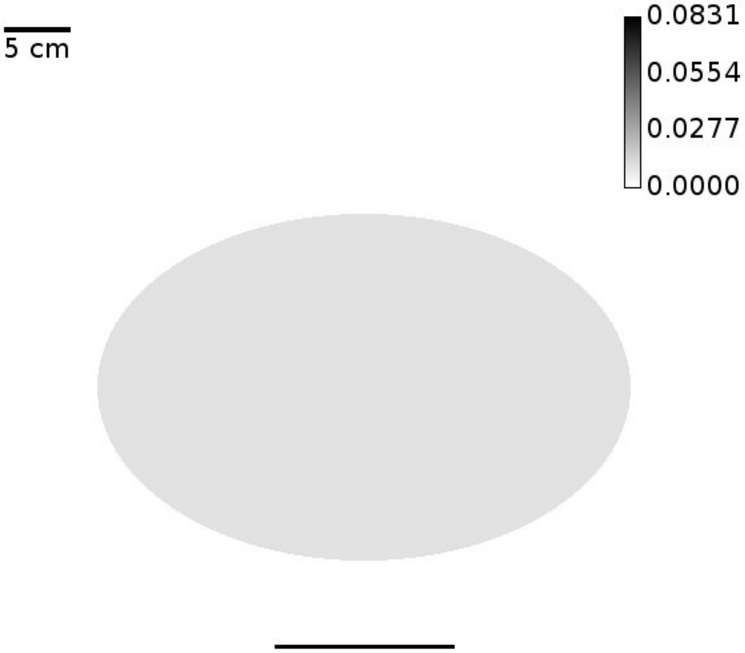

Figure 3.2. Attenuation map used for attenuation correction in the active PET geometry. Attenuation coefficient (at 511 keV) used for the insert is 0.831 cm^{-1} as opposed to 0.096 cm^{-1} for the body. Note that the image voxel size is 0.1 cm × 0.1 cm × 0.1 cm, therfore, 0.831 $\text{cm}^{-1} = 0.0831\ \text{mm}^{-1}$.

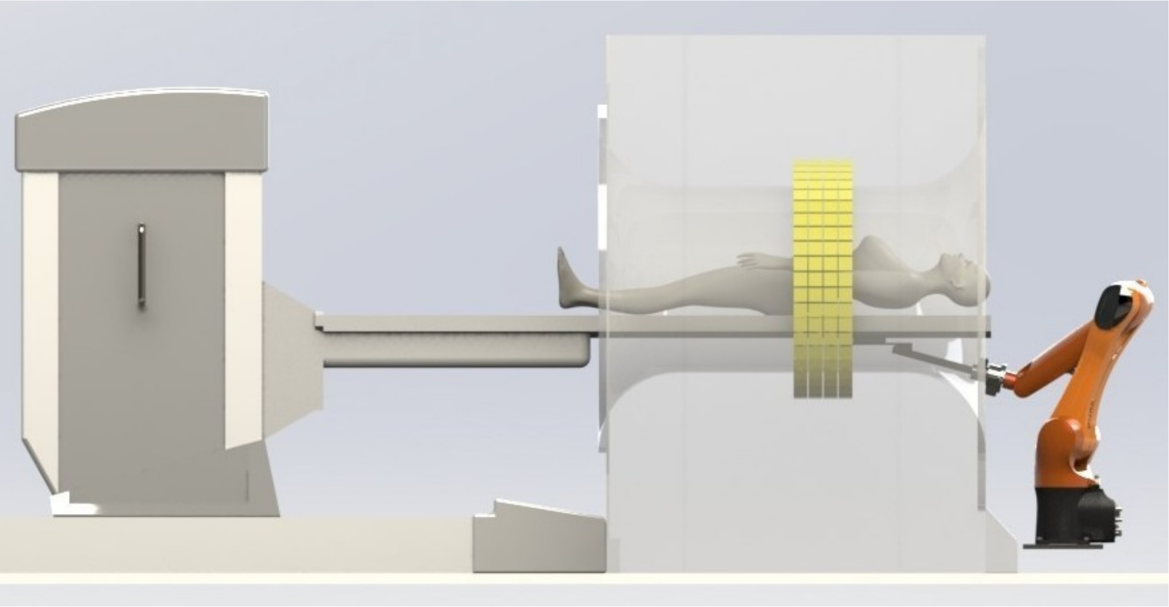

Figure 3.3. Schematic of the surveillance mode imaging setup. The robotic arm holds the PET insert under the bed. The insert collects coincidence events with the scanner from different regions in the patient's body as the bed moves.

3.3 Motivation

The medical application of interest in Chapter 3 is tumor detectability. Virtual-pinhole PET insert has the potential to increase tumor detectability by improving the spatial resolution and the contrast recovery of a conventional PET scanner. However, placing the high-resolution PET insert in the scanner's FOV will introduce other inevitable issues to deal with such as attenuation or handling the insert compliant with clinical standards.

When the PET insert is inside the PET scanner's bore, it shadows a portion of the scanner's crystals, so the number of counts from that portion of the scanner-scanner LORs is significantly attenuated. This has motivated us to propose a new mode of imaging to which we refer as *surveillance* mode. In the surveillance mode imaging regime, the PET insert is placed[13] fixed outside of the PET scanner's gantry and will "closely observe" the regions of interest as the bed moves the patient towards the insert. This illustrated in Figure 3.3.

---

[13] The initial design is to place the insert under the bed mainly because of patient's safety issues. The robotic arm can move the insert to the top in which case the insert is positioned even closer to the body surface.

In this Chapter, we describe a procedure as to achieve a solution to the above task, and details are discussed more specifically in Section 3.5.

Although Chapter 3 is about the *surveillance* mode of the virtual-pinhole PET technology, the reason we described the *active* mode in Section 3.2 is because of its analogy to the surveillance mode.

3.4 Simulation study

3.4.1 Monte Carlo Simulation Package

Among various simulation packages for emission tomography, SimSET (Simulation System for Emission Tomography) is a dedicated code for PET and SPECT simulations [54]. It uses a simplified physics model that is accurate and fast. It is capable of modeling basic detector design. However, it has its own stumbling blocks for users who are willing to explore more than the conventional detector geometries. Also, in SimSET, like all of the other publicly available simulation codes, time is not modeled, which makes it impractical for many time-dependent applications such as kinetics.

The Geant4 package [1, 5, 6] is a more generic Monte Carlo toolkit that simulates the passage of subatomic particles through matter. It is widely used in high-energy, nuclear, and accelerator physics studies. Built on top of Geant4 libraries, GATE (Geant4 Application for Emission Tomography) is a modular, versatile, and scripted Monte Carlo simulation toolkit that overcomes all of the limitations mentioned above. GATE has become the standard for Monte Carlo simulation in the field of nuclear medicine [60, 59].

The user can define the geometry of the PET system as accurately as the position and orientation of the LSO crystals in scripts called GATE macros. It is also possible to define new systems integrated in the coincidence detection wiring of the computer simulation. This has enabled us to define the geometry of the flat-panel insert functioning in coincidence with the PET system.

Furthermore, the user can take advantage of the HepRep (for High Energy Physics REPresentables) file to extract the size, position, and orientation of the detector elements in a hierarchical format. After running the geometry initialization, the following GATE commands are run:

```
Idle> /vis/open HepRepFile
Idle> /vis/viewer flush
```

All the geometrical information will be saved in a file with heprep extension. The HepRep file is in XML format and can be displayed by most web browsers with colorful indenting and coding. HepRep is a hierarchical format: Geant4 volumes have sub-volumes, etc. For example a PET system consists of sectors, sectors have modules, modules have crystals, and cyrstals have LSO (cerium-doped lutetium oxyorthosilicate[14]) or BGO (bismuth germanate[15]) elements. The following tree shows the hierarchy for the geometry used in this study:

---

[14] $Lu_2SiO_5(Ce)$

[15] $Bi_4Ge_3O_{12}$

```
World
|__Scanner
|  |__Sector 1
|  |  |__Module 1
|  |  |  |__Crystal 1
|  |  |  |  |__LSO
|  |  |  |__Crystal 2
|  |  |  |__
|  |  |  |__
|  |  |  |__
|  |  |  |__Crystal 169
|  |  |__Module 2
|  |  |__Module 3
|  |  |__Module 4
|  |__Sector 2
|  |__
|  |__
|  |__
|  |__Sector 48
|__Insert
   |__Sector
      |__Module 1
      |  |__Crystal 1
      |  |  |__LSO
      |  |__
      |  |__
      |  |__
      |  |__Crystal 256
      |__Module 2
      |__
      |__
      |__
      |__Module 32
```

HepRep was not initially developed for Geant4 but it is a generic interface for displaying the detector elements of a GATE simulation.

To read the XML file we utilized the MATLAB® built-in function:

```
DOMnode = xmlread('G4Data0.heprep');
```

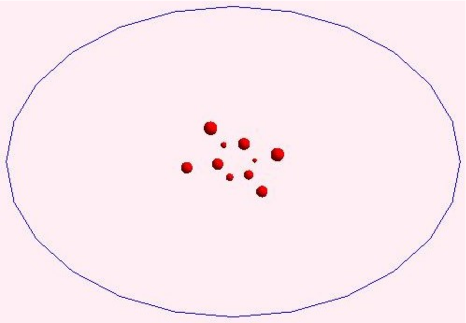

Figure 3.4. Spherical sources of ^{18}F embedded in the background phantom used in the simulation. The background phantom has an elliptical tube shape that is 22 cm long. The base of the tube is an ellipse, which is 40 cm in major axis diameter and 26 cm in minor axis diameter.

Which returns a Document Object Model node (`DOMnode`). In a Document Object Model, every item in an XML file corresponds to a node. The properties and methods for DOM nodes such as `getElementsByTagName('heprep:instance')` and `getChildNodes` are used to extract the geometry information from the scanner all the way down to the LSO elements.

3.4.2 Geometry

All the measurements in Chapter 3 were made using GATE simulation. For both GATE simulation and image reconstruction, the origin of the coordinate system is always in the center of the PET scanner's FOV.

3.4.2.1 Phantom

The phantom consists of spherical sources of ^{18}F embedded in an elliptical cylinder (elliptical tube) with uniform background activity similar to what is shown in Figure 3.4. The size of the elliptical tube is 40 cm × 26 cm × 22 cm in x, y, and z direction, respectively. The cylinder is along the scanner's axial direction. The shape of the phantom resembles the transverse view of a patient's torso lying on the scanner's bed.

The imaging field of view (FOV) is a rectangular box of dimensions: 40 cm × 40 cm × 22.4 cm, as shown in Figure 3.5.

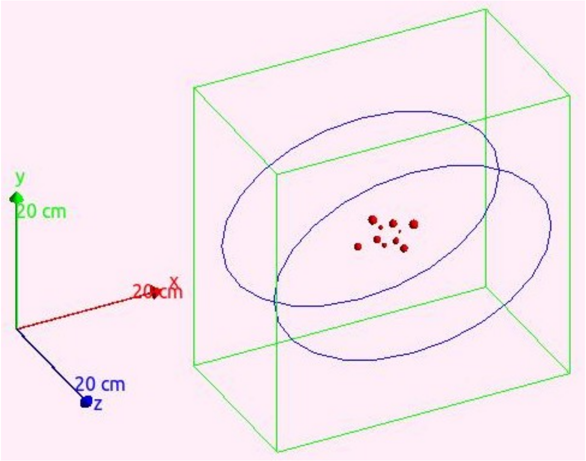

Figure 3.5. The imaging field-of-view (FOV) used for image reconstruction.

3.4.2.2 PET Insert

The PET insert is a flat-panel PET detector with 8 × 4 detector modules. Each module contains 16 × 16 high resolution crystals of size 0.1 cm × 0.1 cm × 0.3 cm. The choice of the crystal size (dimensions) was based on the available detectors in our lab. This insert is shown in Figure 3.6.

3.4.2.3 PET Scanner

The scanner models Siemens Biograph 40 TruePoint® PET/CT with the following geometrical specifications:

- Number of rings: 52
- Ring diameter: 84.2 cm
- Number of crystals: 32,448
- Crystal size: 0.4 cm × 0.4 cm × 2 cm
- Axial field of view: 21.6 cm

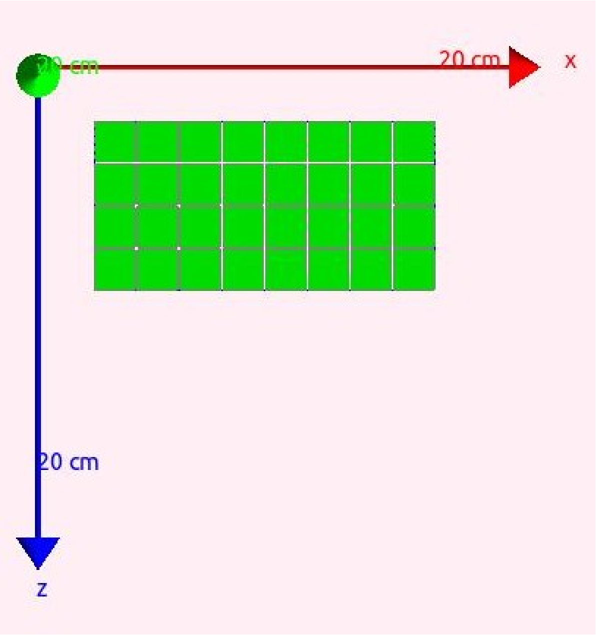

Figure 3.6. The schematic of the flat-panel insert. There are 8 × 4 modules. Each module contains 16 × 16 crystals of size 0.1 cm × 0.1 cm × 0.3 cm.

The imaging FOV is centered with the scanner's coordinate system and the PET insert is positioned in front of the scanner as depicted in Figure 3.7.

3.4.3 Data

The data generated by GATE are singles events from both the scanner and the insert. Since GATE is not capable of generating a coincidence file for the coincidence events between the scanner and the extra system added to the geometry (insert), we have developed our own sorting code that finds the coincidence events in the scanner's singles file and the coincidence events between the scanner's singles file and the insert's singles file. The time window that we have used is 4 nano seconds.

There is coincidence both between the scanner's detectors and between the scanner's detectors and the insert's detectors. we refer to

- the coincidence events between the scanner's crystals as scanner-scanner (SS) events

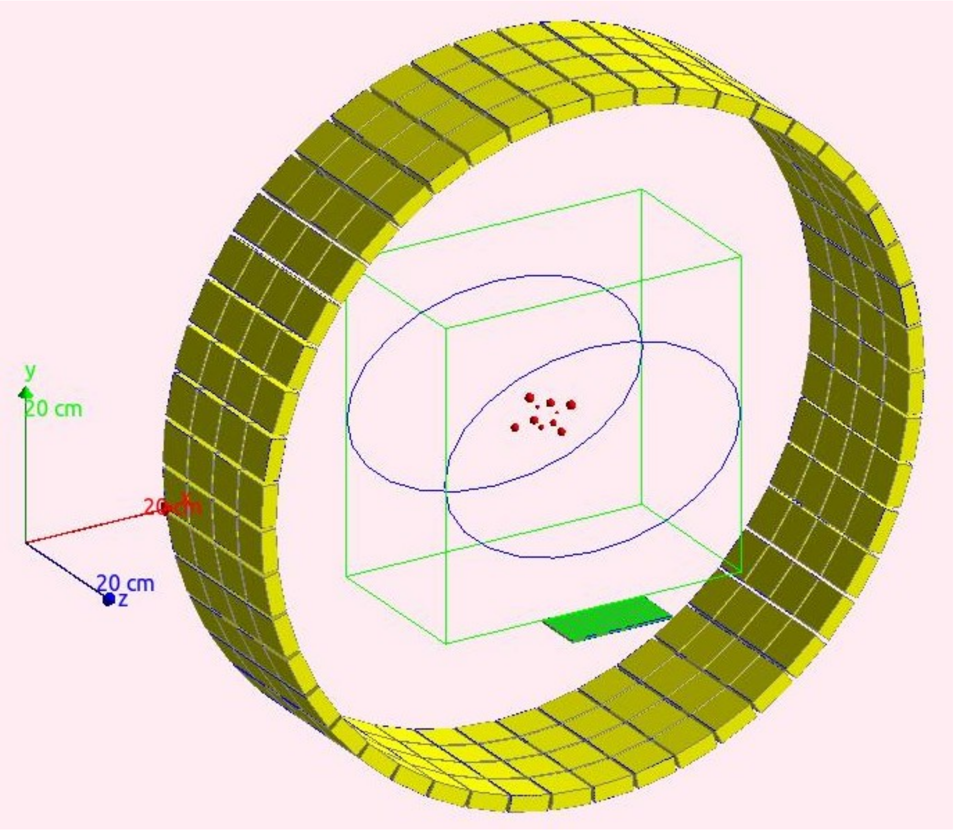

Figure 3.7. The simulation geometry including the PET scanner, the flat-panel insert, the imaging FOV, and a phantom.

- and the coincidence events between the scanner's crystals and insert's crystals as insert-scanner (IS) events.

If the insert had a different shape such that its crystals could constitute any LORs, insert-insert (II) events would exist, too.

3.5 Imaging Regime

The clinical whole-body PET/CT imaging protocol dictates that the patient be scanned in multiple bed positions that are slightly over-lapping and have the same scan duration, e.g. 7 bed positions each taking 3 minutes.

The surveillance mode imaging is fully compliant with the above imaging protocol. The insert is positioned outside of the scanner's axial FOV, and as the patient (bed) moves towards the insert, it collects coincidence events. These coincidence events are marked according to their correspondence with the bed positions. After the full scan, insert data are combined with the scanner data to jointly reconstruct the image.

3.5.1 Detectors set-up

In the surveillance mode imaging, the PET insert is located outside of the PET scanner's FOV. To maximize the sensitivity of the insert device which is to minimize the distance between the insert and the patient's body, and also yet, to keep the insert outside of the scanner's gantry, the insert has been placed right on the edge outside of the scanner's bore (Figure 3.8).

3.5.2 Implementing Surveillance Mode Imaging

In order to demonstrate the feasibility of the surveillance mode imaging technique, I have considered two bed positions that are 12 cm apart along the z-axis:

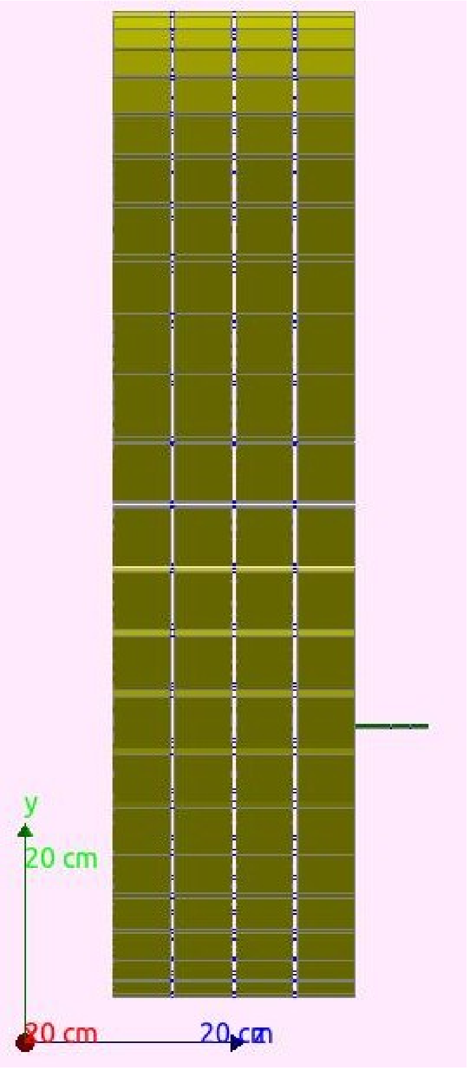

Figure 3.8. The sagittal view of the PET scanner and insert. The insert is placed right on the edge outside of the scanner's bore. The bed moves towards +z-axis

- In *step 1*, the background phantom, described in Section 3.4.2.1, is centered at $z = 0$ cm. Data are acquired for a known time duration, e.g. 3 minutes.
- Then the scanner's bed moves 12 cm towards the positive z-axis. This is *step 2* and the background phantom is now centered at $z = 12$ cm. In this step, data are acquired for the same duration as in *step 1*.

Data from both steps are combined to jointly reconstruct one image into a common image space, as shown in Figure 3.5. The data from *step 2* are added to data from *step 1* by shifting the LORs of *step 2*. The LORs from *step 2* are shifted towards negative z-axis (away from the insert) by the same amount as the bed moved towards positive z-axis, i.e. 12 cm.

3.5.3 Virtual Detectors

In Section 3.5.2, axial shifting of the LORs, acquired in *step 2*, was proposed as a way to add them to the LORs acquired in *step 1*. We have implemented this axial shift by means of virtual detectors: virtual scanner and virtual insert. The virtual detectors are shown in Figure 3.9.

The virtual detectors are identical to the real detectors but are positioned by an axial offset with respect to them. This offset is equal to the bed movement of 12 cm. The reason they are called “virtual” is because they do not exist in data acquisition (simulation) and that they only represent the detectors which constitute the LORs from *step 2*.

We introduced the coincidence data types in Section 3.4.3, i.e. SS and IS events, however, after adding the virtual detectors to the system geometry, one has to differentiate between the coincidence events of the real detectors and the coincidence events of the virtual detectors. We define, similarly:

- the coincidence events between the virtual scanner's crystals as virtual scanner-scanner (vSS) events
- and the coincidence events between the virtual scanner's crystals and the virtual insert's crystals as virtual insert-scanner (vIS) events.

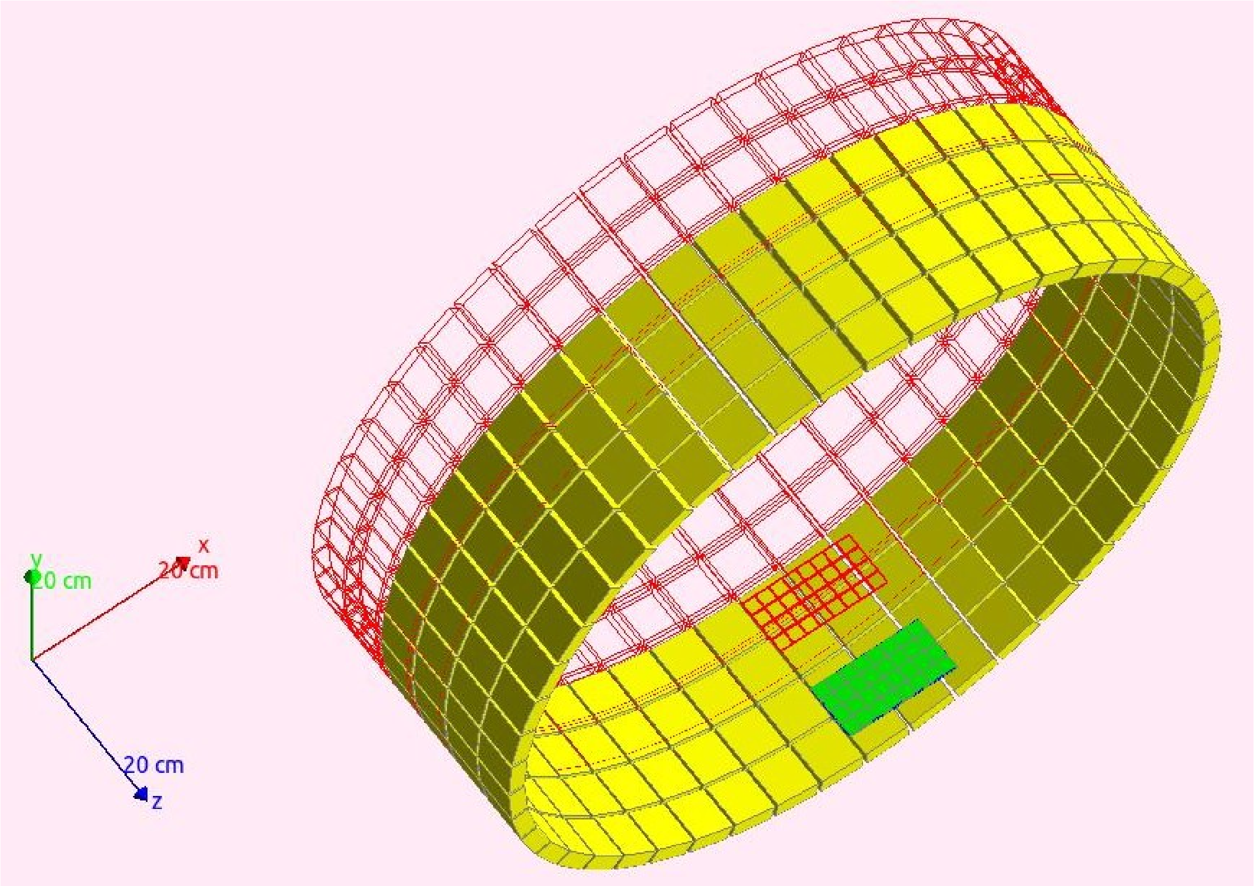

Figure 3.9. Positioning of the virtual detectors: The virtual scanner and the virtual insert are positioned 12 cm, in axial direction, from the scanner and the insert, respectively. Virtual detectors are visualized in hollow red modules. Note that the origin of the coordinate system is always in the center of the scanner's FOV

Therefore, we have 4 types of events: SS, IS, vSS, and vIS. Although we have defined four types of events, we won't use all of the four types for joint image reconstruction at the same time. This is because, when the bed moves to *step 2*, the insert is now imaging the section of the body which was previously centered in the scanner's FOV and which now is moved to a new location viewable by the insert detectors , while the scanner detectors are now imaging a new section of the body.

Therefore, the SS data from *step 1* and the vIS data from *step 2* are used jointly to reconstruct the image for the body section that was initially centered in the scanner's FOV in *step 1.* We currently limit the image reconstruction only to SS and vIS events for all the results presented in Section 3.7.

3.6 Image Reconstruction

The image reconstruction framework used here is a penalized version of the list-mode ML-EM reconstruction algorithm described in Section 1.3.4.

3.6.1 Regularization

Regularization is considered as it is described in Section 1.3.3 and the implementation of the penalty term follows the same procedure as in Section 1.3.3.2. More specifically, using Trust Region Newton's method, the objective function in Equation 3.1 bellow is maximized over all image voxels.

$$E_{\text{penalized}}(\mathbf{d}|\mathbf{v}) = \sum_j v_j^{(n)} u_j^{(n)} \log(v_j) - \sum_j s_j v_j - \beta \sum_j \sum_{\substack{k \in \mathcal{N}_j \\ k \neq j}} \eta_{jk} \phi \left(\frac{v_j - v_k}{\delta} \right) \tag{3.1}$$

In Equation 3.1, $\mathbf{s}$ is the sensitivity image, i.e. $s_j = \sum_i h_{ij}$, and $\mathbf{u}^{(n)}$ is referred to as the update image at the n-th iteration which is defined in Equations 3.2 and 3.3.

- Histogram

$$u_j^{(n)} = \sum_i h_{ij} \frac{d_i}{\sum_{j' \in J_i} h_{ij'} v_{j'}^{(n)}} \tag{3.2}$$

- List-mode

$$u_j^{(n)} = \sum_m h_{i_m j} \frac{1}{\sum_{j' \in J_i} h_{i_m j'} v_{j'}^{(n)}} \tag{3.3}$$

Aside from implementing the maximization of Equation 3.1, choosing the penalty parameters, β and δ are effectively equally important. As mentioned in Section 1.3.3, β controls the relative weight of the penalty term versus the data-fitting term. There is not a systematic procedure to compute the optimal value for β, however, depending on the application or the goal the reconstructed images are supposed to serve, the trade-off between bias and variance has been used to tune β [71]. In list-mode reconstruction, the numerical value of the update image $\mathbf{u}^{(n)}$ in Equation 3.1 depends on the number of coincidence events (as seen in Equation 3.3), therefore, if one seeks the same regularization effect on the reconstructed image from a higher number of coincidence events, they should use a larger value for β.

As mentioned in Section 1.3.3, δ controls the variance (smoothness) imposed on the reconstructed image. This gives us a clue about choosing a proper value for δ. So in order find a proper value for δ, we have used a reconstruction from the background data. The background data are the simulated data from the background phantom described in Section 3.4.2.1 with no tumor sources (background only). The emission decay map[16] of the uniform background is shown in Figure 3.10a.

Using the background data, we reconstruct images with no penalty and study the variations in the image voxels. The attenuation map, used in reconstruction for attenuation correction, is shown in Figure 3.10b. The image at iteration 20 is shown in Figure 3.10c. In order to study the variations in the image voxels, we select only the voxels in the reconstructed image which has non-zero activity by means of the background activity emission decay map shown in Figure 3.10a, and calculate the standard deviation of the reconstructed image. This is conveniently implemented in MATLAB® by:

---

[16] An emission decay map is the true 3-D positions of the origin of all detected counts, obtained from GATE simulation data. We don't use the emission map for image reconstruction but we use it for illustration and image quality analysis purposes.

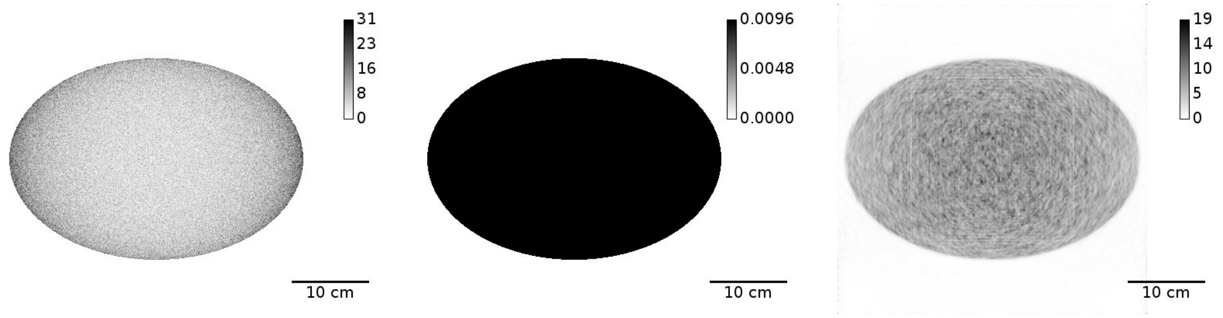

(a) Emission decay map. The color bar represents number of decays per image voxel.

(b) Phantom attenuation map. The color bar represents attenuation coefficient in mm^{-1}.

(c) Reconsrtucted image at iteration 20. The color bar has unit of dps per image voxel.

Figure 3.10. Uniform background phantom. Image voxel size is 0.1 cm × 0.1 cm × 0.1 cm.

```
std(reconMap(decayMap>0));
```

which returns the mathematical value:

$$\sqrt{\frac{1}{\sum_{\substack{j\in J\\ \lambda_j>0}} -1} \sum_{\substack{j\in J\\ \lambda_j>0}} (v_j - m)^2}$$

where m is the mean of the image:

$$m = \frac{1}{\sum_{\substack{j\in J\\ \lambda_j>0}}} \sum_{\substack{j\in J\\ \lambda_j>0}} v_j$$

where λ_j is the emission decay map and v_j is the reconstructed image shown in Figure 3.10c. When we analyze the recontructed images of tumor plus background activity (Section 3.7.2), we exclude (mask out) the tumor voxels in the computation of the mean and variance of the background.

3.6.2 Normalization

In the implementation of the VP-PET imaging, normalization is so essential that one would not be able to obtain a meaningful image if the sensitivity image $\mathbf{s}$ is not properly normalized.

This is because the efficiencies of the two types of detectors, i.e. scanner and insert, in detecting 511-keV gamma rays, are so different that one could not simply use $s_j = \sum_{i \in I_j} h_{ij}$ in the ML-EM algorithm (Equation 1.11).

The normalization described in Section 1.4.1, is comprehensive and includes all elements of normalization such as crystal efficiency and gamma ray interaction angle. However, in this preliminary study, we did not apply normalization in its common sense but only applied crystal efficiencies of two or more types. This crystal efficiency should not be confused with that of the scintillation crystals degrading over time. The two types include scanner's crystals and insert crystals. Therefore, n_i in Equation 1.26, will have as many values as the number of types of coincidence events, in which case is equal to four, because we have SS, IS, vSS, and vIS coincidence events.

$$n_i = \begin{cases} \alpha_{\mathrm{SS}} & i \in I_{\mathrm{SS}} \\ \alpha_{\mathrm{IS}} & i \in I_{\mathrm{IS}} \\ \alpha_{\mathrm{vSS}} & i \in I_{\mathrm{vSS}} \\ \alpha_{\mathrm{vIS}} & i \in I_{\mathrm{vIS}} \end{cases} \tag{3.4}$$

Using Equation 3.4 in the definition of the the sensitivity image yields:

$$s_j = \sum_i h_{ij} n_i \tag{3.5}$$

$$= \alpha_{\mathrm{SS}} \sum_{i \in I_{\mathrm{SS}}} h_{ij} + \alpha_{\mathrm{IS}} \sum_{i \in I_{\mathrm{IS}}} h_{ij} + \alpha_{\mathrm{vSS}} \sum_{i \in I_{\mathrm{vSS}}} h_{ij} + \alpha_{\mathrm{vIS}} \sum_{i \in I_{\mathrm{vIS}}} h_{ij} \tag{3.6}$$

which means the sensitivity image is a weighted sum of the individual sensitivity images $\mathbf{s}^{\mathrm{SS}}$, $\mathbf{s}^{\mathrm{IS}}$, $\mathbf{s}^{\mathrm{vSS}}$, and $\mathbf{s}^{\mathrm{vIS}}$:

$$\mathbf{s} = \alpha_{\mathrm{SS}} \mathbf{s}^{\mathrm{SS}} + \alpha_{\mathrm{IS}} \mathbf{s}^{\mathrm{IS}} + \alpha_{\mathrm{vSS}} \mathbf{s}^{\mathrm{vSS}} + \alpha_{\mathrm{vIS}} \mathbf{s}^{\mathrm{vIS}}$$

The weights in Equation 3.6 are determined by means of a normalization dataset and will be discussed in details in Section 3.6.2.2. Note that in the case that we only use SS and vIS

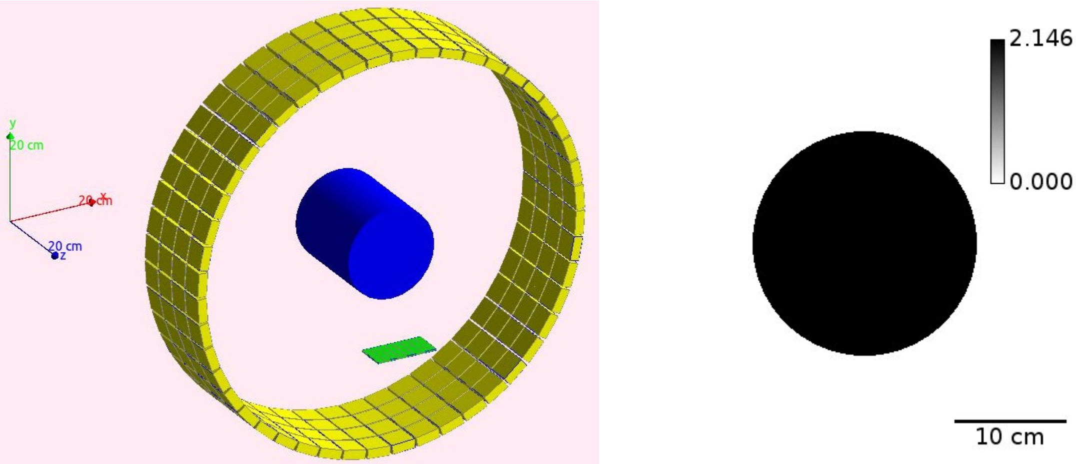

(a) Schematic of the normalization phantom in the center of the scanner.

(b) A xy-plane (z-slice) of the emission map of the normalization phantom. Color bar has unit of dps per image voxel.

Figure 3.11. Normalization phantom: The diameter of the cylinder is 20 cm and its height is 22 cm. Radioactivity is uniformly distributed in the volume and the attenuation medium is water.

coincidence events for joint image reconstruction, as explained in Section 3.5.3, Equation 3.6 may be simplified to:

$$s_j = \alpha_{\text{SS}} \sum_{i \in I_{\text{SS}}} h_{ij} + \alpha_{\text{vIS}} \sum_{i \in I_{\text{vIS}}} h_{ij}$$

3.6.2.1 Normalization phantom

The normalization phantom, used here, has a cylindrical tube shape with a height of 22 cm and a radius of 10 cm. This phantom is schematically shown in Figure 3.11a.

The radioactivity concentration is 100 $\frac{\text{nCi}}{\text{cc}}$. The phantom is placed in the center of the scanner and data are acquired for 10 minutes per *step* (*step* is the same concept as was introduced in Section 3.5.2).

- In *step 1*, the normalization phantom is placed at $x = 0$ cm, $y = 0$ cm, and $z = 0$ cm and data are aquired for 10 minutes. This dataset is used to compute α_{SS} and α_{IS}.

- In *step 2*, the normalization phantom is placed at $x = 0$ cm,$y = 0$ cm, and $z = 12$ cm and data are aquired for 10 minutes. This dataset is used to compute α_{vSS} and α_{vIS}.

3.6.2.2 Computing Weights of Sensitivity Image

In order to calculate the weights in the computation of the sensitivity image as formulated in Equation 3.6, we review our understanding of the sensitivity image based on its definition: $s_j = \sum_i h_{ij}$. s_j is fundamentally proportional to the probability of detection of events in the j-th image voxel of a decay. Thus, for each of the four types of event (SS, IS, vSS, and vIS), the weight will be proportional to the mean number of coincidence counts in the normalization dataset. Therefore, the most intuitive definition for the normalization factors, n_i, is the ratio of the mean number of measured counts (N) divided by the expected mean number of counts ($\bar{n}_i$).

$$n_i = \frac{N}{\bar{n}_i}$$

where:

$$\bar{n}_i = \sum_j h_{ij} v_j^{\mathrm{norm}}$$

$\bar{\mathbf{n}} = H\mathbf{v}^{\mathrm{norm}}$ is the mean forward projected value of the emission map shown in Figure 3.11b.

Following the same procedure for the 4 types of coincidence events, the weights are calculated as:

$$\alpha_{\mathrm{SS}} = \frac{N_{\mathrm{SS}}}{\sum_{i\in I_{\mathrm{SS}}} \bar{n}_i}$$
$$\alpha_{\mathrm{IS}} = \frac{N_{\mathrm{IS}}}{\sum_{i\in I_{\mathrm{IS}}} \bar{n}_i}$$
$$\alpha_{\mathrm{vSS}} = \frac{N_{\mathrm{vSS}}}{\sum_{i\in I_{\mathrm{vSS}}} \bar{n}_i}$$
$$\alpha_{\mathrm{vIS}} = \frac{N_{\mathrm{vIS}}}{\sum_{i\in I_{\mathrm{vIS}}} \bar{n}_i}$$

where N_{SS}, N_{IS}, N_{vSS}, and N_{vIS} are the mean number of measured SS, IS, vSS, and vIS coincidence events, respectively, from the normalization dataset.

The unscaled individual sensitivity images $\mathbf{s}^{\mathrm{SS}}$, $\mathbf{s}^{\mathrm{IS}}$, $\mathbf{s}^{\mathrm{vSS}}$, and $\mathbf{s}^{\mathrm{vIS}}$, already have attenuation correction included, as explained in Section 1.4.3, and more specifically in the denominator of Equation 1.29. Scatter correction is not performed for any of the image reconstruction jobs in this project.

3.7 Results

3.7.1 Resolution

One common way to assess the spatial resolution of a PET scanner is to use spherical sources of various radii in the object being imaged.

The phantom, used in Section 3.7.1, follows the same idea as to demonstrate how “well” one can differentiate the variations in adjacent voxels of the reconstructed image. We evaluate the line profiles of the spherical sources in one plane of the reconstructed image volume.

The plane of the image volume, where all the spherical sources are centered (z_0), is selected for extracting the one-dimensional profiles. In order to demonstrate the resolution enhancement of the surveillance mode image reconstruction, a Derenzo-like-pattern phantom has been

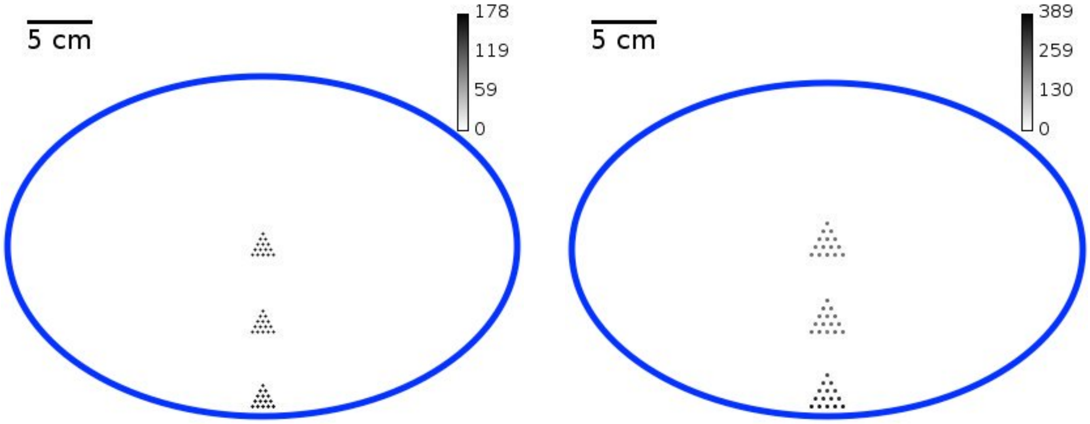

(a) Diameter = 0.2 cm **(b)** Diameter = 0.3 cm

Figure 3.12. Emission decay maps for the spherical-source Derenzo-like-pattern phantoms. The three phantoms are positioned at three vertical locations, 8.45 cm, 14.15 cm, and 20.05 cm from the surface of the insert. The insert is not shown in the maps but is located at the bottom. The distance between the surface of the insert to the body (the oval contour in the figure) is 7 cm. Spacing between the centers of the adjacent spheres, is twice the diameter.

designed and the phantom has been positioned in three distances from the surface of the insert. Figure 3.12 shows all the three locations in one emission decay map.

Figures 3.13 and 3.14 show the reconstructed images and their line profiles through the row with five tumors on it for the phantom shown in Figure 3.12a.

Similarly, Figures 3.15 and 3.16 show the reconstructed images and their line profiles through the row with five tumors on it for the phantom shown in Figure 3.12b. Results show that the resolution of the jointly reconstructed images is the highest for regions close to the flat-panel insert, and the improvement diminishes at a distance of approximately 20 cm from the surface of the flat-panel insert.

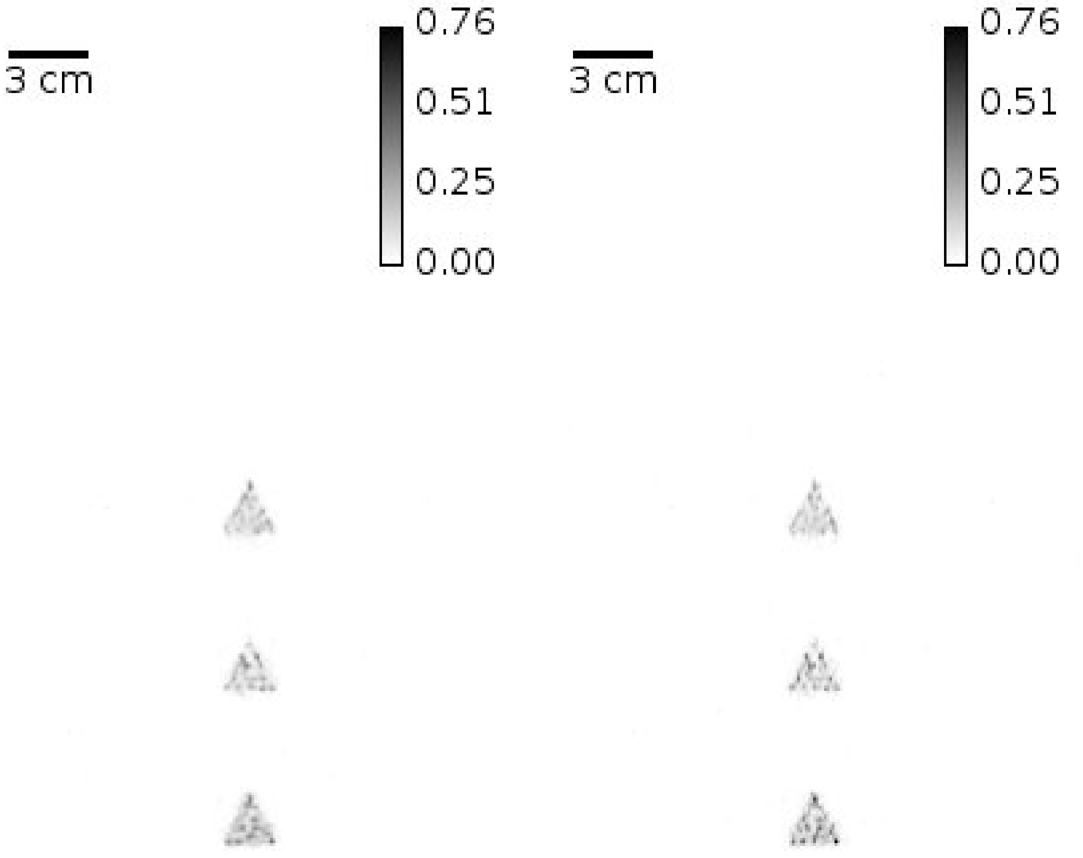

(a) scanner only **(b)** joint

Figure 3.13. Reconstructed images (iteration 30) of the data shown in Figure 3.12a. Diameter of the spheres is 0.2 cm. Color bars have unit of nCi.

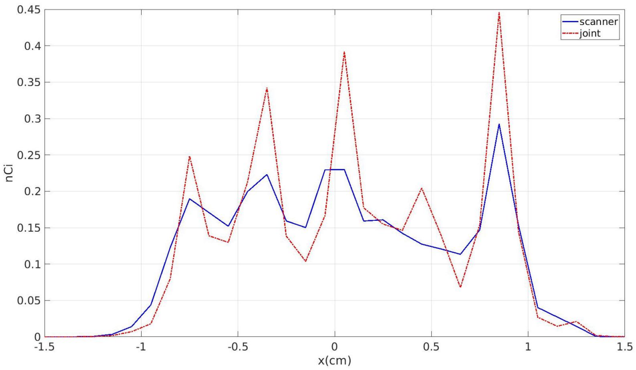

(a) Distance = 8.45 cm

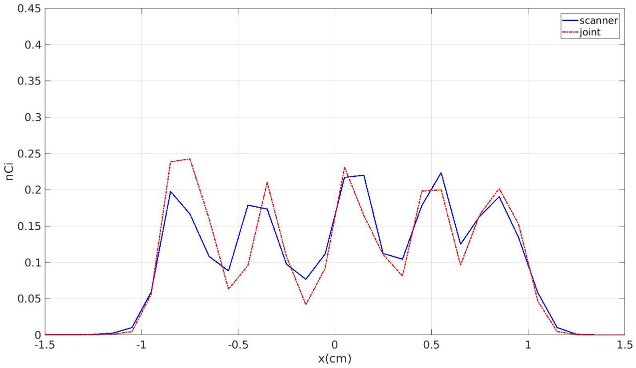

(b) Distance = 14.15 cm

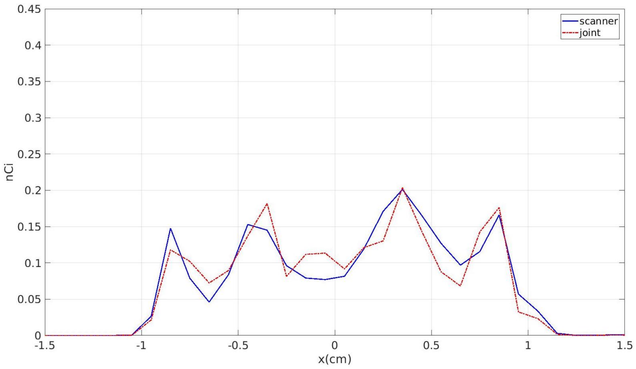

(c) Distance = 20.05 cm

Figure 3.14. The line profiles of the reconstructed images shown in Figure 3.13 along the row with five spheres. Diameter of the spheres is 0.2 cm. Color bars have unit of nCi.

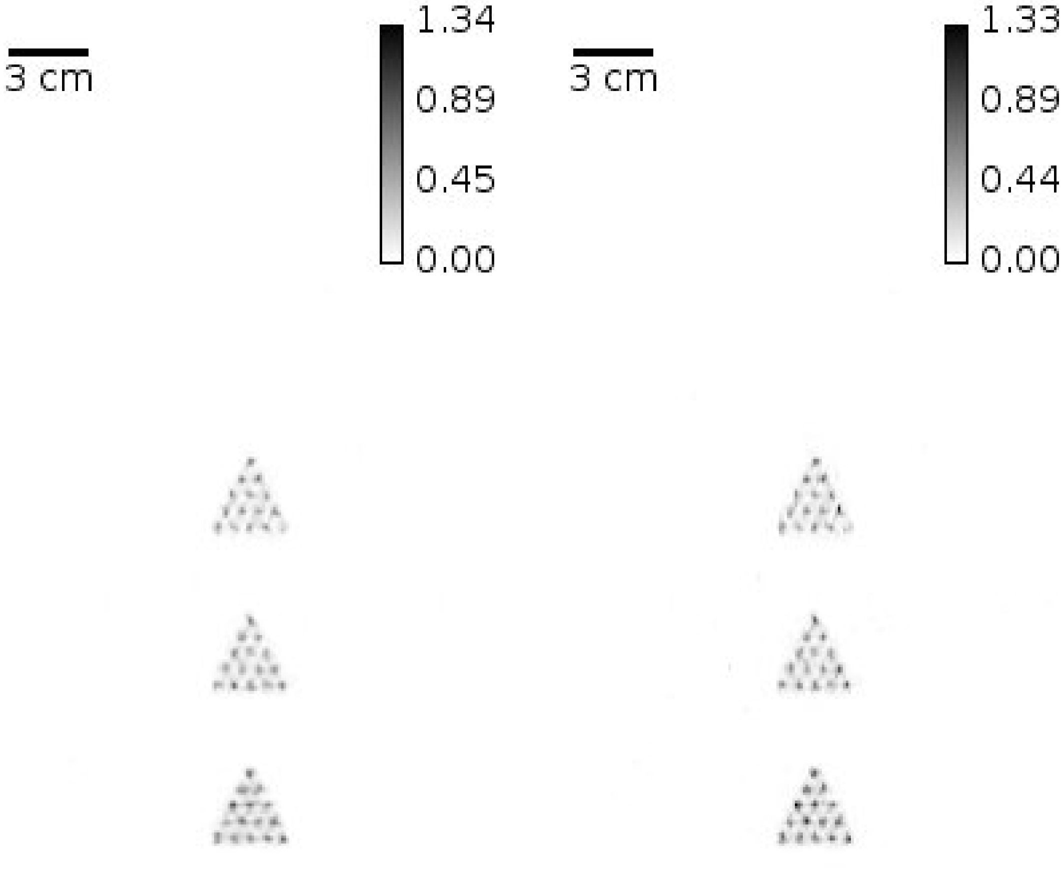

(a) scanner only

(b) joint

Figure 3.15. Reconstructed images (iteration 30) of the data shown in Figure 3.12b. Diameter of the spheres is 0.3 cm. Color bars have unit of nCi.

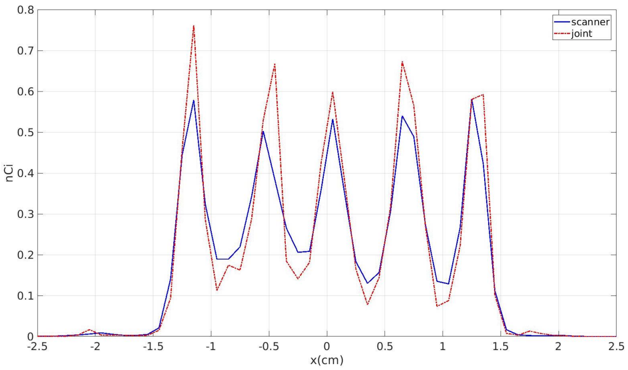

(a) Distance = 8.45 cm

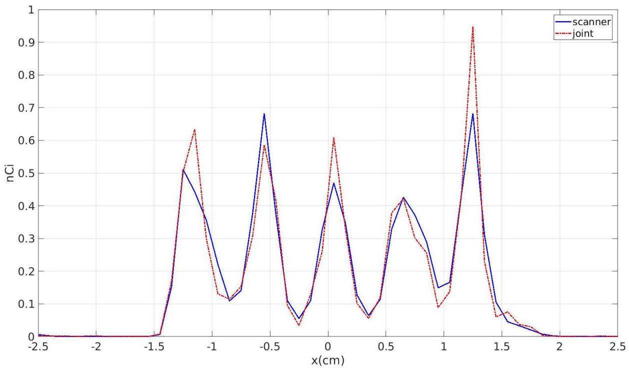

(b) Distance = 14.15 cm

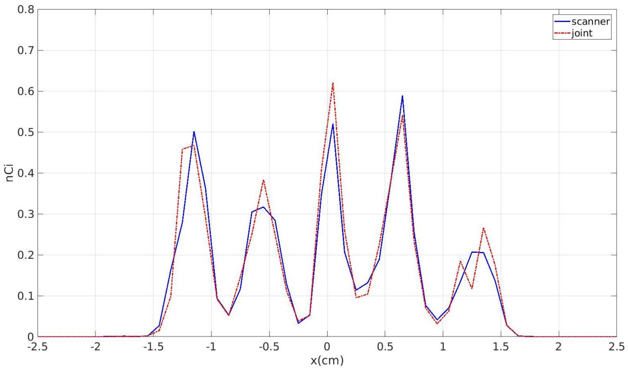

(c) Distance = 20.05 cm

Figure 3.16. The line profiles of the reconstructed images shown in Figure 3.15 along the row with five spheres. Diameter of the spheres is 0.3 cm. Color bars have unit of nCi.

3.7.2 Contrast Recovery

In a real world imaging experiment, there always is background activity. That's why in every imaging study (both experiment and simulation) including the imaging study presented here, the background activity phantom/source is considered.

In order to find the contrast of a reconstructed image, I divide the image voxels into three non-overlapping groups:

- Tumor voxels: The voxels that contain the tumors.
- Background voxels: The voxels that contain the background activity minus the voxels that contain the tumors.
- Outside voxels: All the remaining voxels of the image volume that contain no acivity.

All of the above groups of voxels can be masked out according to the emission decay map shown in Figure 3.17.

We use the mean value of tumor voxels, m_1, and the mean value of background voxels, m_0, in Equation 3.7 to calculate the contrast.

$$\text{Contrast} = \frac{m_1 - m_0}{m_0} \tag{3.7}$$

m_0 and m_1 are defined in Equations 3.8 and 3.9, respectively.

$$m_0 = \frac{1}{\sum_{\substack{j \in J \\ \lambda_{bj} > 0 \\ \lambda_{tj} = 0}}} \sum_{\substack{j \in J \\ \lambda_{bj} > 0 \\ \lambda_{tj} = 0}} v_j \tag{3.8}$$

$$m_1 = \frac{1}{\sum_{\substack{j \in J \\ \lambda_{bj} > 0 \\ \lambda_{tj} > 0}}} \sum_{\substack{j \in J \\ \lambda_{bj} > 0 \\ \lambda_{tj} > 0}} v_j \tag{3.9}$$

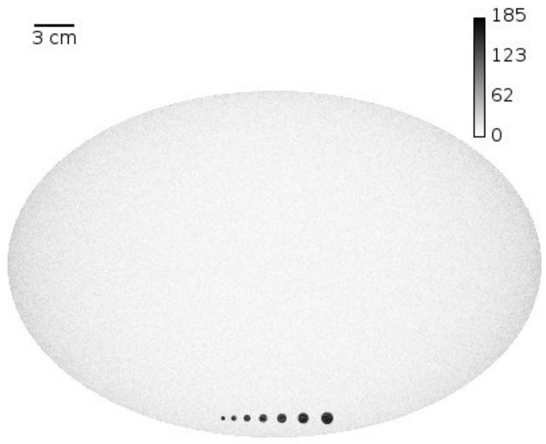

Figure 3.17. The emission decay map of the spherical sources placed near the edge of the body closer to the insert. The diameters of the spherical sources (left to right) are 0.3, 0.4, 0.5, 0.6, 0.7, 0.8, and 0.9 cm. The vertical distance between the centers of the spheres and the surface of the flat-panel insert is 8.5 cm. The tumor-to-background contrast ratio is 12:1.

Note that $\lambda_{\mathbf{b}}$ ($\lambda_{bj}: \ j \in J$) is the background emission decay map and $\lambda_{\mathbf{t}}$ ($\lambda_{tj}: \ j \in J$) is the tumor emission decay map. Also, note that $\lambda_{\mathbf{b}}$ and $\lambda_{\mathbf{t}}$ are readily available only in a simulation study, however for experimental data, one may use a primarily reconstructed image to obtain estimates for $\lambda_{\mathbf{b}}$ and $\lambda_{\mathbf{t}}$[17].

Contrast recovery is defined as the percentage ratio of the contrast of the output to the contrast of the input. Here in Monte Carlo simulation the input is the emission decay map and the output is the reconstructed image. The contrast recovery is defined in Equation 3.10.

$$\text{Contrast Recovery (\%)} = \frac{C_{\mathrm{o}}}{C_{\mathrm{i}}} \times 100 \tag{3.10}$$

- C_{o} is the contrast of the reconstructed image.
- C_{i} is the tumor-to-background contrast ratio specified in the simulations.

---

[17] Only for the tumors that can be confidently perceived.

In order to study contrast recovery enhancement brought by the insert, a simple phantom has been simulated which consists of a row of spherical sources lined up horizontally. The diameters of the spherical sources range from 0.3 cm to 0.9 cm in increments of 0.1 cm, and the distance between the centers of the adjacent spheres is twice the diameter of the larger one. This phantom is shown in Figure 3.17.

Figure 3.18 shows the reconstructed images in surveillance mode, as well as the contrast recovery as a function of spherical tumor size.

The reconstructed images (displayed in Figure 3.18) show that the main challenge is to detect tumors (spheres) of diameters 0.4 cm, 0.5 cm, and 0.6 cm. Therefore, phantoms of spherical sources of the same diameter have been simulated where the spheres are arranged in three rows of 5 spheres, a total of 15 spheres. The rows, in order, are positioned 8.5 cm, 14.5 cm, and 20 cm from the surface of the insert. The phantoms are shown in Figure 3.19.

Using the data set shown in Figure 3.19 for two tumor-to-background contrast ratios of 12:1 and 6:1, we have reconstructed images for *step 1*, and jointly *step 1* and *step 2* together. Figure 3.20 shows the reconstructed images for 12:1 contrast.

Also, Figure 3.21 shows the reconstructed images for 6:1 contrast.

In order to more quantitatively assess the contrast recovery enhancement of images shown in Figures 3.20 and 3.21, contrast recovery is calculated for each of the spherical sources as described in Section 3.7.2 and mainly by Equations 3.7 and 3.10. Figure 3.22 shows contrast recovery versus size of the sphere.

Similar to Section 3.7.1, in order to examine the effect of distance between the tumors and the insert on, in this case, contrast recovery, Figure 3.23 shows contrast recovery versus the distance between the centers of the tumors and the surface of the flat-panel insert.

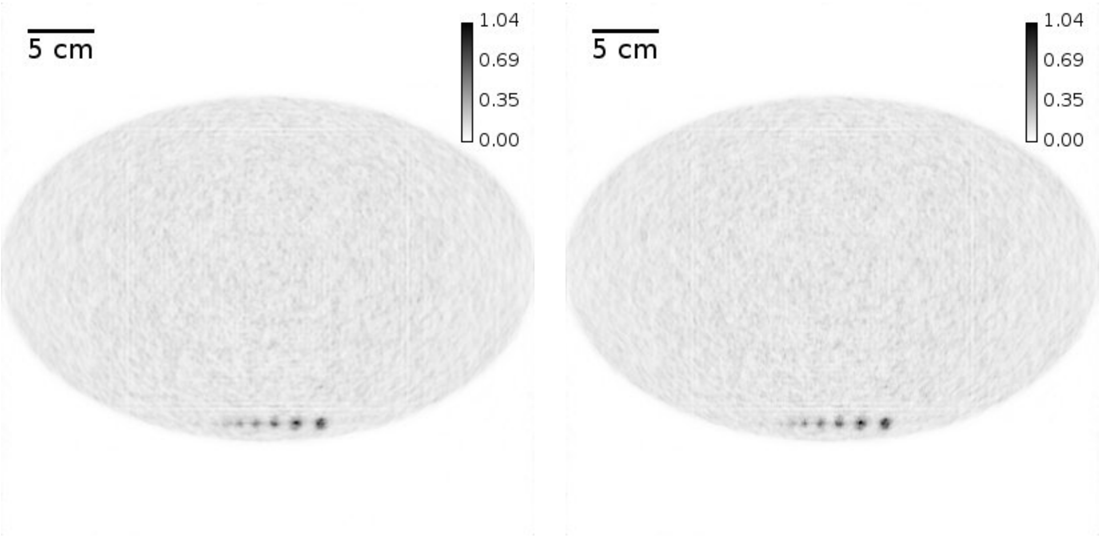

(a) Scanner only **(b)** Joint

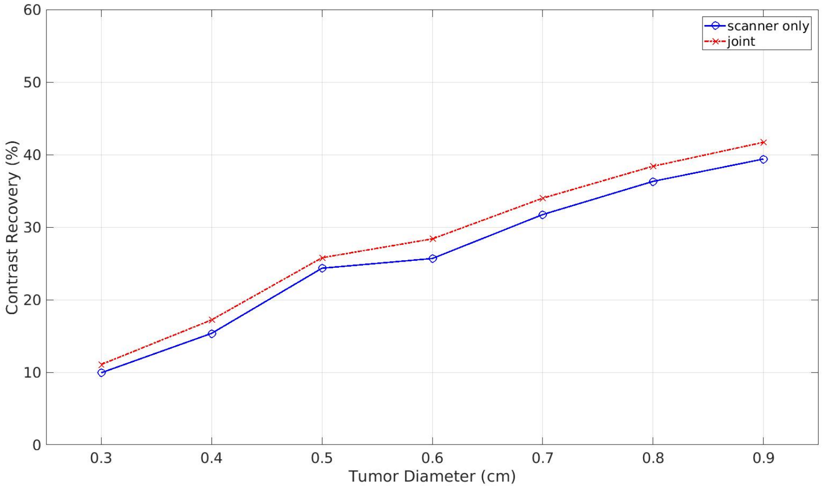

(c) Contrast recovery plot

Figure 3.18. Recontructed images and the contrast recovery plot for the phantom shown in Figure 3.17. Tumor-to-background contrast ratio is 12:1 and reconstruction iteration is 30.

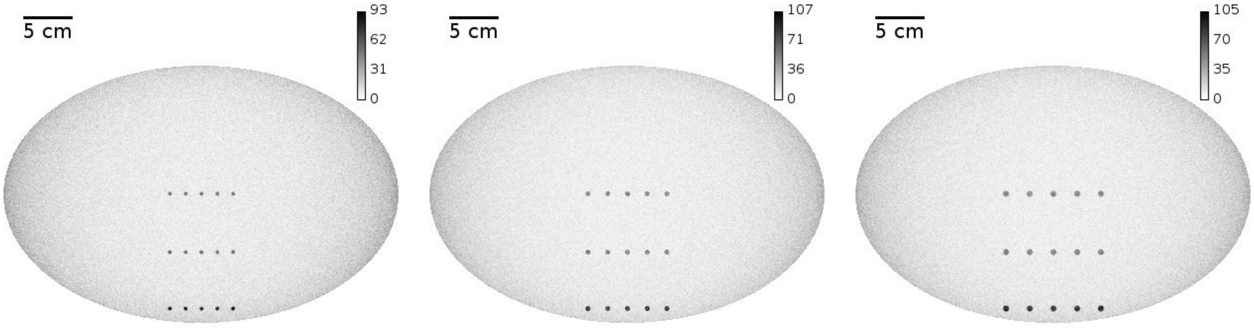

(a) Diameter = 0.4 cm **(b)** Diameter = 0.5 cm **(c)** Diameter = 0.6 cm

Figure 3.19. The emission decay maps for the spherical sources phantom.

3.7.3 SNR

None of the metrics, used in Sections 3.7.1 and 3.7.2, takes into account the image noise. As mentioned in Section 1.5.3, image noise is associated with the variations in the neighboring voxels across the image volume.

The reconstructed image of a uniform source must ideally have flat profiles across the image volume. However, in a real world scenario where noise exists, there are fluctuations in the values of neighboring image voxels. I have used the standard deviation of the background voxels as the representative of the image noise.

Similar to Section 3.7.2, there will be two standard deviation values for each image. One is for the background voxels, that I refer to as δ_0, and one is for the tumor voxels, namely δ_1. The standard deviations are calculated in Equations 3.11 and 3.12 in the same manner as Equations 3.8 and 3.9.

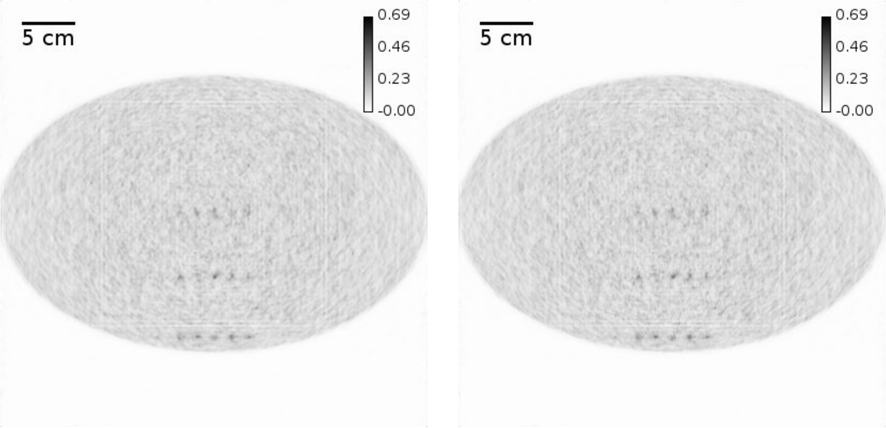

(a) Diameter = 0.4 cm , scanner only.

(b) Diameter = 0.4 cm , joint.

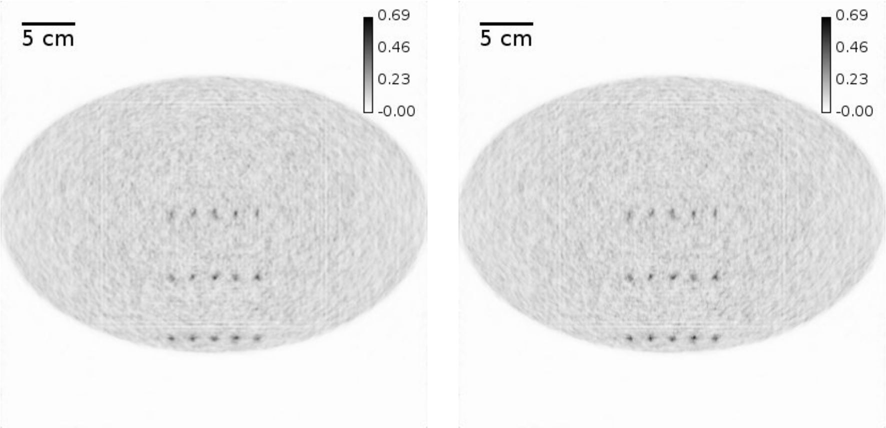

(c) Diameter = 0.5 cm , scanner only.

(d) Diameter = 0.5 cm , joint.

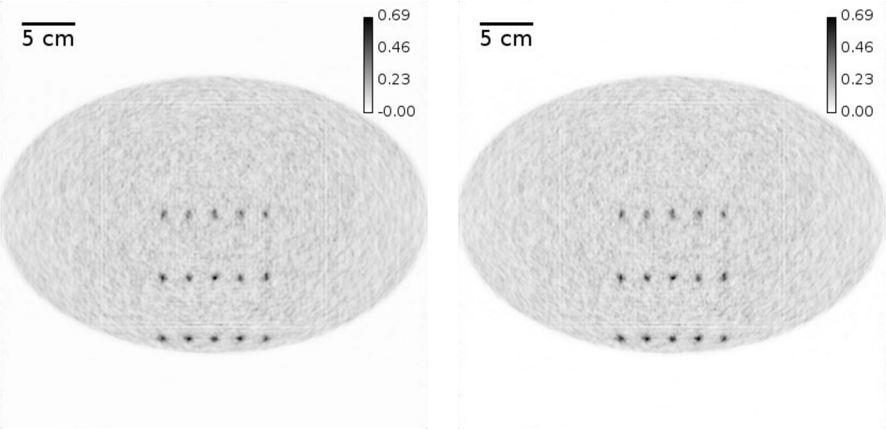

(e) Diameter = 0.6 cm , scanner only.

(f) Diameter = 0.6 cm , joint.

Figure 3.20. Reconstructed images of data set shown in Figure 3.19. Tumor-to-background contrast ratio is 12:1, reconstruction iteration is 30, and the color bar has unit of nCi.

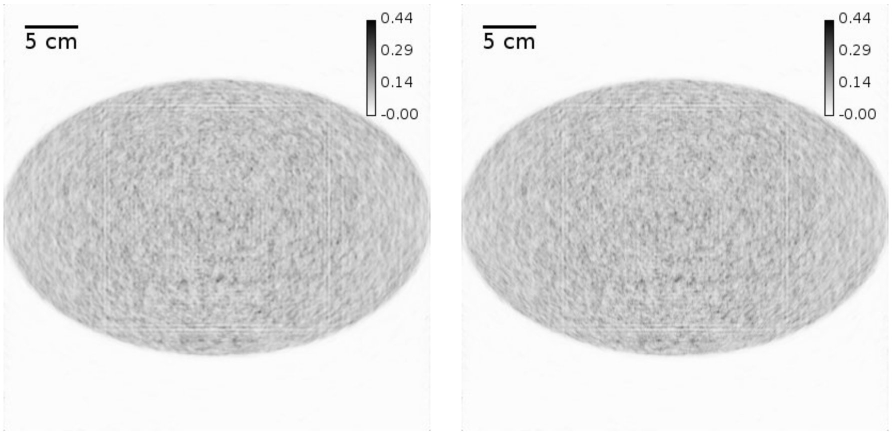

(a) Diameter = 0.4 cm , scanner only.

(b) Diameter = 0.4 cm , joint.

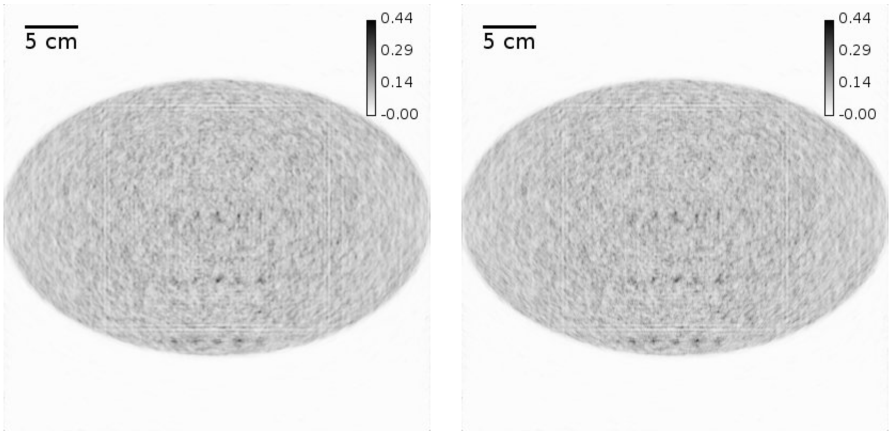

(c) Diameter = 0.5 cm , scanner only.

(d) Diameter = 0.5 cm , joint.

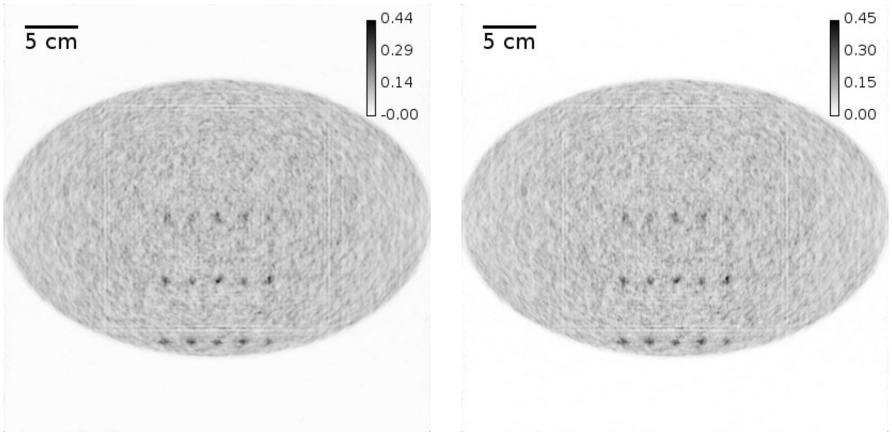

(e) Diameter = 0.6 cm , scanner only.

(f) Diameter = 0.6 cm , joint.

Figure 3.21. Reconstructed images of data set shown in Figure 3.19. Tumor-to-background contrast ratio is 6:1, reconstruction iteration is 30, and the color bar has unit of nCi.

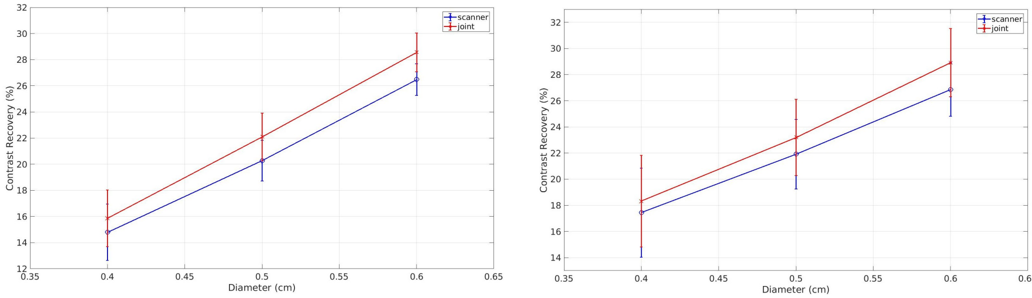

(a) 12:1 contrast **(b)** 6:1 contrast

Figure 3.22. Contrast recovery of the reconstructions shown in Figures 3.20 and 3.21, for the spheres in only the closest row to the flat-panel insert, as a function of sphere size. The error bars are derived by averaging over the five spheres in the row.

$$\delta_0 = \sqrt{\frac{1}{\sum_{\substack{j\in J\\ \lambda_{bj}>0\\ \lambda_{tj}=0}} -1} \sum_{\substack{j\in J\\ \lambda_{bj}>0\\ \lambda_{tj}=0}} (v_j - m_0)^2} \tag{3.11}$$

$$\delta_1 = \sqrt{\frac{1}{\sum_{\substack{j\in J\\ \lambda_{bj}>0\\ \lambda_{tj}>0}} -1} \sum_{\substack{j\in J\\ \lambda_{bj}>0\\ \lambda_{tj}>0}} (v_j - m_1)^2} \tag{3.12}$$

Using the standard deviation as a measure of noise in the image, and mean as a measure of the signal in the image, one may define the signal-to-noise (SNR) ratio as in Equation 3.13.

$$\mathrm{SNR} = \frac{m_1 - m_0}{\frac{1}{2}\delta_1 + \frac{1}{2}\delta_0} \tag{3.13}$$

Using Equation 3.13, the SNR is calculated for the spherical sources in the reconstructed images in Figures 3.20 and 3.21. Figure 3.24 shows SNR versus the tumor size.

Similarly, Figure 3.25 shows SNR versus the vertical distance between the centers of the spherical sources and the surface of the flat-panel insert.

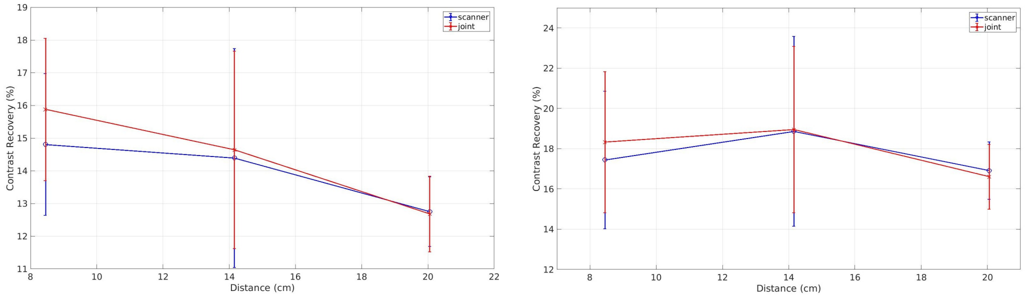

(a) Diameter = 0.4 cm , 12:1 contrast. **(b)** Diameter = 0.4 cm , 6:1 contrast.

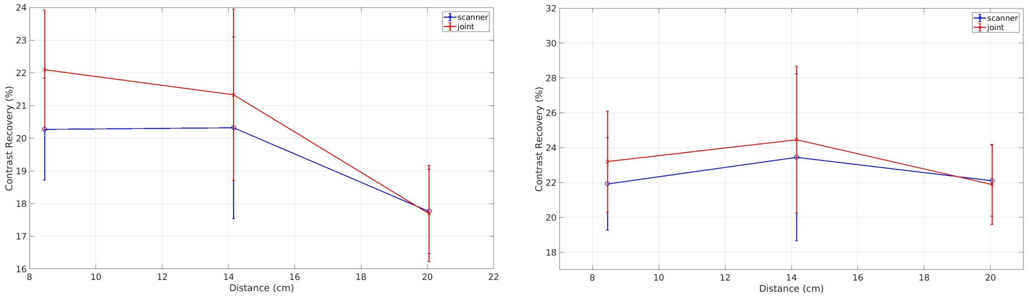

(c) Diameter = 0.5 cm , 12:1 contrast. **(d)** Diameter = 0.5 cm , 6:1 contrast.

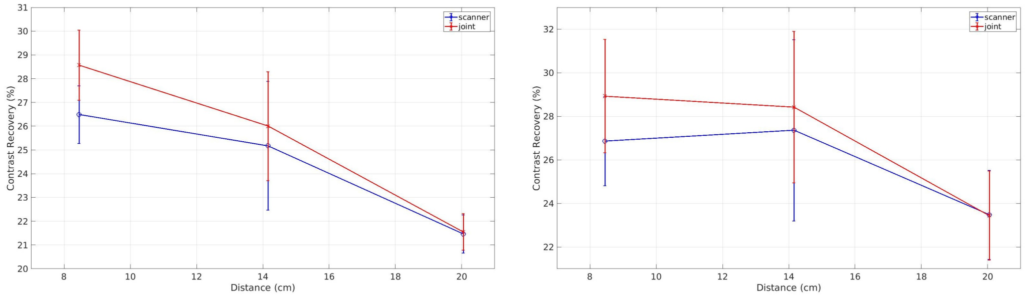

(e) Diameter = 0.6 cm , 12:1 contrast. **(f)** Diameter = 0.6 cm , 6:1 contrast.

Figure 3.23. Contrast recovery of the reconstructions shown in Figures 3.20 and 3.21 as a function of the distance between the centers of the spheres and the surface of the flat-panel insert. The error bars are derived by averaging over the five spheres in the row.

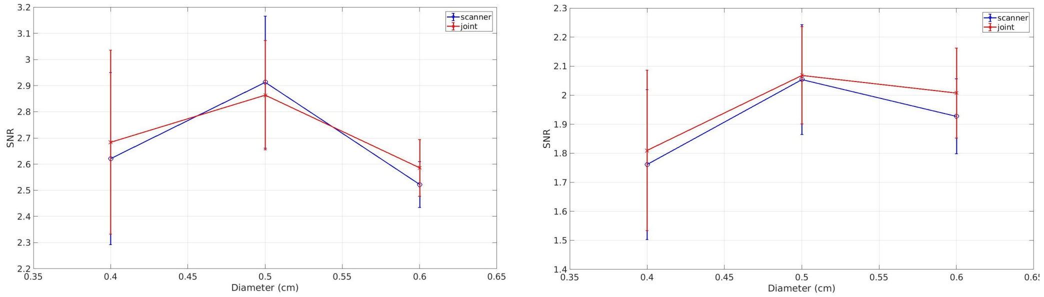

(a) 12:1 contrast **(b)** 6:1 contrast

Figure 3.24. SNR of the reconstructions shown in Figures 3.20 and 3.21, for the spheres in only the closest row to the flat-panel insert, as a function of sphere size. The error bars are derived by averaging the SNR values over the five spheres in the row.

3.8 Discussion and Conclusion

The results presented in Section 3.7 demonstrate that by adding the insert data to the scanner data, one can achieve enhancement in resolution, contrast recovery and SNR "near" the surface of the flat-panel insert. The term "near" is ambiguous, however, empirically our simulation results have suggested that nearness usually translates into distances ranging from 8 cm to 15 cm when using the geometry of the Biograph TruePoint®PET-CT scanner.

The improvement from one small flat panel insert is very limited. This is mainly because the number of IS counts acquired, is much less than that of the SS counts. In the configuration used in the simulations and reconstructions presented in Chapter 3, where the insert is made of 0.3 cm thick crystals and is located 20 cm from the center of the scanner, the insert picks up only less than 4% of total coincidence counts and the remaining 96% and more are SS counts. One way to improve the overall sensitivity of the insert device is to use thicker crystals. Additional studies are needed in order to find the optimal design that balances the resolution and sensitivity characteristics.

Other, yet unmet, challenges include scatter correction which is more essential in larger body phantoms simulation. Previous works of our lab have demonstrated that a small flat-panel insert with limited number of angles of data acquisition, works better for brain-size phantoms as opposed to torso-size ones. Additional investigations to evaluate the optimal geometry and the number of panel detectors will be left for future studies.

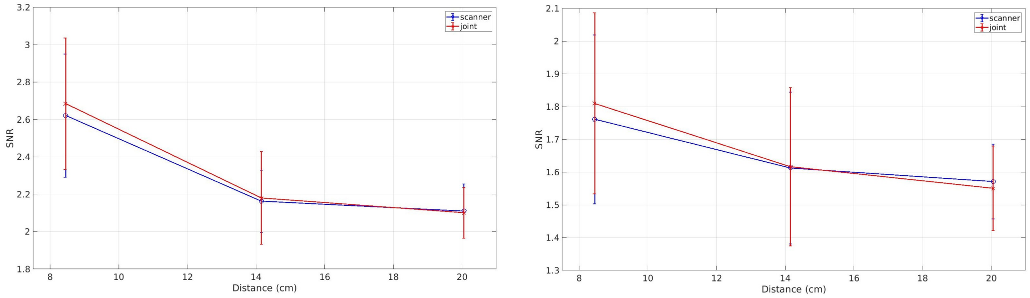

(a) Diameter = 0.4 cm , 12:1 contrast. **(b)** Diameter = 0.4 cm , 6:1 contrast.

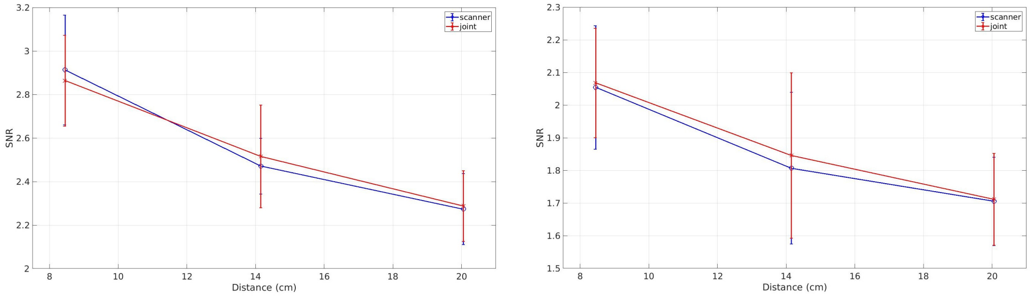

(c) Diameter = 0.5 cm , 12:1 contrast. **(d)** Diameter = 0.5 cm , 6:1 contrast.

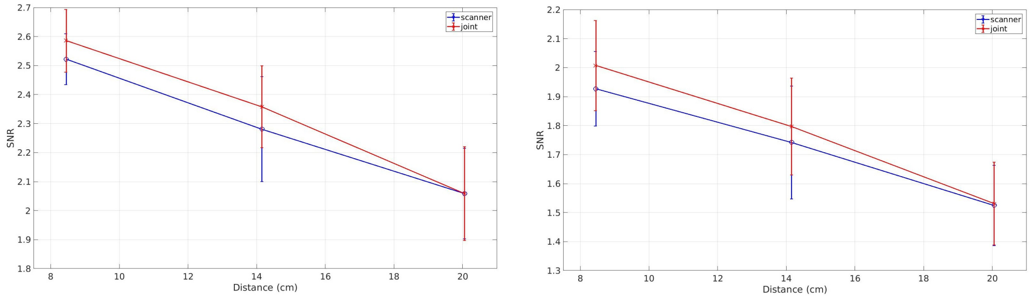

(e) Diameter = 0.6 cm , 12:1 contrast. **(f)** Diameter = 0.6 cm , 6:1 contrast.

Figure 3.25. SNR of the reconstructions shown in Figures 3.20 and 3.21 as a function of the distance between the centers of the spheres and the surface of the flat-panel insert. The error bars are derived by averaging over the five spheres in the row.

All the phantoms designed and tested in Chapter 3, seem to be horizontally aligned. This is because the focus and main purpose were to implement and test the surveillance mode imaging regime and reconstruction framework. More realistic phantom designs should have the tumors more variably distributed in the body phantom. This makes more sense when the insert effectively acquires data from more than one azimuthal angle[18] (in-plane angles), so the the IS (or vIS) counts become more tomographic.

---

[18] Either from multiple panel inserts forming an arc or forming a semicircle, or from one single panel insert that moves in semicircular steps.

References

[1] S. Agostinelli, J. Allison, K. Amako, J. Apostolakis, H. Araujo, P. Arce, M. Asai, D. Axen, S. Banerjee, G. Barrand, F. Behner, L. Bellagamba, J. Boudreau, L. Broglia, A. Brunengo, H. Burkhardt, S. Chauvie, J. Chuma, R. Chytracek, G. Cooperman, G. Cosmo, P. Degtyarenko, A. Dell'Acqua, G. Depaola, D. Dietrich, R. Enami, A. Feliciello, C. Ferguson, H. Fesefeldt, G. Folger, F. Foppiano, A. Forti, S. Garelli, S. Giani, R. Giannitrapani, D. Gibin, J.J. Gómez Cadenas, I. González, G. Gracia Abril, G. Greeniaus, W. Greiner, V. Grichine, A. Grossheim, S. Guatelli, P. Gumplinger, R. Hamatsu, K. Hashimoto, H. Hasui, A. Heikkinen, A. Howard, V. Ivanchenko, A. Johnson, F.W. Jones, J. Kallenbach, N. Kanaya, M. Kawabata, Y. Kawabata, M. Kawaguti, S. Kelner, P. Kent, A. Kimura, T. Kodama, R. Kokoulin, M. Kossov, H. Kurashige, E. Lamanna, T. Lampén, V. Lara, V. Lefebure, F. Lei, M. Liendl, W. Lockman, F. Longo, S. Magni, M. Maire, E. Medernach, K. Minamimoto, P. Mora de Freitas, Y. Morita, K. Murakami, M. Nagamatu, R. Nartallo, P. Nieminen, T. Nishimura, K. Ohtsubo, M. Okamura, S. O'Neale, Y. Oohata, K. Paech, J. Perl, A. Pfeiffer, M.G. Pia, F. Ranjard, A. Rybin, S. Sadilov, E. Di Salvo, G. Santin, T. Sasaki, N. Savvas, Y. Sawada, S. Scherer, S. Sei, V. Sirotenko, D. Smith, N. Starkov, H. Stoecker, J. Sulkimo, M. Takahata, S. Tanaka, E. Tcherniaev, E. Safai Tehrani, M. Tropeano, P. Truscott, H. Uno, L. Urban, P. Urban, M. Verderi, A. Walkden, W. Wander, H. Weber, J.P. Wellisch, T. Wenaus, D.C. Williams, D. Wright, T. Yamada, H. Yoshida, and D. Zschiesche. Geant4a simulation toolkit. *Nuclear Instruments and Methods in Physics Research Section A: Accelerators, Spectrometers, Detectors and Associated Equipment*, 506(3):250–303, 2003.

[2] Beverly Agtuca, Elisabeth Rieger, Katharina Hilger, Lihui Song, Christelle AM Robert, Matthias Erb, Abhijit Karve, and Richard A Ferrieri. Carbon-11 reveals opposing roles of auxin and salicylic acid in regulating leaf physiology, leaf metabolism, and resource allocation patterns that impact root growth in Zea mays. *Journal of Plant Growth Regulation*, 33(2):328–339, 2014.

[3] S. Akazawa. The scope of the Japanese information industry in the 1980s. In K. R. Brown, editor, *The challenge of information technology: Proceedings of the forty-first FID (Federation Internationale de Documentation) congress held in Hong Kong 13-16 September 1982*, pages 19–22, Amsterdam, New York, and Oxford, 1983. North Holland.

[4] David L Alexoff, Stephen L Dewey, Paul Vaska, Srilalan Krishnamoorthy, Richard Ferrieri, Michael Schueller, David J Schlyer, and Joanna S Fowler. PET imaging of thin objects: measuring the effects of positron range and partial-volume averaging in the leaf of Nicotiana tabacum. *Nuclear Medicine and Biology*, 38(2):191–200, 2011.

[5] J. Allison, K. Amako, J. Apostolakis, H. Araujo, P. Arce Dubois, M. Asai, G. Barrand, R. Capra, S. Chauvie, R. Chytracek, G.A.P. Cirrone, G. Cooperman, G. Cosmo, G. Cuttone, G.G. Daquino, M. Donszelmann, M. Dressel, G. Folger, F. Foppiano, J. Generowicz, V. Grichine, S. Guatelli, P. Gumplinger, A. Heikkinen, I. Hrivnacova, A. Howard, S. Incerti, V. Ivanchenko, T. Johnson, F. Jones, T. Koi, R. Kokoulin, M. Kossov, H. Kurashige, V. Lara, S. Larsson, F. Lei, O. Link, F. Longo, M. Maire, A. Mantero, B. Mascialino, I. McLaren, P. Mendez Lorenzo, K. Minamimoto, K. Murakami, P. Nieminen, L. Pandola, S. Parlati, L. Peralta, J. Perl, A. Pfeiffer, M.G. Pia, A. Ribon, P. Rodrigues, G. Russo, S. Sadilov, G. Santin, T. Sasaki, D. Smith, N. Starkov, S. Tanaka, E. Tcherniaev, B. Tome, A. Trindade, P. Truscott, L. Urban, M. Verderi, A. Walkden, J.P. Wellisch, D.C. Williams, D. Wright, and H. Yoshida. Geant4 developments and applications. *IEEE Transactions on Nuclear Science*, 53(1):270–278, feb 2006.

[6] J. Allison, K. Amako, J. Apostolakis, P. Arce, M. Asai, T. Aso, E. Bagli, A. Bagulya, S. Banerjee, G. Barrand, B.R. Beck, A.G. Bogdanov, D. Brandt, J.M.C. Brown, H. Burkhardt, Ph. Canal, D. Cano-Ott, S. Chauvie, K. Cho, G.A.P. Cirrone, G. Cooperman, M.A. Cortés-Giraldo, G. Cosmo, G. Cuttone, G. Depaola, L. Desorgher, X. Dong, A. Dotti, V.D. Elvira, G. Folger, Z. Francis, A. Galoyan, L. Garnier, M. Gayer, K.L. Genser, V.M. Grichine, S. Guatelli, P. Guèye, P. Gumplinger, A.S. Howard, I. Hivnáčová, S. Hwang, S. Incerti, A. Ivanchenko, V.N. Ivanchenko, F.W. Jones, S.Y. Jun, P. Kaitaniemi, N. Karakatsanis, M. Karamitros, M. Kelsey, A. Kimura, T. Koi, H. Kurashige, A. Lechner, S.B. Lee, F. Longo, M. Maire, D. Mancusi, A. Mantero, E. Mendoza, B. Morgan, K. Murakami, T. Nikitina, L. Pandola, P. Paprocki, J. Perl, I. Petrović, M.G. Pia, W. Pokorski, J.M. Quesada, M. Raine, M.A. Reis, A. Ribon, A. Ristić Fira, F. Romano, G. Russo, G. Santin, T. Sasaki, D. Sawkey, J.I. Shin, I.I. Strakovsky, A. Taborda, S. Tanaka, B. Tomé, T. Toshito, H.N. Tran, P.R. Truscott, L. Urban, V. Uzhinsky, J.M. Verbeke, M. Verderi, B.L. Wendt, H. Wenzel, D.H. Wright, D.M. Wright, T. Yamashita, J. Yarba, and H. Yoshida. Recent developments in Geant4. *Nuclear Instruments and Methods in Physics Research Section A: Accelerators, Spectrometers, Detectors and Associated Equipment*, 835:186–225, 2016.

[7] American Library Association, Young Adult Services Division, Services Statement Development Committee. Directions for library service to young adults. Chicago, 1978.

[8] Hal O Anger. Sensitivity, resolution, and linearity of the scintillation camera. *IEEE Transactions on Nuclear Science*, 13(3):380–392, 1966.

[9] Gilberto Artioli. *Structural studies of the water molecules and hydrogen bonding in zeolites.* PhD thesis, University of Chicago, 1985.

[10] Bertil Axelsson, Peter Msaki, and Anders Israelsson. Subtraction of compton-scattered photons in single-photon emission computerized tomography. *Journal of nuclear medicine: official publication, Society of Nuclear Medicine*, 25(4):490–494, 1984.

[11] RD Badawi, MP Miller, DL Bailey, and PK Marsden. Randoms variance reduction in 3d pet. *Physics in medicine and biology*, 44(4):941, 1999.

[12] Bing Bai, Q Li, CH Holdsworth, E Asma, Yuan-Chuan Tai, A Chatziioannou, and Richard M Leahy. Model-based normalization for iterative 3d pet image reconstruction. *Physics in medicine and biology*, 47(15):2773, 2002.

[13] Dale L Bailey and Steven R Meikle. A convolution-subtraction scatter correction method for 3D PET. *Physics in medicine and biology*, 39(3):411, 1994.

[14] Harrison H Barrett and Kyle J Myers. *Foundations of image science.* John Wiley & Sons, 2013.

[15] Harrison H Barrett, Timothy White, and Lucas C Parra. List-mode likelihood. *JOSA A*, 14(11):2914–2923, 1997.

[16] Harrison H Barrett, Donald W Wilson, and Benjamin MW Tsui. Noise properties of the em algorithm. i. theory. *Physics in medicine and biology*, 39(5):833, 1994.

[17] HH Barrett, KJ Myers, and RF Wagner. Beyond signal-detection theory. In *Proc. SPIE*, volume 626, pages 1–239, 1986.

[18] S Beer, M Streun, T Hombach, J Buehler, S Jahnke, M Khodaverdi, H Larue, S Minwuyelet, C Parl, G Roeb, et al. Design and initial performance of PlanTIS: a high-resolution positron emission tomograph for plants. *Phys. Med. Biol.*, 55(3):635, 2010.

[19] M Bentourkia, P Msaki, J Cadorette, and R Lecomte. Assessment of scatter components in high-resolution pet: correction by nonstationary convolution subtraction. *Journal of Nuclear Medicine*, 36(1):121–130, 1995.

[20] Ljudmilla Borisjuk, Hardy Rolletschek, and Thomas Neuberger. Surveying the plants world by magnetic resonance imaging. *The Plant Journal*, 70(1):129–146, 2012.

[21] E Boroński and RM Nieminen. Electron-positron density-functional theory. *Physical Review B*, 34(6):3820, 1986.

[22] Christopher S Butler and Michael I Miller. Maximum a posteriori estimation for SPECT using regularization techniques on massively parallel computers. *IEEE transactions on medical imaging*, 12(1):84–89, 1993.

[23] Charles Byrne. Likelihood maximization for list-mode emission tomographic image reconstruction. *IEEE Transactions on Medical Imaging*, 20(10):1084–1092, 2001.

[24] C Carrier, C Martel, D Schmitt, and R Lecomte. Design of a high resolution positron emission tomograph using solid state scintillation detectors. *IEEE Transactions on Nuclear Science*, 35(1):685–690, 1988.

[25] ME Casey and EJ Hoffman. A technique to reduce noise in accidental coincidence measurements and coincidence efficiency calibration. *J. Comput. Assist. Tomogr*, 10(6):845–850, 1986.

[26] Lynette Cegelski and Jacob Schaefer. NMR determination of photorespiration in intact leaves using in vivo 13 CO 2 labeling. *Journal of Magnetic Resonance*, 178(1):1–10, 2006.

[27] Simon R Cherry and Sung-Cheng Huang. Effects of scatter on model parameter estimates in 3d pet studies of the human brain. *IEEE transactions on nuclear science*, 42(4):1174–1179, 1995.

[28] Simon R Cherry, Steven R Meikle, and E Jcorrection Hoffman. Correction and characterization of scattered events in three-dimensional pet using scanners with retractable septa. *Journal of nuclear medicine: official publication, Society of Nuclear Medicine*, 34(4):671–678, 1993.

[29] Simon R Cherry, James A Sorenson, and Michael E Phelps. *Physics in Nuclear Medicine*. Elsevier Health Sciences, 2012.

[30] B. G. F. Cohen. Human aspects in office automation. Technical Report NTIS, PB84-240738, National Institute for Occupational Safety and Health, Division of Biomedical and Behavioral Science, Cincinnati, 1984.

[31] BE Cooke, AC Evans, EO Fanthome, R Alarie, and AM Sendyk. Performance figures and images from the therascan 3128 positron emission tomograph. *IEEE Transactions on Nuclear Science*, 31(1):640–644, 1984.

[32] DW Cooke, KJ McClellan, BL Bennett, JM Roper, MT Whittaker, RE Muenchausen, and RC Sze. Crystal growth and optical characterization of cerium-doped Lu1. 8Y0. 2SiO5. *Journal of Applied Physics*, 88(12):7360–7362, 2000.

[33] Margaret E Daube-Witherspoon and Richard E Carson. Unified deadtime correction model for pet. *IEEE transactions on medical imaging*, 10(3):267–275, 1991.

[34] Alvaro R De Pierro. On the relation between the ISRA and the EM algorithm for positron emission tomography. *IEEE Transactions on Medical Imaging*, 12(2):328–333, 1993.

[35] Alvaro R De Pierro. A modified expectation maximization algorithm for penalized likelihood estimation in emission tomography. *IEEE Transactions on Medical Imaging*, 14(1):132–137, 1994.

[36] Veerle De Schepper, Jonas Bühler, Michael Thorpe, Gerhard Roeb, Gregor Huber, Dagmar van Dusschoten, Siegfried Jahnke, and Kathy Steppe. 11C-PET imaging reveals transport dynamics and sectorial plasticity of oak phloem after girdling. *Frontiers in Plant Science*, 4, 2013.

[37] Michel Defrise, Paul E Kinahan, David W Townsend, Christian Michel, Merence Sibomana, and Danny F Newport. Exact and approximate rebinning algorithms for 3-d pet data. *IEEE transactions on medical imaging*, 16(2):145–158, 1997.

[38] Timothy R DeGrado, Timothy G Turkington, J Jay Williams, Charles W Stearns, John M Hoffman, and R Edward Coleman. Performance characteristics of a whole-body pet scanner. *Journal of Nuclear Medicine*, 35(8):1398–1406, 1994.

[39] Arthur P Dempster, Nan M Laird, and Donald B Rubin. Maximum likelihood from incomplete data via the em algorithm. *Journal of the royal statistical society. Series B (methodological)*, pages 1–38, 1977.

[40] Stephen E Derenzo. Precision measurement of annihilation point spread distributions for medically important positron emitters. pages 819–823. Sendai, Japan: The Japan Institute of Metals, 1979.

[41] Richard E Dickson and Philip R Larson. Incorporation of 14C-photosynthate into major chemical fractions of source and sink leaves of cottonwood. *Plant Physiology*, 56(2):185–193, 1975.

[42] Rebecca C Dirks, Manmilan Singh, Gregory S Potter, Lee G Sobotka, and Jacob Schaefer. Carbon partitioning in soybean (Glycine max) leaves by combined 11C and 13C labeling. *New Phytologist*, 196(4):1109–1121, 2012.

[43] Niraj K Doshi, Yiping Shao, Robert W Silverman, and Simon R Cherry. Design and evaluation of an lso pet detector for breast cancer imaging. *Medical physics*, 27(7):1535–1543, 2000.

[44] Niraj K Doshi, Robert W Silverman, Yiping Shao, and Simon R Cherry. maxpet, a dedicated mammary and axillary region pet imaging system for breast cancer. *IEEE Transactions on Nuclear Science*, 48(3):811–815, 2001.

[45] Bert G Drake, Miquel A Gonzàlez-Meler, and Steve P Long. More efficient plants: a consequence of rising atmospheric CO2? *Annual Review of Plant Biology*, 48(1):609–639, 1997.

[46] Peter K Farage, Ian F McKee, and Steve P Long. Does a low nitrogen supply necessarily lead to acclimation of photosynthesis to elevated CO2? *Plant Physiology*, 118(2):573–580, 1998.

[47] Jeffrey A Fessler. Penalized weighted least-squares image reconstruction for positron emission tomography. *IEEE transactions on medical imaging*, 13(2):290–300, 1994.

[48] RD Fiete, Harrison H Barrett, White E Smith, and Kyle J Myers. Hotelling trace criterion and its correlation with human-observer performance. *JOSA A*, 4(5):945–953, 1987.

[49] Carey E Floyd Jr, Ronald J Jaszczak, Kim L Greer, and R Edward Coleman. Deconvolution of compton scatter in spect. *Journal of nuclear medicine: official publication, Society of Nuclear Medicine*, 26(4):403–408, 1985.

[50] G Germano and EJ Hoffman. A study of data loss and mispositioning due to pileup in 2-d detectors in pet. *IEEE Transactions on Nuclear Science*, 37(2):671–675, 1990.

[51] Peter J Green. Bayesian reconstructions from emission tomography data using a modified em algorithm. *IEEE transactions on medical imaging*, 9(1):84–93, 1990.

[52] Martin Greenberger, Julius Aronofsky, James L. McKenney, and William F. Massy, editors. *Networks for research and education: Sharing of computer and information resources nationwide.* MIT Press, Cambridge, 1974.

[53] S Grootoonk, TJ Spinks, D Sashin, NM Spyrou, and T Jones. Correction for scatter in 3d brain pet using a dual energy window method. *Physics in medicine and biology*, 41(12):2757, 1996.

[54] RL Harrison, SD Vannoy, DR Haynor, SB Gillispie, MS Kaplan, and TK Lewellen. Preliminary experience with the photon history generator module of a public-domain simulation system for emission tomography. In *Conf. Rec. IEEE Nucl. Sci. Symp*, pages 1154–1158, 1993.

[55] Harold Hotelling. The generalization of student's ratio. *The Annals of Mathematical Statistics*, 2(3):360–378, 1931.

[56] John Theodore Houghton, YDJG Ding, David J Griggs, Maria Noguer, Paul J van der Linden, Xiaosu Dai, Kathy Maskell, and CA Johnson. *The scientific basis, intergovernmental panel on climate change.* Cambridge University Press, Cambridge, UK, 2001.

[57] Richard Jackson. Running down the up-escalator: Regional inequality in papua new guinea. *Australian Geographer*, 14:175–84, May 1979.

[58] Siegfried Jahnke, Marion I Menzel, Dagmar Van Dusschoten, Gerhard W Roeb, Jonas Bühler, Senay Minwuyelet, Peter Blümler, Vicky M Temperton, Thomas Hombach, Matthias Streun, et al. Combined MRI–PET dissects dynamic changes in plant structures and functions. *The Plant Journal*, 59(4):634–644, 2009.

[59] S Jan, D Benoit, E Becheva, T Carlier, F Cassol, P Descourt, T Frisson, L Grevillot, L Guigues, L Maigne, C Morel, Y Perrot, N Rehfeld, D Sarrut, D R Schaart, S Stute, U Pietrzyk, D Visvikis, N Zahra, and I Buvat. GATE V6: a major enhancement of the GATE simulation platform enabling modelling of CT and radiotherapy. *Physics in Medicine and Biology*, 56(4):881–901, feb 2011.

[60] S Jan, G Santin, D Strul, S Staelens, K Assié, D Autret, S Avner, R Barbier, M Bardiès, P M Bloomfield, D Brasse, V Breton, P Bruyndonckx, I Buvat, A F Chatziioannou, Y Choi, Y H Chung, C Comtat, D Donnarieix, L Ferrer, S J Glick, C J Groiselle, D Guez, P-F Honore, S Kerhoas-Cavata, A S Kirov, V Kohli, M Koole, M Krieguer, D J van der Laan, F Lamare, G Largeron, C Lartizien, D Lazaro, M C Maas, L Maigne, F Mayet, F Melot, C Merheb, E Pennacchio, J Perez, U Pietrzyk, F R Rannou, M Rey, D R Schaart, C R Schmidtlein, L Simon, T Y Song, J-M Vieira, D Visvikis, R Van de Walle, E Wieërs, and C Morel. GATE: a simulation toolkit for PET and SPECT. *Physics in Medicine and Biology*, 49(19):4543–4561, oct 2004.

[61] Vincent Keereman, Yves Fierens, Tom Broux, Yves De Deene, Max Lonneux, and Stefaan Vandenberghe. MRI-based attenuation correction for PET/MRI using ultrashort echo time sequences. *J. Nucl. Med.*, 51(5):812–818, 2010.

[62] Daniel B Keesing, Aswin Mathews, Sergey Komarov, Heyu Wu, Tae Yong Song, Joseph A OSullivan, and Yuan-Chuan Tai. Image reconstruction and system modeling techniques for virtual-pinhole pet insert systems. *Physics in medicine and biology*, 57(9):2517, 2012.

[63] Paul E Kinahan and JG Rogers. Analytic 3d image reconstruction using all detected events. *IEEE Transactions on Nuclear Science*, 36(1):964–968, 1989.

[64] PE Kinahan, DW Townsend, T Beyer, and D Sashin. Attenuation correction for a combined 3D PET/CT scanner. *Medical Physics*, 25(10):2046–2053, 1998.

[65] S Kiyomiya, H Nakanishi, H Uchida, S Nishiyama, H Tsukada, NS Ishioka, S Watanabe, A Osa, C Mizuniwa, T Ito, et al. Light activates H2 15O flow in rice: Detailed monitoring using a positron-emitting tracer imaging system (PETIS). *Physiologia Plantarum*, 113(3):359–367, 2001.

[66] Kenneth Lange, Mark Bahn, and Roderick Little. A theoretical study of some maximum likelihood algorithms for emission and transmission tomography. *IEEE Transactions on Medical Imaging*, 6(2):106–114, 1987.

[67] Kenneth Lange and Richard Carson. EM reconstruction algorithms for emission and transmission tomography. *Journal of computer assisted tomography*, 8(2):306–316, 1984.

[68] Craig S Levin, M Dahlbom, and Edward J Hoffman. A Monte Carlo correction for the effect of compton scattering in 3-d pet brain imaging. *IEEE Transactions on Nuclear Science*, 42(4):1181–1185, 1995.

[69] Craig S Levin and Edward J Hoffman. Calculation of positron range and its effect on the fundamental limit of positron emission tomography system spatial resolution. *Phys. Med. Biol.*, 44(3):781–799, 1999.

[70] Emanuel Levitan and Gabor T Herman. A maximum a posteriori probability expectation maximization algorithm for image reconstruction in emission tomography. *IEEE Transactions on Medical Imaging*, 6(3):185–192, 1987.

[71] J-S Liow and SC Strother. Practical tradeoffs between noise, quantitation, and number of iterations for maximum likelihood-based reconstructions. *IEEE transactions on medical imaging*, 10(4):563–571, 1991.

[72] Dong C Liu and Jorge Nocedal. On the limited memory bfgs method for large scale optimization. *Mathematical programming*, 45(1):503–528, 1989.

[73] Aswin John Mathews, Sergey Komarov, Heyu Wu, Joseph A O'Sullivan, and Yuan-Chuan Tai. Improving pet imaging for breast cancer using virtual pinhole pet half-ring insert. *Physics in medicine and biology*, 58(18):6407, 2013.

[74] Aswin John Mathews, Ke Li, Sergey Komarov, Qiang Wang, Bosky Ravindranath, Joseph A OSullivan, and Yuan-Chuan Tai. A generalized reconstruction framework for unconventional PET systems. *Medical Physics*, 42(8):4591–4609, 2015.

[75] Charles E Metz. Basic principles of roc analysis. In *Seminars in nuclear medicine*, volume 8, pages 283–298. Elsevier, 1978.

[76] Peter EH Minchin and Michael R Thorpe. Using the short-lived isotope 11C in mechanistic studies of photosynthate transport. *Funct. Plant Biol*, 30(8):831–841, 2003.

[77] Sacha J Mooney, Tony P Pridmore, Jonathan Helliwell, and Malcolm J Bennett. Developing x-ray computed tomography to non-invasively image 3-d root systems architecture in soil. *Plant and soil*, 352(1-2):1–22, 2012.

[78] J Moorby, M Ebert, and NTS Evans. The translocation of 11C-labelled photosynthate in the soybean. *J. Exp. Botany*, 14(2):210–220, 1963.

[79] Erkan U Mumcuoglu, Richard Leahy, Simon R Cherry, and Zhenyu Zhou. Fast gradient-based methods for bayesian reconstruction of transmission and emission pet images. *IEEE transactions on Medical Imaging*, 13(4):687–701, 1994.

[80] Hiromi Nakanishi, Naimatullah Bughio, Shinpei Matsuhashi, Noriko-Shigeta Ishioka, Hiroshi Uchida, Atsunori Tsuji, Akihiko Osa, Toshiaki Sekine, Tamikazu Kume, and Satoshi Mori. Visualizing real time [11C] methionine translocation in Fe-sufficient and Fe-deficient barley using a positron emitting tracer imaging system (PETIS). *J. Exp. Botany*, 50(334):637–643, 1999.

[81] John M Ollinger. Model-based scatter correction for fully 3D PET. *Physics in medicine and biology*, 41(1):153, 1996.

[82] Alpaslan Ongun and CR Stocking. Effect of light on the incorporation of serine into the carbohydrates of chloroplasts and nonchloroplast fractions of tobacco leaves. *Plant Physiol*, 40(5):819–824, 1965.

[83] Joseph A O'Sullivan and Jasenka Benac. Alternating minimization algorithms for transmission tomography. *IEEE Transactions on Medical Imaging*, 26(3):283–297, 2007.

[84] Sang-June Park, W Leslie Rogers, and Neal H Clinthorne. Design of a very high-resolution small animal pet scanner using a silicon scatter detector insert. *Physics in medicine and biology*, 52(15):4653, 2007.

[85] Hao Peng and Craig S Levin. Study of pet intrinsic spatial resolution and contrast recovery improvement for pet/mri systems. *Physics in medicine and biology*, 57(9):N101, 2012.

[86] Michael E Phelps, Edward J Hoffman, Nizar A Mullani, and Michel M Ter-Pogossian. Application of annihilation coincidence detection to transaxial reconstruction tomography. *Journal of Nuclear Medicine*, 16(3):210–224, 1975.

[87] David G Politte and Donald L Snyder. Corrections for accidental coincidences and attenuation in maximum-likelihood image reconstruction for positron-emission tomography. *IEEE Transactions on Medical Imaging*, 10(1):82–89, 1991.

[88] JG Rogers, R Harrop, and PE Kinahan. The theory of three-dimensional image reconstruction for pet. *IEEE transactions on medical imaging*, 6(3):239–243, 1987.

[89] Roy Pines Sallen and Edwin L Key. A practical method of designing RC active filters. *IRE Transactions on Circuit Theory*, 2(1):74–85, 1955.

[90] Lingxiong Shao, Richard Freifelder, and Joel S Karp. Triple energy window scatter correction technique in pet. *IEEE transactions on medical imaging*, 13(4):641–648, 1994.

[91] Lawrence A Shepp and Yehuda Vardi. Maximum likelihood reconstruction for emission tomography. *IEEE Transactions on Medical Imaging*, 1(2):113–122, 1982.

[92] Robert L Siddon. Fast calculation of the exact radiological path for a three-dimensional CT array. *Medical Physics*, 12(2):252–255, 1985.

[93] Stefan Siegel, Robert W Silverman, Yiping Shao, and Simon R Cherry. Simple charge division readouts for imaging scintillator arrays using a multi-channel PMT. *IEEE Transactions on Nuclear Science*, 43(3):1634–1641, 1996.

[94] BW Silverman, MC Jones, JD Wilson, and DW Nychka. A smoothed em approach to indirect estimation problems, with particular, reference to stereology and emission tomography. *Journal of the Royal Statistical Society. Series B (Methodological)*, pages 271–324, 1990.

[95] Warren E Smith and Harrison H Barrett. Hotelling trace criterion as a figure of merit for the optimization of imaging systems. *JOSA A*, 3(5):717–725, 1986.

[96] Donald L Snyder, Michael I Miller, Lewis J Thomas, and David G Politte. Noise and edge artifacts in maximum-likelihood reconstructions for emission tomography. *IEEE transactions on medical imaging*, 6(3):228–238, 1987.

[97] Donald L Snyder, Joseph A O'Sullivan, Ryan J Murphy, David G Politte, Bruce R Whiting, and Jeffrey F Williamson. Image reconstruction for transmission tomography when projection data are incomplete. *Phys. Med. Biol.*, 51(21):5603, 2006.

[98] Donald L Snyder and David G Politte. Image reconstruction from list-mode data in an emission tomography system having time-of-flight measurements. *IEEE Transactions on Nuclear Science*, 30(3):1843–1849, 1983.

[99] CW Stearns. Scatter correction method for 3D PET using 2D fitted Gaussian functions. *J Nucl Med*, 36(5):105P, 1995.

[100] Alexander V Stolin, Andrew G Weisenberger, John E McKisson, and Stan Majewski. Feasibility study of using detection of direct positrons in plant imaging research. In *Nuclear Science Symposium Conference Record (NSS/MIC)*, pages 2338–2341. IEEE, 2009.

[101] William Jr. Strunk and E. B. White. *The Elements of Style*. MacMillan Publishing Co., New York, 3rd edition, 1979.

[102] Yuan-Chuan Tai, Heyu Wu, Debashish Pal, and Joseph A O'Sullivan. Virtual-pinhole pet. *Journal of Nuclear Medicine*, 49(3):471–479, 2008.

[103] Michel M Ter-Pogossian, Michael E Phelps, Edward J Hoffman, and Nizar A Mullani. A positron-emission transaxial tomograph for nuclear imaging (PETT). *Radiology*, 114(1):89–98, 1975.

[104] CJ Thompson. The effect of collimation on scatter fraction in multi-slice pet. *IEEE Transactions on Nuclear Science*, 35(1):598–602, 1988.

[105] CJ Thompson, K Murthy, Y Picard, IN Weinberg, and R Mako. Positron emission mammography (PEM): a promising technique for detecting breast cancer. *IEEE Transactions on Nuclear Science*, 42(4):1012–1017, 1995.

[106] CJ Thompson, K Murthy, IN Weinberg, and F Mako. Feasibility study for positron emission mammography. *Medical physics*, 21(4):529–538, 1994.

[107] MP Tornai, CS Levin, LR MacDonald, CH Holdsworth, and EJ Hoffman. A miniature phoswich detector for gamma-ray localization and beta imaging. *IEEE Transactions on Nuclear Science*, 45(3):1166–1173, 1998.

[108] MP Tornai, LR MacDonald, CS Levin, S Siegel, and EJ Hoffman. Design considerations and initial performance of a 1.2 cm 2 beta imaging intra-operative probe. *IEEE Transactions on Nuclear Science*, 43(4):2326–2335, 1996.

[109] Kate L. Turabian. *A Manual for Writers of Term Papers, Theses, and Dissertations.* University of Chicago Press, Chicago, 5th edition, 1987.

[110] U.S. Department of Agriculture. *Will there be enough food? The 1981 yearbook of agriculture.* Government Printing Office, Washington, D.C., 1981.

[111] Eugene Veklerov and Jorge Llacer. Stopping rule for the mle algorithm based on statistical hypothesis testing. *IEEE Transactions on Medical Imaging*, 6(4):313–319, 1987.

[112] John R Votaw and Jonathan A Nye. *Physics and Instrumentation of Cardiac Positron Emission Tomography/Computed Tomography.* 2015.

[113] Qiang Wang, Aswin J Mathews, Ke Li, Jie Wen, Sergey Komarov, Joseph A OSullivan, and Yuan-Chuan Tai. A dedicated high-resolution PET imager for plant sciences. *Phys. Med. Biol.*, 59(19):5613–5629, 2014.

[114] Zhou Wang, Alan C Bovik, Hamid R Sheikh, and Eero P Simoncelli. Image quality assessment: from error visibility to structural similarity. *IEEE Transactions on Image Processing*, 13(4):600–612, 2004.

[115] Charles C Watson, DMEC Newport, and Mike E Casey. A single-scatter simulation technique for scatter correction in 3D PET. In *Three-dimensional image reconstruction in radiology and nuclear medicine*, pages 255–268. Springer, 1996.

[116] AG Weisenberger, A Stolin, B Kross, SJ Lee, S Majewski, J McKisson, JE McKisson, W Xi, C Zorn, CR Howell, et al. Compact beta particle/positron imager for plant biology. In *Nuclear Science Symposium Conference Record (NSS/MIC), 2010 IEEE*, pages 1752–1754. IEEE, 2010.

[117] Andrew G Weisenberger, Brian Kross, Seungjoon Lee, John McKisson, JE McKisson, Wenze Xi, Carl Zorn, Chantal D Reid, Calvin R Howell, Alexander S Crowell, et al. PhytoBeta imager: a positron imager for plant biology. *Phys. Med. Biol.*, 57(13):4195–4210, 2012.

[118] Chien-shiung Wu. Beta-decay. In *Weak Interactions and High-Energy Neutino Physics*, page 52, 1966.

[119] Heyu Wu and Yuan-Chuan Tai. A novel phoswich imaging detector for simultaneous beta and coincidence-gamma imaging of plant leaves. *Phys. Med. Biol.*, 56(17):5583–5598, 2011.

Vita

Homayoon Ranjbar

Degrees	B.S. Electrical Engineering, Amirkabir University of Technology (Tehran Polytechnic), May 2011 M.S. Electrical and Systems Engineering, Washington University in St. Louis, December 2014 Ph.D. Electrical and Systems Engineering, Washington University in St. Louis, December 2017
Professional Societies	Institute of Electrical and Electronics Engineers (IEEE) Association of Graduate Engineering Students (AGES) at Washington University in St. Louis
Courses	Optimization, Detection and Estimation Theory, Probability and Stochastic Processes, Special Topics: Alternating Minimization Algorithms in Information Theory and Inference, Biomedical Optics I: Principles, Principles in Applications of Biological Imaging, Biological Imaging Technology, Biological Neural Computation, Information Theory, Machine Learning, and Coding Theory.
Employment	Graduate Student Research Assistant, 2012-2017, *Washington University, St. Louis, MO.* PET scientist intern, Summer 2017, *RefleXion Medical, Hayward, CA.* Senior SPECT Software Engineer, starting in January 2018, *Siemens Healthineers, Hoffman Estates, IL.*
Publications	**Ranjbar, H.**, Wen, J., Mathews, A. J., Komarov, S., Wang, Q., Li, K., O'Sullivan, J. A., Tai, Y. C. (2016). A simultaneous beta and coincidence-gamma imaging system for plant leaves. *Physics in medicine and biology, 61*(9), 3572.

Ranjbar, H., Wen, J., Mathews, A. J., O'Sullivan, J. A., Tai, Y. C. (2014). A joint beta and coincidence-gamma data modeling and image reconstruction framework for plant leaf imaging. *Nuclear Science Symposium and Medical Imaging Conference (NSS/MIC)*, 2014 IEEE (pp. 1-5). IEEE.

December 2017

Joint Reconstruction in PET, Ranjbar, Ph.D. 2017